

Development of a Three-dimensional Multi-scale Model to Study the Formation of Solidification Defects in Fusion Welding

by

Hamid Reza Zareie Rajani

B.Sc., Isfahan University of Technology, 2008

M.Sc., University of Tehran, 2011

A THESIS SUBMITTED IN PARTIAL FULFILLMENT OF
THE REQUIREMENTS FOR THE DEGREE OF

Doctor of Philosophy

in

THE COLLEGE OF GRADUATE STUDIES

(Applied Science)

THE UNIVERSITY OF BRITISH COLUMBIA

(Okanagan)

February 2016

© Hamid Reza Zareie Rajani, 2016

The undersigned certify that they have read, and recommend to the College of Graduate Studies for acceptance, a thesis entitled:

Development of a three-dimensional multi-scale model to study the formation of solidification defects in fusion welding.

submitted by Hamid Reza Zareie Rajani in partial fulfilment of the requirements of
the degree of Doctor of Philosophy.

Andre Phillion, School of Engineering

Supervisor, Professor (please print name and faculty/school above the line)

Joshua Brinkerhoff, School of Engineering

Supervisory Committee Member, Professor (please print name and faculty/school in the line above)

Lukas Bichler, School of Engineering

Supervisory Committee Member, Professor (please print name and faculty/school in the line above)

Yves Lucet, School of Art and Sciences

University Examiner, Professor (please print name and faculty/school in the line above)

Mathieu Brochu, McGill University

External Examiner, Professor (please print name and university in the line above)

March 18, 2016

(Date Submitted to Grad Studies)

Abstract

One of the long-standing challenges in joining of aluminum alloys is the occurrence of solidification defects, i.e. hot cracking and porosity, since these defects significantly increase manufacturing costs. This research project investigates the formation of solidification defects through development of a novel and comprehensive 3-D multi-scale and multi-physics numerical study and then application to the GTA welding of the aluminum alloy AA6061. The developed multi-scale model is composed of four different modules: 1) Solidification, 2) Deformation, 3) Fluid flow, and 4) Defect formation. The solidification module numerically reconstructs the 3-D microstructure of semisolid welds using a granular model of solidification. Specifically, a modified Voronoi tessellation algorithm is used to generate an unstructured grid representing the weld microstructure. The reconstructed microstructure contains both columnar and equiaxed grains and varies as a function of welding process parameters. Then, the Scheil equation is used in combination with the temperature field obtained through the Rosenthal equation and the reconstructed 3D microstructure to simulate solidification. This module outputs the evolving 3D structure of the semisolid weld composed of solid grains and a network of micro liquid channels for use by the deformation and fluid flow modules as the simulation geometry. The deformation module analyzes via finite elements the deformation of the semisolid weld due to externally applied strains and self-induced strains such as thermo-mechanical strains and solidification shrinkage in order to obtain local strain rates within the micro liquid channels. The local strain rates outputted by the deformation module feed a fluid flow analysis module in which the pressure field within the semisolid weld is calculated. Finally, the defect formation module uses various defect formation models to link the pressure field and the local strain rates to the formation of solidification defects including micro cracks and hydrogen porosity.

Preface

The developed multi-scale multi-physics model is inspired by recent work on granular modeling of solidification defects in casting at École polytechnique fédérale de Lausanne (EPFL) and the University of British Columbia (UBC) by professors M. Rappaz, A.B. Phillion, and Dr. M. Sistaninia. My key contribution was to extend the application of the granular modeling technique to the field of welding for the first time. In this research, I managed to address several challenges in the exploitation of granular modeling in welding caused by the complex microstructure of the weld and also the non-uniform nature of the thermal field in welding. I was responsible for developing all the modules of the model as well as analyzing the results. I used several programming languages such as C++, Fortran, Python, and Matlab to create various parts of each module. In addition, I designed an automatic welding table and a series of welding experiments to assess the accuracy of the model. Two students helped me in conducting the welding experiments. Aviral Vaid was involved in fabricating weld samples, and Kaitlin Carson helped me to scan the welding samples through X-ray tomography.

The results of this research are presented in several international conferences. Also, parts of chapters 4 and 5 are published in three different journals: 1) Zareie Rajani, H. R., Phillion, A. B., "A Multi-scale Thermomechanical-Solidification Model to Simulate the Transient Force Field Deforming an Aluminum 6061 Semisolid Weld", *Metallurgical and Materials Transactions B* 46.4 (2015): 1942-1950, 2) Zareie Rajani, H. R., Phillion, A. B., "3D multi-scale modelling of deformation within the weld mushy zone", *Materials & Design* 94 (2016): 536-545, and 3) Zareie Rajani, H. R., Phillion, A. B., "A mesoscale solidification simulation of fusion welding in aluminum–magnesium–silicon alloys" *Acta Materialia* 77 (2014): 162-172.

Check the first pages of these chapters to see footnotes with similar information.

Table of Contents

Abstract	ii
Preface	iii
Table of Contents	iv
List of Tables	vi
List of Figures	vii
1 Introduction	1
1.1 Overview.....	1
1.2 Background.....	2
1.2.1 6061 Aluminum alloys.....	2
1.2.2 Welding.....	3
1.2.3 Solidification defects in welding.....	4
2 Literature review	6
2.1 Solidification.....	6
2.1.1 Fundamentals of solidification in welding.....	6
2.1.2 Modeling of solidification.....	8
2.2 Hot cracking.....	12
2.2.1 Experimental characterization of hot cracking.....	12
2.2.2 Numerical characterization of hot cracking.....	18
2.3 Summary.....	27
3 Scope and Objectives	28
4 Methodology	30
4.1 Overview.....	30
4.2 Solidification module.....	31
4.2.1 Simulation domain.....	31
4.2.2 Thermal analysis.....	36
4.2.3 Solidification.....	38
4.2.4 Coalescence.....	41
4.3 Deformation module.....	42
4.3.1 Internal normal deformation rate.....	44
4.3.2 External normal deformation rate.....	44
4.4 Fluid flow module.....	58

4.4.1	Mathematical approach	58
4.4.2	Numerical implementation	59
4.4.3	Domain and boundary conditions.....	62
4.5	Defect formation module.....	66
4.5.1	Cracks	66
4.5.2	Hydrogen porosity	69
4.6	Welding Experiments	70
4.6.1	Process maps	71
4.6.2	Thermal analysis.....	73
4.6.3	X-ray Tomography	74
4.7	Computation	75
5	Results and Discussion	76
5.1	Solidification	76
5.1.1	Structural analysis of the semisolid weld	77
5.1.2	Effect of welding procedure on semisolid weld characteristics	79
5.2	Deformation of the semisolid weld	83
5.2.1	Internal normal deformation rate.....	83
5.2.2	External normal deformation rate.....	87
5.3	Fluid flow	98
5.4	Defect formation.....	105
5.4.1	Hot cracking	106
5.4.2	Hydrogen Porosity.....	111
6	Conclusions	119
6.1	Conclusion.....	119
6.2	Model limitations.....	121
6.3	Outlook of future use.....	123
	Bibliography.....	124

List of Tables

Table 1.1 Chemical composition limits of AA 6061 [1].	3
Table 1.2 Mechanical properties of AA6061 [1].	3
Table 4.1 Welding parameters and resulting microstructure characteristics.	73

List of Figures

Fig. 2.1 (a) The distribution of the growth rate and the temperature gradient within the weld pool; (b) different growth modes within a single columnar grain in the weld pool [7]. 7

Fig. 2.2 (a) 2D approximation of grains through polyhedrons based on the Voronoi diagram of a random set of nuclei; (b) advancing the grain edges towards the border along a linear segment connecting the nuclei with a Voronoi vertex. The arrow shows the growth direction from a nucleolus towards a border. 11

Fig. 2.3 (a) The configuration of the circular patch test, and (b) the Houldcroft susceptibility test [7]. 13

Fig. 2.4 (a) The configuration of the transverse Vareststraint susceptibility test [52]; (b) a typical Λ -shape curve showing the effect of alloying elements on the hot crack susceptibility of welds [7, 71]. 14

Fig. 2.5 Ductility curve for assessing the susceptibility of weld metals to hot cracking [7]. 17

Fig. 2.6 The 2D differential control volume used by Kou to develop a strain rate-based model of hot cracking [100]. 23

Fig. 2.7 Schematic of two grains and a micro liquid channel within which a hemicylindrical void starts to form [11]. 25

Fig. 4.1 The base geometry and relative position of the RVE at various welding time. 32

Fig. 4.2 (a) Developed geometry of the weld mushy zone for a welding speed of 3 mm/s and welding amperage of 120 A; (b) base metal grains; (c) columnar grains; (d) equiaxed grains at the center of the weld; (e) geometry of weld mushy zone fabricated with different conditions (welding speed of 5 mm/s, welding amperage of 140 A); (f) the same mushy zone as (e) but with longer columnar grains..... 35

Fig. 4.3 Schematic of a primary tetrahedral element..... 36

Fig. 4.4 (a) A reference tetrahedron element showing an arbitrary point (p), the face opposite the i node, subtetrahedron volume (V_{ip}) spanned by the point p and the i face, and also the distance of the point from the i face (h_{ip}). (b) Shows the center of the triangular solidification front, and the geometrical characteristics (the area of the base (A_{ip}), and the height from the apex to the base (H_{ip})) of the subtetrahedrons spanned by the coordinates of the centroid and the faces opposite the nodes 0,1, and 2.....	38
Fig. 4.5 The relation between the solid fraction and temperature for aluminum 6061 using a Scheil approximation within the Thermo-Calc software. Points 1, 2, and 3 and their corresponding images show the growth of the solid phase within the model during cooling.....	39
Fig. 4.6 (a) The geometry of a single micro liquid channel sandwiched between two parallel solidification fronts; (b) the reconstructed network of micro liquid channels for the mushy zone of the weld shown in Fig. 4.2a.....	43
Fig. 4.7 (a) The boundaries of the base metal; (b) Variation in the size of the weld and consequently the shape and size of the base metal geometry due to using different welding parameters; (c) The discretized base metal in 2D.....	47
Fig. 4.8 Various transient regions on the fusion surface separating the base metal from the weld line.....	47
Fig. 4.9 The bar elements used to obtain the local solid fraction within the semisolid weld.....	50
Fig. 4.10 The shrinkage displacement values, $D(x, t)$, at three different points on the fusion surface of a weld fabricated using a welding current of 120 A and a welding speed of 3 mm/s.....	51
Fig. 4.11 The temperature-dependent flow stresses for AA6061 [124, 125].	52
Fig. 4.12 The temperature field within the base metal for a weld fabricated with a speed of 3 mm/s and a current of 120 A.....	53

Fig. 4.13 The decomposition of the global deformation rate vector into external normal deformation rate vectors.....	55
Fig. 4.14 (a) Schematic of a 2D plane inside a micro liquid, and (b) the triangular reference element.	60
Fig. 4.15 Surfaces of the RVE analyzed by the fluid flow module.	63
Fig. 4.16 The 3D view of the whole mushy zone reconstructed by the fluid flow module; (a) welding speed of 2 mm/s and welding current of 100 A, (b) welding speed of 4 mm/s and welding current of 120 A.....	65
Fig. 4.17 The 2D top view of the mushy zone reconstructed by the fluid flow module. Here welding speed is 4 mm/s and welding current is 120 A.	65
Fig. 4.18 Fluid velocity characteristics of a triangular element.	67
Fig. 4.19 Example scanning electron microscopy images showing the measurement methodology for (a) depth of penetration, and (b) weld width.	72
Fig. 4.20 Process maps from welding experiments linking weld characteristics to welding parameters including amperage and speed: (a) Depth of penetration, (b) Weld half-width, and (c) Normalized length of the columnar zone.	72
Fig. 4.21 (a) Experimental setup before welding; (b) Schematic of the location of the thermocouples, and (c) the numerical and experimental thermal histories of the three points shown in part (b).....	74
Fig. 5.1 The gradual evolution of the weld mushy zone as predicted by the model at welding time of (a) 0.2 s, (b) 0.7 s, and (c) 1.8 s. The weld was fabricated using a welding speed of 3mm/s and welding amperage of 120 A.....	78
Fig. 5.2 Process map from a series of simulations examining the effect of equiaxed grain size at the center of the weld on the average width of the micro liquid channels near grains with high f_s	80

Fig. 5.3 Process map from a series of simulations examining the effect of columnar grain length on the average width of the micro liquid channels near grains with high f_s 81

Fig. 5.4 Process map from a series of simulations examining the effect of welding parameters on the average width of the micro liquid channels near grains with high f_s 82

Fig. 5.5 The internal normal deformation rate of the micro liquid channels within the reconstructed mushy zone of a weld for (a) an average solid fraction of 0.66 and (b) an average solid fraction of 0.92. The weld is fabricated by a welding velocity of 4 mm/s and a welding current of 120 A. 84

Fig. 5.6 The cooling rate over the mushy zone of a weld fabricated by a welding travel speed of 4 mm/s and a welding current of 120 A..... 85

Fig. 5.7 The variation of the average internal normal deformation rate as a function of average solid fraction for various welding parameters..... 86

Fig. 5.8 The variation of the maximum cooling rate along the mushy zone of six welds fabricated by different welding parameters..... 87

Fig. 5.9 (a) The lateral component of the force field acting on the fusion surface of the semisolid weld at welding time of $t=1.8$ s; (b) The corresponding distribution of the solid fraction projected on the fusion surface..... 88

Fig. 5.10 The calculated average tensile stress for various welding currents at welding speeds of: (a) 2 mm/s; (b) 3mm/s; (c) 4 mm/s; (d) 5 mm/s. 90

Fig. 5.11 The average tensile stresses on the weld fusion surface under different constraining conditions..... 91

Fig. 5.12 The calculated global strain rate for various welding currents at welding speeds of: (a) 2 mm/s; (b) 3mm/s; (c) 4 mm/s; (d) 5 mm/s. 93

Fig. 5.13 The external normal deformation rate of the micro liquid channels within the reconstructed mushy zone of a weld for (a) an average solid fraction of 0.66 and (b) an average solid fraction of 0.92. The weld is fabricated by a welding velocity of 4 mm/s and a welding current of 120 A and under a restraining strain rate of 0.1 s^{-1} 95

Fig. 5.14 The effect of various welding parameters on the average external normal deformation rate of the mushy zone for three different restraining strain rates: (a) 0 s^{-1} , (b) 0.005 s^{-1} , and (c) 0.1 s^{-1}	97
Fig. 5.15 Cross-sectional distribution of the magnitude of the fluid velocity vector at an average solid fraction of 0.85 for a weld fabricated on a clamped plate with a welding velocity of 5 mm/s and a welding current of 140 A; (a) average columnar length of 250 μm ; (b) average columnar length of 800 μm . The contours on the left show the distribution of the magnitude of the fluid velocity, while the images on the right show their corresponding microstructure.....	98
Fig. 5.16 The variation in the average fluid velocity versus average solid fraction for a weld fabricated by a welding current of 140 A and a welding speed of 5 mm/s under three different external lateral tensile strain rates.....	99
Fig. 5.17 Cross-sectional distribution of pressure at different average solid fractions for a semisolid weld fabricated at a welding speed of 4 mm/s and a welding current of 120 A.....	100
Fig. 5.18 The localization of pressure drop along the mushy zone is shown from the top view of the weld mushy zone.....	101
Fig. 5.19 The variation of the average pressure as a function of average solid fraction for a clamped weld with various welding parameters.....	103
Fig. 5.20 The variation in the average pressure along the weld mushy zone for four different external lateral tensile strain rates. The weld is fabricated at a welding current of 120A and a welding speed of 4 mm/s.....	104
Fig. 5.21 The Kou crack index for different RVE's with different average solid fractions along the weld mushy zone. The welds are fabricated on a plate under an external lateral tensile strain rate of 0.1 s^{-1} with six different sets of welding parameters.....	105
Fig. 5.22 The distribution of new defected channels at three different average solid fractions based on the Kou cracking criterion. The weld is fabricated on a plate under	

an external lateral tensile strain rate of 0.1 s^{-1} with a welding speed of 2 mm/s and a welding current of 120 A.....	107
Fig. 5.23 The variation of the Kou crack index along the mushy zone of a weld fabricated at a welding speed of 4 mm/s and a welding current of 120 A under various external lateral tensile strain rates.....	108
Fig. 5.24 The variation of the surface rupture index along the mushy zone of a weld fabricated at a welding speed of 4 mm/s and a welding current of 120 A under various external lateral tensile strain rates.....	108
Fig. 5.25 The distribution of surface cracks inside a RVE with average solid fraction of 0.7 for a weld fabricated at a welding speed of 4 mm/s and a welding current of 120 A. (a) external strain rate of 0.1 s^{-1} ; (b) external strain rate of 1 s^{-1}	110
Fig. 5.26 The hydrogen porosity index for different RVE's with different average solid fractions along the weld mushy zone. The welds are fabricated on a clamped plate with six different sets of welding parameters. The initial hydrogen content is assumed to be 2 (ml/100gr).	112
Fig. 5.27 The distribution of new defected channels due to hydrogen porosity at three different average solid fractions. The weld is fabricated on a clamped plate with a welding speed of 2 mm/s and a welding current of 120 A. The initial hydrogen content is assumed to be 2 (ml/100gr).....	113
Fig. 5.28 The variation of the hydrogen porosity index along the weld mushy zone for different initial hydrogen contents. The weld is fabricated on a clamped plate with a welding speed of 4 mm/s and a welding current of 120 A.	114
Fig. 5.29 The variation of the hydrogen porosity index along the weld mushy zone for various external lateral tensile strain rates. The weld is fabricated at a welding speed of 4 mm/s and a welding current of 120 A. The initial hydrogen content is assumed to be 2 ml/100gr.....	115
Fig. 5.30 X-ray tomography image of a weld fabricated on a clamped plate at a welding speed of 2 mm/s and a welding current of 95 A.	117

Fig. 5.31 X-ray tomography image of a weld fabricated on a clamped plate at a welding speed of 4 mm/s and a welding current of 120 A. 117

Fig. 5.32 X-ray tomography image of a weld fabricated on a clamped plate at a welding speed of 5 mm/s and a welding current of 140 A. 118

1 Introduction

1.1 Overview

Fusion welding is the process to join metallic components by causing the metal in two adjoining workpieces to reach its melting point. It is fast and efficient, allowing assembly of a single large component from a series of smaller ones. Welding is also economical since the direct production of large metallic components through shape casting processes can be cost prohibitive and accompanied by the formation of defects that result in rejection of the entire component. However, fusion welding defects such as solidification cracks, cold cracks, and porosity can spoil the joint during the welding process. The solidification crack, also called hot crack, is one of the most serious types of imperfection found in a weld and must be prevented. Hot cracks not only reduce the strength of the weld through a reduction in the cross-sectional area, but also reduce the fracture toughness and fatigue strength of the component. They normally appear as straight lines along the centreline of the weld bead, but may occasionally appear as transverse cracking depending on welding conditions.

The susceptibility of metals to hot cracking varies from one material to another. Aluminum alloys in particular require special considerations during welding to avoid the formation of this defect. In the 6XXX series, widely used by industry due to its combination of good strength and ductility, with low density, the joining process remains challenging and it is common for welders to encounter hot cracking. Although filler metals with different chemical compositions have been used over the years to heal hot cracks and aid the welding process, side effects such as galvanic corrosion still aggravate the quality of the weld. In order to control hot cracking in welding, it is necessary to study the solidification of the weld pool along with semisolid deformation and mechanical constraints imposed by the weld geometry. Due to the very high temperatures present in the weld pool, experimental methods for in-situ investigation of solidification phenomena within the weld are limited. Alternatively, numerical methods can be used to investigate new aspects of solidification within the weld pool and also the formation of defects. At present, this field of study suffers from a lack of comprehensive numerical studies. The existing numerical models focus on one of two extremes – either the average properties of the weld at the macro-scale or the micro-

scale phenomena involved in hot cracking during welding. Thus, there is need for a multi-scale model that simulates the various physical phenomena occurring during welding, and leading to the formation of a hot crack through which micro-scale solidification phenomena can be coupled with macro-scale material properties and welding process parameters. This thesis presents a new 3-D multi-scale and multi-physics model that is able to predict the formation of hot cracks within the weld pool of aluminum alloys, with a specific focus on the AA6061 alloy. The use of a multi-scale model enables each grain to exist as a discrete element within the domain while allowing for efficient simulation of an ensemble of grains making up the weld pool. The use of multi-physics enables the coupling of the relevant physics – solidification, deformation, and fluid flow – that result in hot cracking.

1.2 Background

1.2.1 6061 Aluminum alloys

The use of aluminum (Al) alloys in the automotive and aerospace sectors continues to increase with the demand for improved fuel economy, performance and safety, and a cleaner environment through weight reduction [1]. Based on the production method, there are two principal classifications of aluminum alloys, wrought and casting. Wrought aluminum products such as rolled plates, foils, and extrusions have better mechanical properties in comparison with cast alloys. However, cast aluminum products are more cost-effective in fabricating complex shapes as a result of good fluidity and low melting point [2]. Typical alloying elements for aluminum alloys are copper, magnesium, manganese, silicon and zinc. Based on the Aluminum Association (AA) standard, wrought aluminum alloys are categorized into eight groups according to their chemical compositions [1]. In this standard, aluminum alloys are represented by a four-digit number in which the first digit shows what group an aluminum alloy belongs to, and what the major alloying elements are.

The aluminum alloy AA6061 is one of the most commonly-used wrought aluminum alloys. Containing magnesium and silicon as the major alloying elements, this alloy is used for many applications including wings and fuselages in the aerospace industry, pleasure watercraft, automotive components, bicycle frames, and packaging. The chemical composition limits of AA6061 are listed in Table 1.1 [3]. The mechanical properties of this alloy depend strongly

on the heat treatment of the material. AA6061 can be used in either an annealed condition (6061-O) or a solution heat-treated condition. In the solution heat-treated state, the alloy can be naturally (6061-T4) or artificially (6061-T6) aged. The mechanical properties of this alloy for various heat treatments are shown in Table 1.2.

Table 1.1 Chemical composition limits of AA 6061 [1].

Element	Al	Ti	Zn	Cr	Mg	Mn	Cu	Fe	Si
Weight Percentage	Bal.	0.15max	0.25max	0.04-0.35	0.8-1.2	0.15max	0.15-0.40	0.7max	0.4-0.8

Table 1.2 Mechanical properties of AA6061 [1].

Heat Treatment	Ultimate Tensile Strength (MPa)	Yield Strength (MPa)	Shear Strength (MPa)	Elongation (%)
O	124	55	83	25
T4	241	145	165	22
T6	310	276	207	12

1.2.2 Welding

Since direct production of large aluminum components through casting processes can be cost prohibitive and accompanied by the formation of defects, it is usual to join smaller components together rather than produce a single large component directly. Welding processes (*i.e.* fusion welding and solid state welding) are the most common methods for joining aluminum components. In fusion welding, a heat source (e.g. an electric arc, electron or laser beam or a gas flame) melts workpieces to form a small pool of molten material [4, 5]. The “weld pool” solidifies over a short period of time, and the pool becomes strong enough to bond the base metals together. In solid-state welding, such as the friction stir process, melting of aluminum workpieces does not occur, and joining is mainly based on plasticity and mechanical pressure [6]. Although fusion and solid-state welding processes are both used to manufacture aluminum components, fusion welding processes are more common due to their affordability, mobility and reliability [4]. Specifically, arc welding processes such as Gas Tungsten Arc Welding (GTAW) and Gas Metal Arc Welding (GMAW) are the most

common methods to fusion weld aluminum alloys. In the arc welding process, a power supply is used to create an electric arc between an electrode and the base metal. This process has two key parameters affecting the final properties: heat input, and base metal preheating temperature. The heat input is a function of three process parameters: voltage, electric current and the travel speed of the welding torch. Higher voltage and current values increase the heat input since they directly increase the power applied to the system, whereas higher welding speeds reduce the heat input [7] since this will increase the volume of material over which the power is applied.

1.2.3 Solidification defects in welding

Porosity and hot cracking are the two main defects that form during solidification of the weld pool [8].

1.2.3.1 Weld porosity

Porosity refers to the formation of small holes in the weld bead. These pores form because of the significant difference in the solubility of gas (principally hydrogen in aluminum) between the liquid and solid. As the solid phase evolves within the weld pool, gas will be rejected into the liquid phase. Once the gas concentration in the liquid exceeds the liquid's solubility limit, porosity can form [9]. Lowering the amount of the dissolved gas through cleaning the workpiece and using proper shielding gases can prevent the formation of porosity [7].

1.2.3.2 Hot cracks

Hot cracks, which represent cracking of the weld bead, form during the terminal stages of solidification when the solid fraction is close to unity. Several factors are reported to affect the formation of hot cracks during welding [7]. In general, these factors fall under two main categories: 1) mechanical factors, and 2) metallurgical factors. From a mechanics perspective, three major requirements must be met in order for hot cracks to occur: 1) the existence of a semisolid phase called mushy zone that is composed of a network of micro liquid channels and solid grains, 2) deformation of the mushy zone in order to induce a strong pressure drop that initiates cracks within the liquid channels, and 3) a lack of liquid

circulation through the channels to prevent refilling (also called healing) of the initiated cracks [10]. At the last stage of solidification, a continuous network of liquid channels develops along the grain boundaries of the solid phase within the mushy zone of the weld. Due to the concomitant phenomena of solidification shrinkage and externally applied mechanical deformation, fluid flow is thus required to achieve a fully dense solid. The pressure drop inside the channels indicates the difficulty of liquid feeding [11, 12]. Studies have shown that the external deformation significantly affects the flow rate and consequently the pressure drop [13, 14]. An increase in the pressure drop suggests that the liquid flow through the intergranular channels is poor, whereas a lower pressure drop is an indication of easy liquid flow. It has been shown that the pressure drop within a liquid channel depends on the liquid viscosity, the width of the channel and the flow rate within the channel [11, 12]. Higher values of viscosity, and narrow liquid channels all lead to greater pressure drops, lowering the network permeability. If a sufficient pressure drop brings the pressure of the liquid below the required pressure for formation of a cavity, a micro crack may initiate within the channel [15]. The lack of permeability within the semi-solid can also contribute to propagation of the resulting hot crack. Numerical models and experimental techniques are both used to characterize hot cracking and therefore to understand the unknown aspects of this deteriorative phenomenon.

From a metallurgical perspective, hot cracking in welding is strongly influenced by the solidification temperature range, the amount of liquid along the grain boundaries, the interfacial energy between the grain boundary and liquid, eutectic reactions, and the grain structure of the weld metal [7]. These metallurgical factors are linked to the chemical composition of the weld and welding parameters. Studies show that a wider freezing range, *i.e.* the temperature range between the liquidus and the solidus, increases the susceptibility of the weld to hot cracking [16-19]. Further, equiaxed grains hinder hot cracking during welding, as compared to columnar grains [20, 21]. Finally, hot cracks can actually be healed, if sufficient liquid exists along the grain boundaries [19] in the region where the crack formed. The role of these factors is discussed in more detail within the literature review given in the following chapter.

2 Literature review

The study of hot cracking requires knowledge of two key phenomena: 1) the solidification process in which the mushy zone and its semisolid structure form, and 2) the formation of hot cracks within the micro liquid channels of the mushy zone. Over the past decades, extensive experimental and numerical studies have been carried out to investigate these two phenomena in order to obtain new insights into the formation of hot cracks. This chapter reviews these investigations through two separate sections: 1) solidification, and 2) hot cracking. In the first part of this chapter, after discussing the fundamentals of solidification in welding, the existing models of solidification and their ability to reconstruct the semisolid structure are reviewed. The second part of this chapter focuses on the second stage, *i.e.* the formation of hot cracks within the mushy zone. First, the experimental investigations into the formation of hot cracks in welding are discussed. Then, the main hot crack susceptibility tests are introduced, and the experimental findings regarding the effects of various metallurgical and mechanical factors on the formation of hot cracks in welding of aluminum alloys are summarized. Third, various models and criteria that have been developed to describe the hot cracking phenomenon are reviewed. Finally, a summary of previous studies on numerical characterization of hot cracking is presented.

2.1 Solidification

2.1.1 Fundamentals of solidification in welding

The process of solidification plays a key role in the final microstructure and properties that result from fusion welding [7]. The fundamentals of solidification during welding can be examined with respect to two different scales. At micro-scale, the focus is on solidification within a single grain, whereas the focus at the meso-scale is on grain arrangement throughout the cross-section of the weld pool.

The micro-scale solidification analysis for the weld pool covers two main topics: 1) solidification mode, and 2) growth mode. The solidification mode of a single grain depends on the ability of solute elements to diffuse within the liquid and solid phases [22]. In general, due to the relatively fast cooling rate of the weld pool, diffusion within the solid phase is

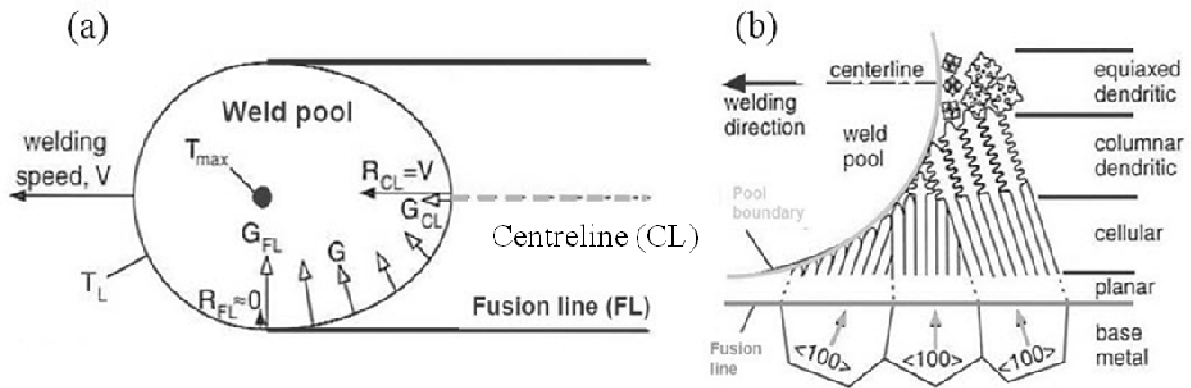


Fig. 2.1 (a) The distribution of the growth rate and the temperature gradient within the weld pool; (b) different growth modes within a single columnar grain in the weld pool [7].

assumed negligible. Moreover, the presence of sufficient convection within the weld pool enables considerable mixing of the solute throughout the liquid phase. Therefore, the solidification mode of a grain during welding is usually considered to be Scheil-like, *i.e.* complete mixing of the rejected solute in the liquid and no diffusion in the solid [7, 23].

The main growth modes observed within a single grain are planar, cellular, columnar dendritic and equiaxed dendritic [24]. In welding, the growth mode of the equiaxed grains is equiaxed dendritic, whereas the growth mode of the columnar grains can be planar, cellular, and/or columnar dendritic [7]. The temperature gradient (G) and growth rate (R) are the two key parameters defining the growth mode. The solidification front tends to grow in a planar mode at high values of G/R . As this ratio decreases to smaller values, the growth mode shifts towards the cellular and finally dendritic growth [25]. Fig. 2.1a shows the variation of the temperature gradient and the growth rate for a single columnar grain as it develops across the weld pool. The temperature gradient is large at the fusion line separating the base metal and the weld, and decreases as the weld centerline is approached. On the other hand, the growth rate significantly drops near the fusion line [7]. Therefore, as shown in Fig. 2.1b, a high value of G/R makes the solidification front grow with a planar mode during the early stages of columnar grain growth. As the columnar grain develops and the solidification front

approaches the centerline, G/R decreases, leading to a columnar dendritic and/or equiaxed microstructure.

Analysis of solidification at the meso-scale concerns the arrangement of grains throughout the cross-section of the weld. Solidification usually starts from the fusion surface and moves towards the centerline, since the interface between the base metal and the molten metal usually acts as a substrate for heterogeneous nucleation [7]. This growth develops a region mainly composed of columnar grains extending from the fusion surface towards the centerline [13]. Near the centerline, the small value of G/R results in constitutional undercooling, allowing equiaxed grains to nucleate and block the growth of the columnar grains [26]. As a result, the microstructure of the weld pool at the meso-scale consists of a columnar zone near the fusion surface and an equiaxed region at the centerline. Due to their detrimental effect on mechanical properties, there is considerable desire to reduce the size of columnar grains within fusion welds of aluminum alloys. The majority of existing techniques for extending the equiaxed zone at the centerline are based on enhancement of the nucleation at the center of the weld [27-29]. For instance, an increase in convection within the weld pool can fragment the columnar dendrites and create additional substrates for the heterogeneous grain nucleation [7]. Large heat inputs and high welding velocities also lower the value of G/R at the centerline and consequently increase the constitutional undercooling, facilitating homogenous nucleation of the equiaxed grains [30].

2.1.2 Modeling of solidification

Modeling of solidification during welding plays a key role in advancing fundamental knowledge of this industrial process. The importance of this type of modeling is a result of two main factors. First, experiments that study solidification during welding are limited due to the presence of high temperatures and also the very short lifetime of the mushy zone. Second, models enable reconstruction of the mushy zone, which aids understanding and subsequent modeling of hot cracking. The reconstruction of the semisolid structure composed of solid grains and liquid films is essential for the modeling of hot cracking since the reconstructed structure acts as the geometry for these models. In the past few years, four major complementary techniques have been developed to model solidification at the scale of the microstructure: front tracking, phase-field, cellular automaton, and granular or discrete-

based methods. These models have been mainly developed for casting processes and only some of them have been adapted for welding. Although all of these models simulate microstructure formation, they use very different techniques [31].

Front tracking models require following the solidification front separating the liquid and solid phases. In these models, the solidification front is tracked by solving the Greens functions for the diffusion problem. Two different numerical methods have been proposed to solve the corresponding diffusion equations: 1) the boundary element method (BEM) in which only the solidification front is meshed [32], and 2) the finite element method (FEM) accompanied by a dynamic remeshing of the entire domain [33]. Front tracking models are accurate but very difficult to implement even in 2D. In addition, these models are not able to handle the coalescence phenomenon, *i.e.* merging of solidification fronts at the terminal stages of solidification. Coalescence is a key factor in controlling hot crack formation. Saito et al. [32] have shown that the front tracking models can successfully model the morphological transition of the solidification front from planar to cellular. Duggan et al. [34] have simulated the solidification process in laser welding through the front tracking technique. Their study shows that the front tracking model can simulate the growth of the columnar grains near the fusion surface.

Phase field models, unlike the front tracking models, do not require an explicit tracking of the solid/liquid interface. As a result, these models are more efficient and capable of reproducing most of the phenomena occurring during solidification [31]. In this modelling approach, the solidification front is represented through continuous variation of the phase-field variable from 0 (liquid) to 1 (solid) over a certain thickness called the thickness of the diffuse interface [35]. Using a free energy or entropy formulation, the equations governing the evolution of the phase-field variable and consequently the semisolid structure are derived and solved using an explicit finite difference method (FDM) [36]. Although this modelling approach has been extensively used to study solidification mechanisms and microstructures in both 2D [68] and 3D [37, 38], it suffers from a major disadvantage. In order to model the diffuse interface, the mesh has to be very small. Therefore, the geometry of this model is usually limited to a micro-scale domain. In comparison to the front tracking method, the phase-field approach is much more commonly used to simulate solidification during welding.

Farzadi et al. [39] have used the phase-field technique to reconstruct the microstructure of the mushy zone at different locations along the fusion surface during GTAW of binary Al-Cu alloys. This study showed that the phase-field model could reflect the effect of welding travel speed on the weld microstructure. Fallah et al. [40] demonstrated the potential of coupling the phase-field method with complex heat transfer conditions to simulate topologically complex microstructures present in laser welding/deposition processes. Zheng et al. [41] successfully predicted the average primary dendrite arm spacing in the weld microstructure during GTAW through phase-field modeling. Montiel et al. [42] have demonstrated the capability of the phase-field method for modeling the columnar-to-equiaxed transition (CET) within the weld microstructure. Their study showed that the size and shape of the columnar and equiaxed regions depend on cooling rate, temperature gradient, and the nature of inoculant particles.

The first two techniques work rather well to reproduce most phenomena associated with microstructure evolution, but as the mesh size must remain small, the simulation is limited to modelling only a few grains due to computational cost. In contrast, the cellular automaton (CA) method has had much success in modelling solidification structure in both 2D and 3D. In this technique, the domain is divided into numbers of cells where each cell is assumed to be either in the solid or liquid state. Based on a solidification rate equation, the solid cells capture their neighbour liquid cells over time, simulating the evolution of solid grains [43]. For welding, this technique has been used to model the competitive growth process between columnar and equiaxed grains, and also to predict the weld microstructure in two dimensions [44]. The CA method has also recently been applied to model hot cracking in welding [45], showing that susceptible sites to hot cracking are normally located along columnar grain boundaries.

The so-called granular model of solidification [11, 12, 46-49] is a recently developed numerical technique in which an assembly of discrete elements is used to simulate equiaxed-globular solidification. The main advantage of this technique is its use of discrete elements, which allows for the simulation of large and non-isothermal mushy zones, as well as inclusion of stochastic effects and solid/liquid interactions [14, 47, 48]. In this model, grains are approximated by polyhedrons based on the Voronoi diagram of a random set of nuclei,

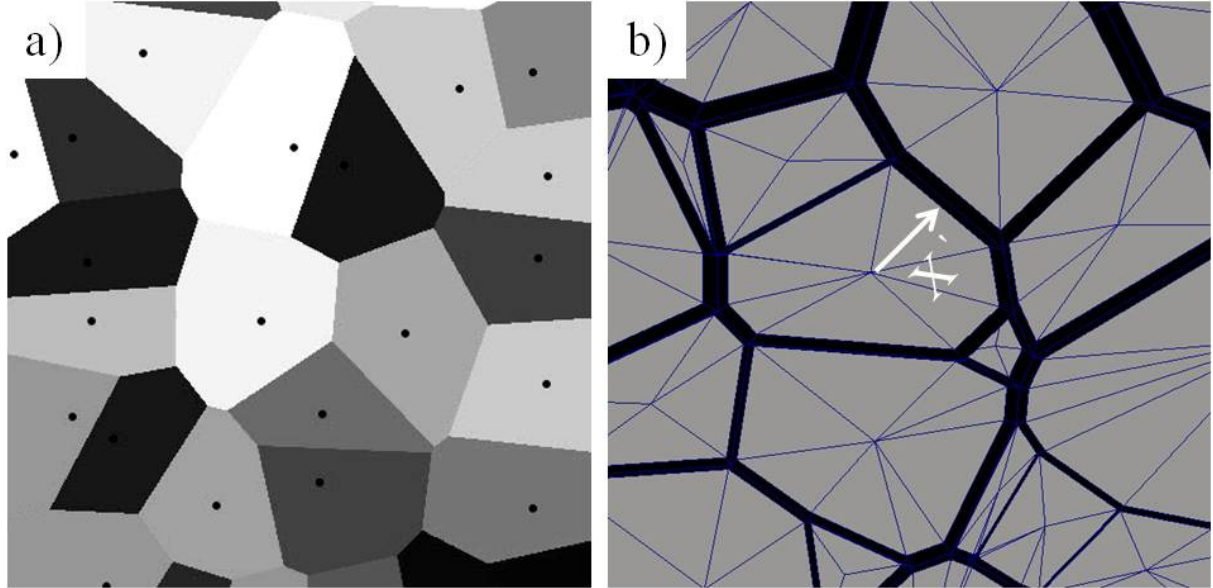


Fig. 2.2 (a) 2D approximation of grains through polyhedrons based on the Voronoi diagram of a random set of nuclei; (b) advancing the grain edges towards the border along a linear segment connecting the nuclei with a Voronoi vertex. The arrow shows the growth direction from a nucleolus towards a border.

resulting in irregular grain arrangements (Fig. 2.2a). As shown in Fig. 2.2b, solidification is then carried out [48] by advancing the grain edges towards the border along a linear segment connecting the nuclei with a Voronoi vertex. Vernède et al. [14, 46, 47] first developed a comprehensive model of this type based on an original idea of Mathier et al. [49] to simulate in two dimensions the solidification sequence and grain percolation of an Al-Cu binary alloy. The authors were able to link the behaviour of the grain network to the macroscopic properties of the semisolid material. Later, Phillion et al. [48] extended this approach to a three-dimensional domain (3D), and showed that the extension to 3D allows for concurrent continuity of both the liquid and solid phases. Concurrent continuity is a key factor in predicting semisolid defect formation. As will be discussed later, granular-type models have also been used by Sistaninia et al. [11, 12], Phillion et al. [50], and Zaragoci et al. [51] to investigate semisolid deformation and crystal rearrangement.

Although the current granular models of solidification have provided much insight into the stochastic microstructure variability, structure transitions from a continuous liquid to coherent solid, and also grain percolation, the basic assumptions of equiaxed-globular

microstructure and uniform cooling rates do not apply in complex casting processes such as die-casting and welding where the solidification kinetics are highly complex. In the case of welding, the fast variable cooling rates containing strong non-linear thermal gradients must be taken into account, along with spatial variations in grain morphology that depend on process parameters.

2.2 Hot cracking

2.2.1 Experimental characterization of hot cracking

Several experimental methods have been developed in order to assess the susceptibility of materials to hot cracking during welding [52-54]. In these tests, the total length of cracks or the length of the biggest crack is usually considered as the susceptibility criterion. The susceptibility tests can be divided into two main categories: 1) Intrinsic tests where hot cracking is caused by only solidification shrinkage and the restraint imposed by the base metal, and 2) Extrinsic tests in which hot cracking in the mushy zone is induced by externally-applied loads.

The patch test is the most common intrinsic susceptibility test for welding [55]. In this test, a circular bead-on-plate weld is fabricated on the base metal plate. As shown in Fig. 2.3a, a centerline hot crack forms at an angle Ω and propagates to the end of the weld. The term Ω is used as the susceptibility index in the patch test. Various versions of this test exist, as discussed by Nelson et al. [56]. Although the patch test is simple and easy to perform, it does not however allow one to study the effect of variation of restraint on hot cracking. The Houldcroft test, also known as fishbone test, is another intrinsic susceptibility test. Unlike the patch test, the degree of restraint can be adjusted in the Houldcroft test. The configuration of this test is illustrated in Fig. 2.3b. In the Houldcroft test, the degree of restraint along the weld line is an experimental variable that is modified by machining slots at the plate edges. The depth of the slots usually increase from a minimum depth on one side to a maximum depth on the opposite side [57]. Such variation in the depth of the slots creates a non-uniform distribution of restraint along the weld. The minimum slot depth with no crack is considered as the susceptibility index in the Houldcroft test.

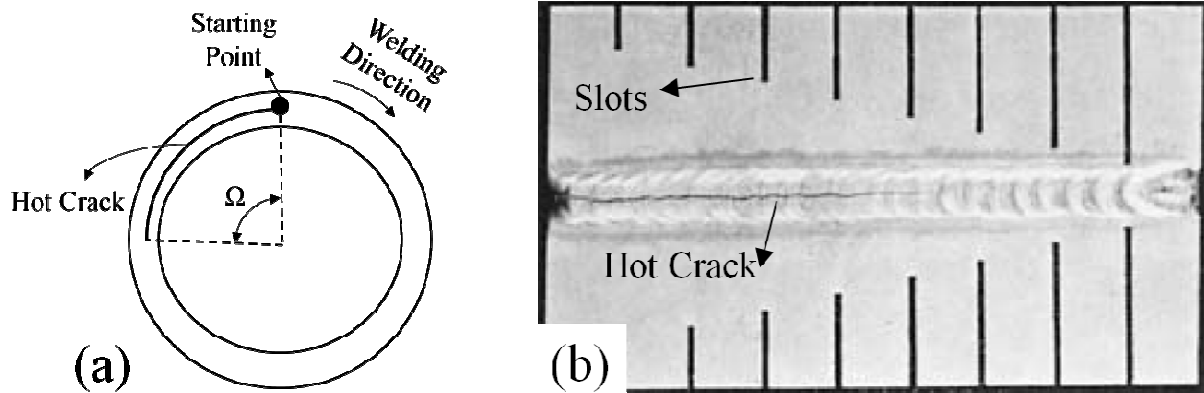


Fig. 2.3 (a) The configuration of the circular patch test, and (b) the Houldcroft susceptibility test [7].

Unlike the intrinsic susceptibility tests, the extrinsic susceptibility tests use an externally applied (augmented) strain, *i.e.* external to the base metal, in order to deform the mushy zone. The Varestraint test is the most common type of extrinsic susceptibility tests for welding. In the Varestraint test, first developed by Savage and Lundin [58], a controlled external load is applied to the base metal in order to bend the plate to a specific angle at an appropriate moment [58] during welding (Fig. 2.4a). The augmented strain is calculated as a function of the radius of curvature and the thickness of the plate, and the corresponding hot tearing susceptibility is quantified by either the total length of the cracks or the length of the biggest crack present in the weld [7]. In the Varestraint test, the base metal plate can be bent either along the weld line or transverse to the welding direction. The latter configuration is known as the transverse Varestraint test in which hot cracks mostly occur inside the weld rather than the outside [7]. The external load in the Varestraint test is applied instantaneously and therefore the role of the strain rate cannot be thoroughly investigated. A second form of the Varestraint test also exists [53, 59], known as the modified Varestraint test or slow bending transverse Varestraint test. In this test, the external load is applied under a controlled rate, enabling one to study the effect of strain rate on the formation of hot cracks. Recently, a number of new extrinsic susceptibility tests have been developed that are able to directly apply tensile strains to the weld rather than bending the base metal plate [53, 60-62]. In these

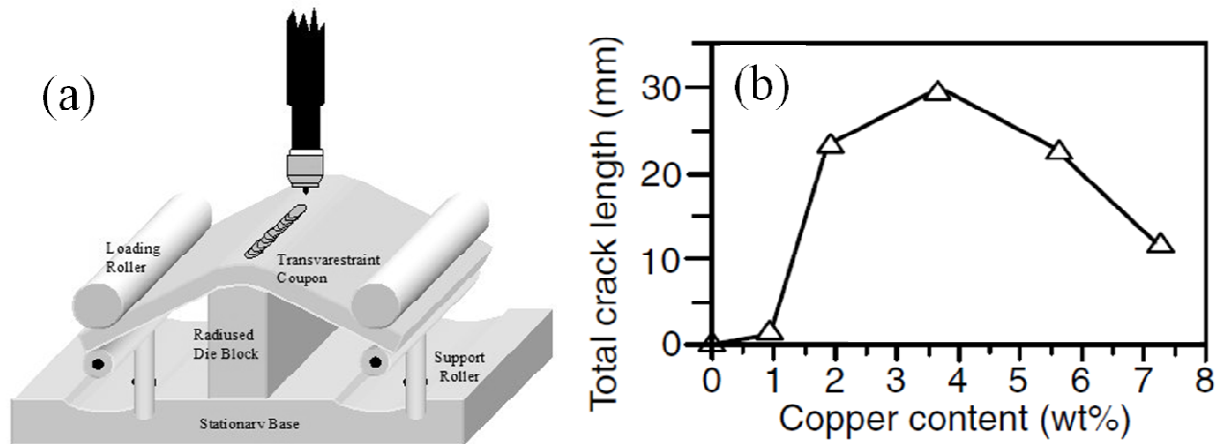


Fig. 2.4 (a) The configuration of the transverse V-restraint susceptibility test [52]; (b) a typical Λ -shape curve showing the effect of alloying elements on the hot crack susceptibility of welds [7, 71].

tests, the tensile strain is either constant [53] or is increased at a specific strain rate during welding [60].

Hot cracking susceptibility tests are widely used to investigate the role of various metallurgical and mechanical factors in the formation of this defect during welding of aluminum alloys. Studies show that in aluminum alloys, hot cracking is strongly affected by the chemical composition of the weld, the weld microstructure, and the level of restraint and deformation during welding [63-65]. The role of alloy composition in hot cracking is mainly shown through its effect on the weld's freezing range [20, 66-72]. Dudas and Collins [70] have reviewed several studies on the role of alloying elements on hot cracks formation. As discussed in their review, the occurrence of hot cracking is minimal when welding pure aluminum alloys as well as highly-alloyed aluminum alloys that contain no less than 6 wt% solute. The maximum susceptibility to hot cracking then occurs somewhere between these two extremes. Michaud et al. [71], Dowd [68], and Pumphrey et al. [67], have all reported similar results for Al-Cu and Al-Mg-Si alloys, showing that the hot cracking sensitivity increases to a maximum value at 4 wt% copper (~ 1 wt% magnesium in Al-Mg-Si), and then decreases at higher contents of solute, forming the so-called Λ -shape curve shown in Fig. 2.4b. The features of the Λ -shape curve are associated with the freezing range and eutectic reactions in aluminum alloys. For pure aluminum, the metal freezes at a unique temperature

and hence the freezing range is nil. Consequently, hot cracking does not occur. The addition of alloying elements first increases the freezing range, which leads to an increase in hot cracking susceptibility, but then also increases the amount of eutectic, which leads to a decrease in hot cracking susceptibility as the eutectic reaction can eliminate the liquid films in which solidification defects occur. It is discussed in [7] that an increase in the freezing range results in an increase in the time that a semisolid is exposed to external deformations, and therefore more strain accumulates especially at higher fraction solid where the material is brittle. Higher levels of strain accumulation can eventually lead to the formation of hot cracks [14]. For highly alloyed aluminum, a significant amount of eutectic and consequently the presence of abundant liquid at the grain boundaries just prior to complete solidification can heal micro cracks, reducing the hot crack sensitivity.

Other studies have shown that the chemical composition of the weld also affects hot cracking through its effect on the solid/liquid interfacial energy [20, 7]. Specifically, when the solid/liquid interfacial energy is small, continuous liquid films will form at the grain boundaries, increasing the crack sensitivity. However, when this interfacial energy is large, the ability of the grain boundary liquid to wet the solid grains decreases, leading to the formation of a discontinuous film of liquid along the grain boundaries. Such discontinuous liquid films improve the hot crack resistance of the semisolid structure. Nakata and Matsuda [20] have observed that aluminum alloys containing magnesium show lower crack sensitivity as a result of having higher solid/liquid interfacial energy.

In addition to the chemical composition of the weld, studies have shown that hot cracking during aluminum alloy welding is strongly affected by the weld microstructure [7, 20]. Specifically, equiaxed grains have higher resistance to hot cracking in comparison with columnar grains [7]. This observation is linked to the fact that equiaxed grains can deform more easily and accommodate more strain. Also, liquid feeding and healing along the columnar grains is more difficult since they have longer travel distances for the grain boundary liquid [11, 12]. Nakata and Matsuda [20] have shown that refinement of equiaxed grains can provide a greater grain boundary surface area that reduces the concentration of the deteriorative low-melting-point segregates along the grain boundaries [7]. Also, grain size directly influences the strain distribution across the mushy zone. Grain refinement increases

the number of grain boundaries in a given volume and consequently reduces the amount of strain seen by each boundary. In separate studies, Mousavi et al. [73], Warrington et al. [74], and Dvornak et al. [21] each demonstrated that a reduction in aluminum alloy hot crack susceptibility could be achieved through the addition of grain refiners. It was also shown that grain refinement increases the ductility of Al-Cu semisolid welds [75].

Many studies have shown that strain and strain rate also affect hot cracking in welding (e.g. [76, 77, 62]). The deformation of the mushy zone during welding primarily comes from self-induced sources including solidification shrinkage in the weld pool and thermo-mechanical stresses from the base metal. This strain can be also augmented through application of external loads. Nakata and Matsuda [20] have shown that the temperature range in which the mushy zone is susceptible to hot cracking, also called the brittle temperature range (BTR), is a function of both the alloy's chemical composition and also the amount of strain accumulated within the mushy zone. They have used the transverse Varestraint test to investigate this relationship and determined the so-called ductility curve shown in Fig. 2.5. This curve demonstrates the brittle temperature range at different values of strain. The brittle temperature range at each strain varies from the liquidus temperature to the temperature measured at the tip of the longest crack. In general, the narrower the curve is, the more weldable the material is. The ductility curve reveals that hot cracking does not happen unless there is a minimum strain (ϵ_{min}) deforming the mushy zone. For some materials, the required minimum strain is very small and therefore the modified transverse Varestraint test should be used to determine the ductility curve [7]. This study also showed that the dynamics of the strain accumulation within the mushy zone, *i.e.* the strain rate, is more important than the final amount of accumulated strain. As can be seen in Fig. 2.5, if the strain accumulates at a slow rate, such that at each strain increment the temperature of the mushy zone has sufficient time to drop below the brittle temperature range, then hot cracking will not occur. In other words, there is a critical ratio of strain rate to cooling rate ($\frac{\dot{\epsilon}}{\dot{T}} = \frac{d\epsilon}{dT}$) above which hot cracks can form. This ratio equals the slope of the tangent to the ductility curve ($\frac{d\epsilon}{dT}$) and is called the critical strain rate for temperature drop (CST). The results of Nakata and Matsuda's study suggest that hot cracking in welding can be prevented by lowering the strain rate or increasing the cooling rate of the weld. Yang et al. [78] have managed to stop hot cracking in

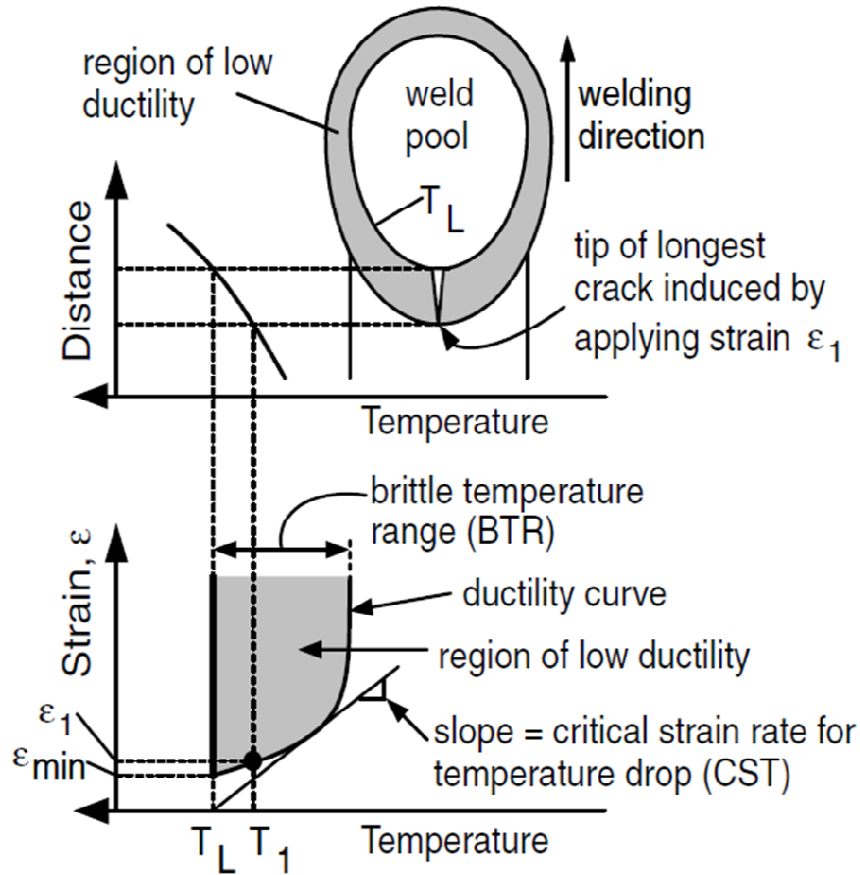


Fig. 2.5 Ductility curve for assessing the susceptibility of weld metals to hot cracking [7].

GTAW of 2024 aluminum alloys by applying liquid nitrogen to the mushy weld in order to drastically increase the cooling rate. Other experimental studies confirm the role of strain rate in hot cracking [76, 60]. Arata et al. [76] have reported critical strain rate values of $0.25\% \text{ s}^{-1}$ and $0.1\% \text{ s}^{-1}$ for hot cracking in arc welding of Al-Mg-Si alloys and Al-Cu alloys respectively. Cross et al. [60] have also shown that the critical strain rate in welding of aluminum alloys can vary as a function of the chemical composition of the weld, the type of the susceptibility test, and also welding speed. Their study reveals that the critical strain rate for hot cracking in welding of aluminum alloys does not exceed $5\% \text{ s}^{-1}$.

Welding process parameters including welding travel speed and welding power also affect hot cracking since these parameters result in changes in the cooling rate, the weld microstructure, and the self-induced strain that comes from thermo-mechanical stresses

during welding. This relationship has been extensively studied [77, 79-84], but is not well understood yet. Matsuda et al. [77] have reported that, in aluminum alloys, increasing the travel speed from 2.5 mm/s to 13 mm/s during GTAW can improve the hot cracking resistance. This finding results from the fact that higher welding travel speeds increase the cooling rate and promote formation of equiaxed grains [7], which are less susceptible to hot cracking. Furthermore, experimental investigations by Chihoski [70, 80] showed that at high welding travel speeds, a compressive stress field forms near the mushy zone, preventing hot cracking. However, at low welding travel speeds, the stress field is tensile, not compressive, facilitating the formation of hot cracks. Niel et al. [84] showed that for a constant welding current in GTAW, increasing the welding travel speed can prevent hot cracking in welding of AA 6061 aluminum alloys. Their study also revealed that for a constant welding travel speed, higher welding currents increase hot cracking susceptibility.

As discussed above, while experimental techniques provide valuable hot cracking criteria for welding, they cannot explain the complex multi-scale/physics phenomena involved in the mechanisms behind hot cracking. The high temperature condition in welding and the very short lifetime of the weld pool restrict the use of experimental methods for investigating transient phenomena during welding including solidification and defect formation.

2.2.2 Numerical characterization of hot cracking

Numerical methods have been widely applied as an alternative approach to experimentation in order to gain better insights into the formation of hot cracks in semisolid structures. In these numerical studies, various models have been proposed based on different criteria. Numerical models of hot cracking were mostly developed for casting processes, relate the mechanisms of hot cracking to state variables such as stress, strain, strain rate, and chemical composition, and are thus implemented within the framework of a mathematical process model. Although some of these models have been adapted for welding, modeling of hot cracking in welding still remains challenging. This is for two reasons. First, the complex nature of the transient thermo-mechanical stresses that deform the weld mushy zone creates additional complications for process modelling of welding. Second, welding involves several process parameters, making mathematical modeling more difficult. In this section, numerical models for hot cracking in semisolid structures will be reviewed. A summary is then made to

show which of these models has been extended to welding. In order to be able to compare the features of these models, they are divided into three categories based on the length-scale in which they govern the hot cracking phenomenon: 1) macro-scale models, 2) micro-scale models, and 3) multi-scale models. These categories are further subdivided based on the hot cracking criteria used in these models.

2.2.2.1 Macro-scale models

Macro-scale models treat the semisolid structure as a single-phase material, through the use of averaging methods. These models usually assume that hot cracking occurs once the average value of a state variable such as the stress, strain, or strain rate across the mushy zone exceeds a critical value. Therefore, these models do not consider the micro-scale phenomena involved in hot cracking and see the mushy zone as a macro-scale domain without any internal features. For the same reason, macro-scale models cannot predict the variation of hot cracking susceptibility across the semisolid structure, *i.e.* the localization phenomenon. These models can be further divided into the following groups based on the state variable used to predict hot cracking:

2.2.2.1.1 Stress-based models

Stress-based models assume that hot cracking occurs within the semisolid structure once the average stress acting on the semisolid exceeds a critical value representing the strength of the semisolid structure. This assumption is supported by several experimental and numerical studies [79, 80, 85]. Zacharia [85] showed that the tensile stress along the weld mushy zone facilitates the formation of hot cracks. Chihoski [79, 80] studied the effect of the stress field near the weld mushy zone on hot cracking, demonstrating that welding parameters vary the stress field deforming the mushy zone and consequently enhance or diminish hot crack susceptibility. These models are simple criteria, relating the hot cracking susceptibility to a critical average semisolid stress value known as fracture stress, *i.e.* σ_{fr} [86]. Dickhaus et al. [87] linked the fracture stress of the semisolid structure to the surface tension of the liquid, γ , and the average liquid film thickness within the semisolid structure, h_{ave} ,

$$\sigma_{fr} = \frac{2\gamma}{h_{ave}} . \quad (2.1)$$

Lahaie et al. [88] then modified Eq. (2.1) to also consider the effects of solid fraction, f_s and the accumulated strain, ε ,

$$\sigma_{fr} = \frac{4\gamma}{3h_{ave}} \left(1 + \left(\frac{f_s^m}{1 - f_s^m}\right)\varepsilon\right)^{-1} \quad (2.2)$$

where m is a microstructural configuration parameter that equals 1/3 for 3D equiaxed semisolid structures and 1/2 for 3D columnar semisolid structures.

2.2.2.1.2 Strain-based models

Strain-based models, initially proposed by Pellini [89] and Magnin [90], assume that hot cracking is controlled by the amount of strain accumulated within the semisolid structure. These models propose that excessive semisolid deformation during welding due to the externally-applied strains, as well as self-induced strains caused by solidification shrinkage and thermo-mechanical strains, facilitates hot cracking. The strain-based models introduce a critical amount of accumulated strain for the semisolid structure, called fracture strain (ε_{fr}), above which the semisolid structure is likely to contain a hot crack. The strain-based criterion for hot cracking during welding is well supported by several studies. Matsuda et al. [91, 92] have shown that tensile strains within the weld mushy zone induce hot cracking during welding. Ploshikhin et al. [93] demonstrated that welds with hot cracks are associated with a higher amount of accumulated strain along the weld centerline.

2.2.2.1.3 Strain rate-based models

Initially proposed by Prokhorov [94] and Feurer [95], the hot cracking models that use the strain rate as the critical parameter are based on the idea that semisolids crack once the average strain rate rises beyond a critical value. In other words, if the semisolid structure does not have sufficient time to accommodate the accumulated strain, it becomes susceptible to hot cracking. Strain rate-based models that are developed for a macro-scale context treat the semisolid structure as a single phase with average properties and are based on the concept of shrinkage-feeding theory.

In hot cracking literature, the shrinkage-feeding theory is the idea that hot cracking occurs once liquid feeding is insufficient to compensate the average shrinkage within the semisolid structure [96-98]. A very common approach in these models [97] introduces two rate concepts: 1) rate of feeding (ROF), and 2) rate of shrinkage (ROS). ROF is the rate at which the semisolid structure is fed by the molten metal, and is a function of several physical parameters such as solid fraction, temperature, and dendrite arm spacing. In general, an open semisolid structure with larger liquid channels has higher rates of feeding. For instance, lower solid fractions and higher amounts of eutectic phase can lead to an open structure and therefore faster feeding [96]. ROS is a function of strain rate within the semisolid induced by solidification shrinkage, thermo-mechanical strains, and also externally-applied (augmented) strains. Higher strain rates and consequently larger ROS generate more empty space within the semisolid structure that has to be filled by the molten metal in order to avoid hot cracking. The outcome of the shrinkage-feeding theory of hot cracking is that a semisolid is susceptible to hot cracking if $ROS > ROF$.

Traditionally, other strain rate-based models such as the well-known RDG model [99] and the newly-introduced Kou's model [100] have been also classified as macro-scale models. However, as will be discussed in section 2.2.2.2, these models have underlying micro-scale characteristics that can be exploited in the multi-scale modeling of hot cracking. Therefore, this study classifies these strain rate-based models as micro-scale models and will discuss them in the following section.

2.2.2.2 Micro-scale models

Unlike the macro-scale models, micro-scale models focus on the phenomena that happen in at the level of the grain and grain boundary to create a hot crack. These models usually involve local differential terms rather than average terms, with local terms that are defined over a micro-scale domain within the mushy zone. Usually, this micro-scale domain is a micro liquid channel and the local terms are the flow rate, pressure, dissolved gas pressure, strain, and strain rate within the channel. Although micro-scale models enable one to consider the local properties of the mushy zone rather than the average properties and therefore study the localization phenomenon, they are not easy to implement. This is because micro-scale models require calculation of the local terms, which in turn requires knowledge

of the boundary conditions that can be applied to the micro-scale domain. These boundary conditions are unknown unless the models are integrated over the entire length of the mushy zone. Unfortunately, integration introduces average properties, and thus eliminates the potential of micro-scale models to simulate the localization phenomenon that results in a hot crack. Because of this integration, these models are traditionally classified as macro-scale models. However, as presented below, micro-scale models can be implemented within multi-scale solidification models. This will eliminate the need for integration, and thus preserves the micro-scale characteristics of these strain rate-based models. Micro-scale models of hot cracking can be divided into two categories:

2.2.2.2.1 Strain rate-based models

Some of the strain rate-based models of hot cracking are developed upon conservation of mass, and hence account for strain rate through a direct term rather than ROS, which is a function of strain rate. These models assume that a micro liquid channel cracks once the continuity condition inside the channel is disturbed [12, 99-100]. According to these models, the local flow rate must compensate for the strain rate applied to a channel in order to prevent hot cracking, similar to the shrinkage-feeding criterion, but with a direct role for the local strain rate. Using Darcy's law for the liquid channel, which links the local flow rate to the pressure drop inside the channel, these models also account for another important term, *i.e.* the pressure drop within the micro liquid channel that may result in crack formation. These terms together allow for the strain-rate based models to assess the susceptibility of the semisolid structure to hot cracking. Some of the main strain rate-based models that are developed upon the mass balance theory are reviewed below.

Rappaz et al. [99] have developed the so-called RDG hot cracking criterion based on a mass balance performed over the entire columnar semisolid structure, linking the pressure drop within the liquid films of the semisolid to both the local flow rate of the channel and the separation rate of the channel walls. According to this strain rate-based criterion, if the local strain rate and the local flow rate induce pressure drops that are greater than a given cavitation pressure drop, then the mushy zone is prone to hot cracking. Drezet et al. [101], amongst others, have implemented the RDG criterion into process models in order to study the formation of hot cracks during welding of aluminum alloys.

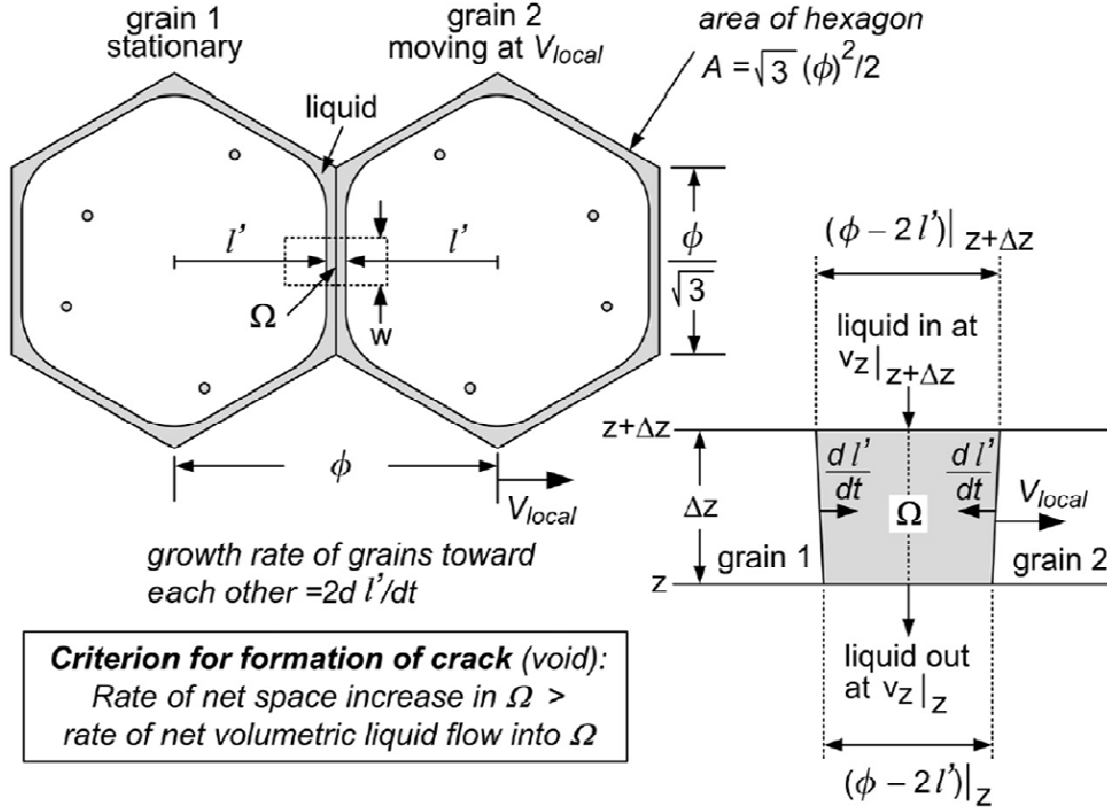


Fig. 2.6 The 2D differential control volume used by Kou to develop a strain rate-based model of hot cracking [100].

Recently, Kou [100] applied a similar mass balance technique to develop a partial differential equation governing the formation of hot cracks within a micro liquid channel. The principles of this model are similar to the theory behind the RDG model, but focus instead on the grain boundary instead of the semisolid structure as a whole. Fig. 2.6 illustrates the 2D differential control volume used by Kou to develop this strain rate-based model. Kou's model shows that at high solid fractions, a micro liquid channel undergoes hot cracking if the separation rate of the channel walls exceeds the growth rate of the walls and the local feeding rate combined. In another word,

$$\frac{d\varepsilon_l}{dt} > (1 - \beta)^m \frac{df_s^m}{dT} \frac{dT}{dt} + \frac{d((1 - (1 - \beta)^m f_s^m) v_l)}{dz'} \quad (2.3)$$

where $\frac{d\varepsilon_l}{dt}$ shows the local strain rate perpendicular to the flow direction, z' , caused by both self-induced and externally applied (augmented) strains. The first term on the right hand side represents the growth rate within the channel due to solidification, while the second term is associated with the feeding rate inside the channel. In this equation, ε_l is the local strain perpendicular to the grain boundary and therefore the flow surface, t , β , T , and f_s denote time, shrinkage factor, temperature, and solid fraction, respectively, v_l represents the 1-D local flow rate within the channel, and m is a microstructure parameter with value of 0.5 for a 2D domain and 0.333 for a 3D domain. In this model, the liquid channel cracks once the opening rate of the intergranular space exceeds the liquid feeding rate. Unlike the RDG model in which the differential control volume consists of both the liquid films and the solid grains, the Kou model focuses on only the micro liquid channels. Thus, the governing partial differential equation (PDF) is a single-phase differential equation and not a two-phase equation.

2.2.2.2 Gas-induced liquid rupture models

Most of the models discussed above do not directly account for the role of liquid rupture in hot cracking, *i.e.* the formation of a vapour-liquid interface. Only in some of the strain rate-based models such as the RDG, is the liquid rupture phenomenon indirectly considered. In these models, the critical pressure drop for cavitation accounts for nucleation of a vapour-liquid interface. According to the classical nucleation theory, a vapour bubble forms once the pressure drop is large enough to provide sufficient energy for the formation of a vapour-liquid interface. The values of the cavitation pressure drop measured through experiments are however significantly lower than the values predicted by the nucleation theories [102-104]. Several studies suggest the involvement of other mechanisms such as the contribution of dissolved gas to the cavitation pressure drop [102, 105-107]. Campbell [102] has shown that in the presence of dissolved gas inside the micro liquid channel, a pore is stable if

$$P_g - P_l \geq \frac{2\gamma}{r} \quad (2.4)$$

where P_l and P_g are the local pressure and the partial gas pressure inside the micro liquid channel, respectively. γ is the liquid surface tension, and r denotes the radius of the pore. Eq.

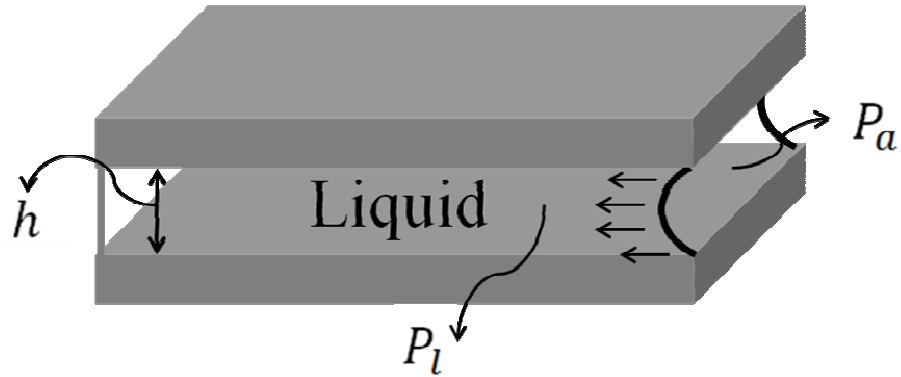


Fig. 2.7 Schematic of two grains and a micro liquid channel within which a hemi-cylindrical void starts to form [11].

(2.4) shows that high partial gas pressures or low local pressures due to high pressure drops can lead to the formation of gas porosity within the micro liquid channels of a semisolid structure. In other words, the presence of dissolved gas can lower the critical cavitation pressure drop for liquid rupture, facilitating the formation of both porosity and hot cracks. This theory is supported by several studies [108-110]. Lee et al. [108] have shown that lowering the level of dissolved hydrogen [102, 109] can reduce the formation of porosity in casting of aluminum alloys. Dixon [110] has shown that hot cracks in welding occur because of gas porosity, and higher pore densities increase the susceptibility of the weld to hot cracking.

The liquid within the semisolid structure can also rupture due to propagation of atmosphere-liquid interface into the micro liquid channels. Based on the overpressure required to overcome capillary forces at the atmosphere-liquid interface, Sistaninia et al. [11] have used a propagation criterion for a hemi-cylindrical void shown in Fig. 2.7,

$$P_a - P_l \geq \frac{2\gamma \cos\phi}{h} \quad (2.5)$$

where P_a and P_l represent the atmospheric pressure and the local pressure of the micro liquid channel, respectively, ϕ denotes the dihedral angle, and γ and h are the liquid surface tension and the thickness of the micro liquid channel. Considering that a thin oxide skin has formed on the atmosphere-liquid interface, and based on the measurements reported by Syvertsen

[111], Sistaninia et al. [11] have shown that the $\gamma\cos\phi$ value can be fixed to 5 Jm^{-2} for aluminum alloys for channels containing an oxide skin, *i.e.* at the component's surface, and 2 Jm^{-2} for interior channels without an oxide skin.

2.2.2.3 Multi-scale models

The models of hot cracking discussed above are either defined in a macro-scale domain and based on the average properties of the semisolid or are limited to the scale of micro. Therefore, none of these criteria alone can model the hot cracking phenomenon in a multi-scale context where the localization phenomena can be observed. Multi-scale modelling of solidification, including the well-known cellular automaton approach for microstructure development (e.g. [45, 112,113]) and more recently the granular modelling approach (e.g. [11, 12, 14]), is useful for understanding the relationships between phenomena occurring at different length-scales. Micro-scale models of hot cracking, like Rappaz's and Kou's criteria, appear to suite multi-scale modelling of solidification since they can be applied to each micro liquid channel within a representative network of channels to examine local hot cracking susceptibility. However, as discussed in section 2.2.2.2, in order to implement micro-scale hot cracking models, the local characteristics of a single micro liquid channel, *i.e.* the local deformation and flow rate, have to be determined. Vernède et al. [14] and Sistaninia et al. [11, 12, 114] have developed a sophisticated numerical method for multi-scale modelling of hot cracking during casting. Following reconstruction of the network of micro liquid channels using a granular model of solidification as discussed in Section 2.1.2, they simulated the local flow rate [12] and the separation rate of the walls of every single channel [11]. Similar studies in welding are less advanced. Cross et al. [115] modeled the separation of grains during welding using a simplified 2D structure with horizontal and vertical micro liquid channels. Bordreuil et al. [45] predicted the local characteristics of the micro liquid channels during welding using a 2D replica of the mushy zone developed by cellular automata. However, the results were limited by the use of 2D geometry, which both induces discontinuity in the liquid network [116], and poorly represents the morphology of the solidifying weld microstructure. Also, these models did not consider the effects of external thermo-mechanical forces on the deformation of the micro liquid channels, and therefore cannot yield the deformation characteristics of the channels in a self-restrained welding

condition. The mentioned shortcomings indicate the necessity of a new multi-scale model to improve the numerical study of the solidification cracking in the weld pool.

2.3 Summary

As shown through the literature presented in this chapter, a large number of experimental and numerical studies have been conducted to investigate hot cracking in welding. Specifically, several numerical models have been developed to overcome the experimental limitations and consequently explore new aspects of the formation of hot cracks during welding. These models are usually inspired by similar studies for casting processes and suffer from several shortcomings. First, the existing models are limited to either a macro-scale domain involving the average properties of the weld or a micro-scale domain at the level of grain boundaries. Second, these models are not able to comprehensively correlate welding process parameters and the phenomena behind hot cracking. Hence, there is need to develop a new multi-scale model of hot cracking for welding in order to obtain new insights into the formation of hot cracks. Such a multi-scale model will relate micro-scale phenomena to welding processes, revealing the role of process parameters in the formation of hot cracks during welding.

3 Scope and Objectives

As shown in Chapter 2, only a few numerical models have been developed to study the formation of hot cracks during the process of fusion welding. These models are all based on the macro-scale approaches that consider the mushy zone of a solidifying weld pool as a single phase with average properties. Although some of the previously-developed hot cracking criteria have the potential to shift from average modelling to multi-scale modeling of hot cracking in welding, they have not yet been exploited in this fashion since the required local information within the mushy zone such as the local strain rate and local flow rate remain unknown. Thus, the existing hot cracking models in welding have only been used to benchmark hot cracking susceptibility of a weld through the calculation of average properties (e. g. average pressure, effective stress, and effective strain rate). Consequently, they cannot separately model the different stages of hot cracking.

In other industrial solidification processes, such as casting, averaging methods and granular models have provided considerable insight into hot crack formation. However, these methods are not designed for welding, and the different microstructural, thermal and also mechanical features of welding hinder the direct application of such approaches to welding. Moreover, none of these models are able to consider a comprehensive range of factors, and most of them only focus on a limited window of parameters.

The above constraints show the necessity of developing a new multi-scale model to improve the numerical study of hot cracking within the weld pool. This study intends to bridge this gap through creation of a 3D numerical model that is able to examine hot cracking during welding within a multi-scale context, *i.e.* that considers the collective solidification and deformation of an ensemble of grains as well as the fluid flow characteristics of the semisolid weld. This research pursues three main objectives:

- The development of a new multi-scale model that is able to simulate the solidification process within a weld pool in a three-dimensional domain. The model should reconstruct the semisolid structure as a function of welding process parameters.

- The development of a new multi-physics model that is able to simulate deformation and fluid flow within the mushy zone during welding.
- Assessment of the susceptibility of the weld to hot cracking under different processing conditions.

This model will be developed for the wrought aluminum alloy AA 6061 due to its relative susceptibility to hot cracking during welding, and its wide industrial application.

4 Methodology

4.1 Overview

The proposed multi-scale and multi-physics model simulating defects during welding of AA6061 requires the development of four co-related modules: 1) solidification, 2) deformation, 3) fluid flow, and 4) defects. These modules are briefly outlined below:

- **Solidification module:** In this module, a discretized geometry reconstructing the weld mushy zone, consisting of both columnar and equiaxed grains, is created in a multi-scale context. This unstructured grid represents the microstructure of the weld mushy zone, and varies as a function of welding process parameters. Then, solidification during welding is simulated. At any welding time, the solidification module outputs the corresponding 3D structure of the weld mushy zone composed of solid grains and a network of micro liquid channels.
- **Deformation module:** This module numerically simulates deformation of the mushy zone during welding. The deformation module accounts for both externally applied (augmented) strains, and self-induced strains including solidification shrinkage and thermo-mechanical strains. The input to this module is the solidification shrinkage, calculated using the solidification module. Then, the finite element method is applied to predict the transient thermo-mechanical strains during welding. The output of this module is the local strain rate within each micro liquid channel, *i.e.* the separation rate between the walls of the channel, as a function of welding conditions.
- **Fluid Flow module:** This module characterizes the flow of liquid metal through the weld mushy zone. The model uses as input the local strain rate data from the deformation module and the geometric description of microstructure from the solidification module. Then, the finite element method is applied to calculate the pressure field within the mushy zone during welding. The output of the fluid flow module is the local pressure within each micro liquid channel.
- **Defect Formation module:** In this module, defect formation models from the literature [12, 100] have been applied to the output of the combined solidification, deformation,

and fluid flow modules in order to predict the formation of micro cracks and micro porosity within the weld mushy zone as a function of process parameters.

The details of the techniques used in each module are presented in this chapter. Sections 4.2 to 4.5 present the numerical simulation methods. Section 4.6 outlines the welding experiments performed to provide input information related to the grain structure occurring under different welding conditions, along with image analysis performed to quantify the formation of micro cracks and micro porosity during welding.

4.2 Solidification module¹

This module uses the granular model of solidification to reconstruct the semisolid structure of the weld mushy zone. Four milestones were achieved to develop a solidification module applicable to welding: 1) developing a simulation domain, 2) thermal analysis, 3) simulation of solidification, and 4) modeling the coalescence phenomenon in which neighbour solid grains bridge to form a coherent solid phase. Each of these steps is discussed below.

4.2.1 Simulation domain

4.2.1.1 Overview

The representative volume element (RVE) for simulating microstructure evolution in the weld pool at the multi-scale is illustrated in Fig. 4.1. The RVE defines the simulation domain, and can be described through both its macroscopic and microscopic characteristics.

At the macro-scale, the simulation domain has to encompass the weld zone, and therefore, the size of the RVE is determined from the depth of penetration and width of the weld assuming a parabolic cross-sectional fusion zone. A small amount of base metal is also included in order to simplify the geometry; creating a cuboid domain. The white dashed cube in Fig. 4.1 indicates the shape and position of the RVE with respect to time and the position of the weld torch. The origin of the RVE is denoted by O , the penetration depth and width of the weld respectively lie along the X and Y directions, and the Z direction follows the line of

¹ This section has been published in : Zareie Rajani, H. R., Phillion, A. B., “A mesoscale solidification simulation of fusion welding in aluminum–magnesium–silicon alloys” *Acta Materialia* 77 (2014): 162-172.

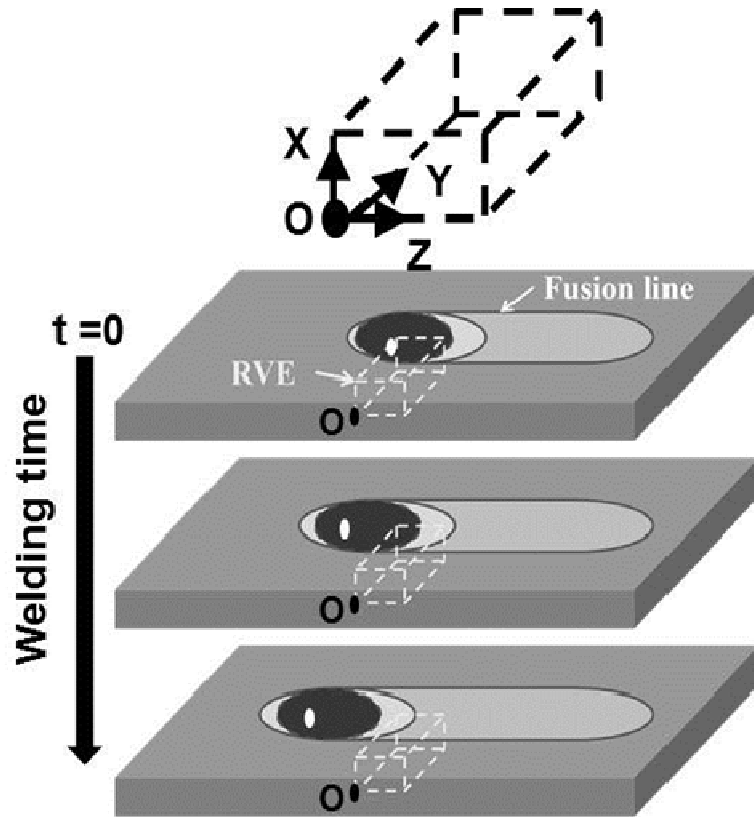


Fig. 4.1 The base geometry and relative position of the RVE at various welding time.

welding. The RVE covers one-half of the weld, and at the beginning of the analysis (welding time equals zero), the weld centre, identified by a small white circle in Fig. 4.1, is assumed to be located at an arbitrary position of $X=1$, $Y=1$, and $Z=0$. With time, the weld torch advances, moving through then out of the RVE, creating transient conditions for solidification.

At the scale of the microstructure, the simulation domain described by the RVE contains a substructure consisting of base metal equiaxed grains, equiaxed fusion zone grains near the weld centre and columnar fusion zone grains at the interface with the base metal to represent the actual microstructure of the weld [7]. Such a substructure enables simulation of the evolution of the weld microstructure during solidification. As discussed in section 4.2.1.3, the substructure is further refined through discretization of the RVE using an unstructured meshing technique.

Not surprisingly, welding parameters are found to strongly affect both the macrostructure and microstructure of fusion welds and consequently their corresponding RVEs [7, 117]. Hence, the characteristics of the developed RVE, including the size and the substructure, have to be a function of welding parameters, otherwise the model cannot simulate the role of welding process parameters in forming a semisolid weld.

4.2.1.2 Creating a welding parameters-dependent RVE

In order to create a welding parameters-dependent RVE in which the size of the fusion zone and the grain size vary spatially based on welding parameters, a relation between the weld features and welding parameters must be first established. Therefore, a series of weld experiments were conducted in order to capture the required input parameters: depth of penetration, width of the weld, and length of the columnar zone. The details of these welding experiments are given in section 4.6. The obtained experimental results are utilized as input data since they link the macroscopic and microscopic characteristics of an aluminum 6061 weld to welding parameters, and therefore enable the solidification module to vary the features of the RVE (domain size, fusion zone dimensions, and also grain size) based on welding procedure. The X and Y dimensions for the RVE are set by the input welding parameters as follows: dimension in X=(depth of penetration from experimental input data (μm) + 200 μm), and dimension in Y=(half-width of the weld from experimental input data(μm) + 200 μm). The Z dimension, along the weld line, is set to 1000 μm . This value was chosen as a compromise between capturing the entire mushy zone and computational cost.

4.2.1.3 Mesh

The unstructured mesh representing the microstructure within the RVE was created from geometry generated using a Voronoi tessellation. The Voronoi tessellation is a technique of dividing spatial domains into numbers of subzones. A set of points (called seeds) is first specified within the domain and for each seed there will be a corresponding zone consisting of all points closer to that seed than to any other. The developed subzones are called Voronoi cells. Assuming the seed points and the Voronoi cells act as grain nuclei and grains respectively, this method can be utilized to create the unstructured mesh required to model

solidification using a granular method within simple microstructure composed of only equiaxed grains [11, 12, 46]. In order to extend the application of the Voronoi tessellation to the creation of complex welding microstructure composed of both columnar and equiaxed grains, an in-house C++ code was developed based on the Vor++ library [118]. This library allows for the creation of Voronoi diagrams within irregular-shaped domains. The in-house code first divides the simulation domain (RVE) into three separate primary regions: 1) base metal, 2) columnar zone, and 3) equiaxed zone at the center of the weld. Using the input data and also the process maps provided by the welding experiments, the code extracts the size and density of the grains in each region for various welding conditions, and consequently sets the number of seeds (grain nuclei) for each of the primary regions. Then, the code randomly distributes the three sets of grain nuclei through their corresponding regions to create three initial Voronoi diagrams representing the microstructure of the primary regions in 3D. In any of the three primary regions, if the average size of the developed grains does not match with the experimentally extracted size for that region, the code iteratively rearranges the nuclei in the region by using new random numbers until the Voronoi diagram with the proper grain size is obtained. By increasing the number of nuclei, the code takes more iterations to create the proper Voronoi diagram. Note that the code starts to diverge for more than 20,000 nuclei. Once the Voronoi diagrams of all three primary regions are finalized, the code assembles the primary regions and stitches their interfacial nodes to create a single unstructured mesh representing the microstructure of the weld.

Fig. 4.2a shows the final developed RVE for a weld fabricated with a welding speed of 3 mm/s and a welding amperage of 120 A. Three regions with different microstructure are clearly visible: base metal with equiaxed grains, columnar zone grains, and equiaxed grains at the center of the weld. Figs. 4.2b-4.2d show each of the individual regions. The base metal, Fig. 4.2b, is composed of polyhedral elements representing equiaxed grains and a fusion surface that follows a parabolic shape obtained from the experimental input data. The columnar zone, Fig. 4.2c, has elongated polyhedral grains. It is assumed that the epitaxial growth governs the formation of columnar grains [7] and thus the average diameter of the columnar grains is close to the size of the equiaxed grains within the base metal. The length of the columnar zone, D , and the size of the equiaxed grains at the centre of the weld, Fig. 4.2d, are given by the experimental data outlined in Section 4.6.

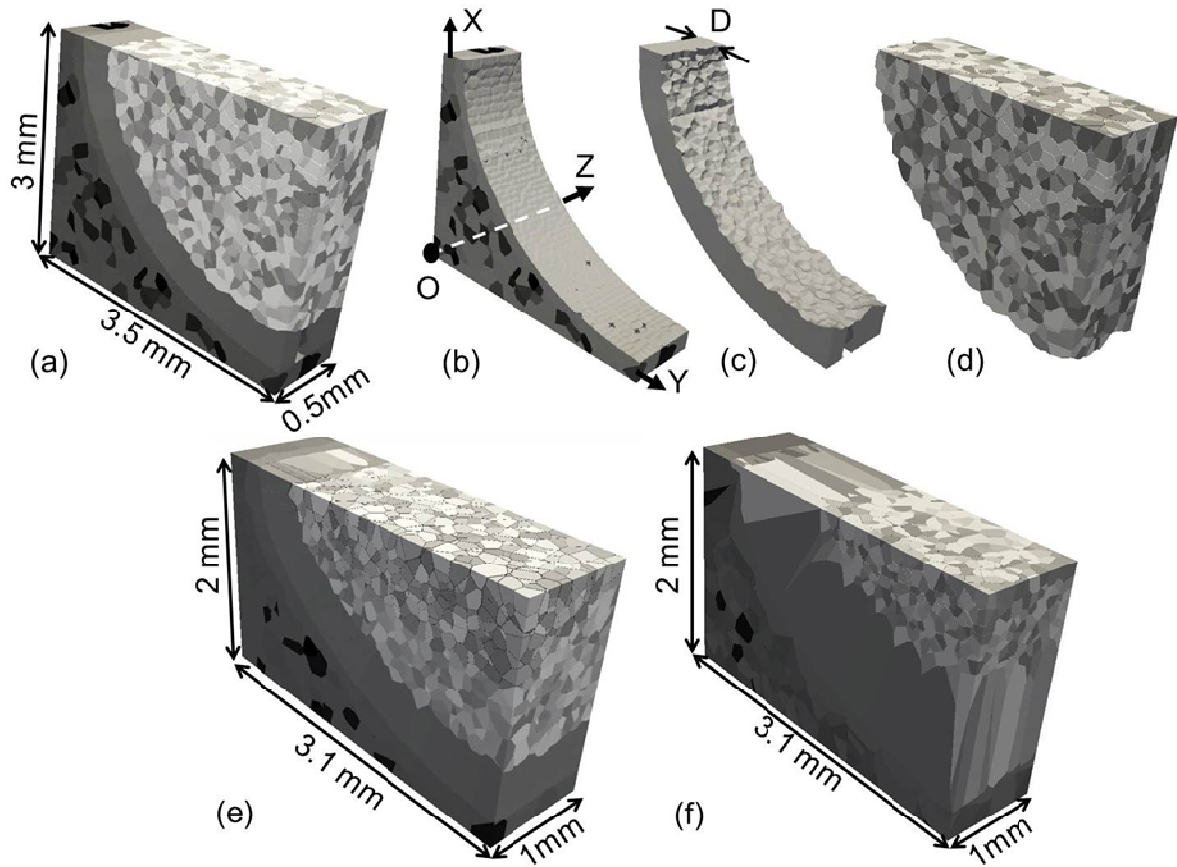


Fig. 4.2 (a) Developed geometry of the weld mushy zone for a welding speed of 3 mm/s and welding amperage of 120 A; (b) base metal grains; (c) columnar grains; (d) equiaxed grains at the center of the weld; (e) geometry of weld mushy zone fabricated with different conditions (welding speed of 5 mm/s, welding amperage of 140 A); (f) the same mushy zone as (e) but with longer columnar grains.

One of the unique features of the RVE is that the underlying constructed microstructure is a function of welding parameters. Fig. 4.2e depicts an RVE for a weld fabricated with welding speed of 5 mm/s and amperage of 140 A. In comparing Fig. 4.2a and Fig. 4.2e, it can be seen that different welding parameters change the size of the weld and also the microstructural features as the weld has shrunk in the latter case. Furthermore, the substructure can be easily modified to reflect the effect of grain manipulation techniques that are used to change the microstructure of the weld. Fig. 4.2f shows the RVE of a weld fabricated with the same welding parameters as of Fig. 4.2e but with a longer columnar zone associated with grain manipulation techniques in which columnar grains are able to grow longer. Physically, this

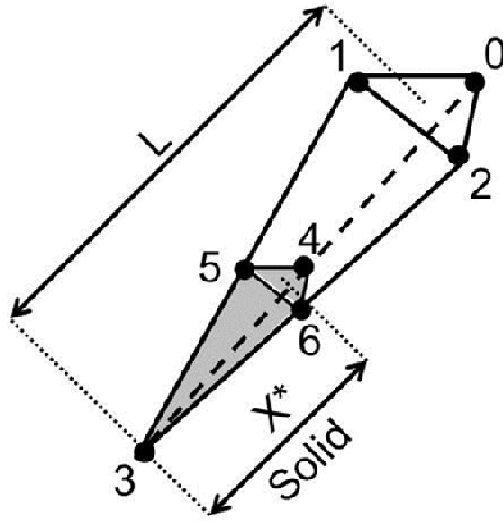


Fig. 4.3 Schematic of a primary tetrahedral element.

structure could have formed due to a lack of impurities, nucleants or turbulence within the weld pool [7].

After constructing complex 3D Voronoi diagrams such as the one shown in Fig. 4.2a, each Voronoi cell or grain is subdivided into polyhedral volume elements with the nucleation center as the summit and the Voronoi facet as the base [11]. These pyramids are divided further into tetrahedral elements in order to model solidification. Fig. 4.3 shows one of the tetrahedral elements. The nucleus of the grain (node 3) forms the apex of the element, and three other vertices (nodes 0, 1, and 2) form the base of a fully-solidified element. The solid/liquid interface is also shown (nodes 4, 5, and 6).

4.2.2 Thermal analysis

Simulation of solidification during a welding process requires knowledge of the thermal field since the solid fraction varies as a function of temperature. The thermal field, T , during welding as a function of spatial coordinates R_c (radial distance from the center of the weld) and D_c (distance from the center of the weld along the weld line) can be calculated from the well-known Rosenthal equation,

$$\frac{2\pi(T - T_o)KR_c}{Q} = \exp\left[\frac{-V(R_c - D_c)}{2\alpha}\right] \quad (4.1)$$

where T_o is the initial temperature of the workpiece, V is the travel speed of the torch, Q is the heat transferred from the torch to the metal, and K and α are the thermal conductivity and diffusivity of the base metal. Although the Rosenthal equation cannot yield precise temperatures above the liquidus, it provides a good prediction of the thermal fields in the mushy zone [7]. Since part of the nominal arc power, *i.e.* $Q_{nominal} = \text{welding voltage} \times \text{welding current}$, dissipates during welding, therefore $Q_{nominal} \neq Q$ and Q remains unknown. Hence, a reverse experimental technique is used to calculate Q . This experimental method is outlined in section 4.6.

In the present model, the temperature evolution at each node of the discretized mesh was calculated from the Rosenthal equation for a given set of welding parameters using a Matlab script. Within an element, the temperature at any position, T^p , was calculated via linear interpolation [119] of the four nodal temperatures, *i.e.*,

$$T^p = \sum_{i=0}^{i=3} \alpha_i T_i \quad (4.2)$$

where T_i are the nodal temperatures and α_i are the shape or interpolation functions. At an arbitrary point (p) in the natural coordinate system [119], the values of α_i are given by,

$$\alpha_i |_p = \frac{h_i^p}{h_i} = \frac{V_i^p}{V_T} \quad (4.3)$$

$$\sum_{i=0}^{i=3} \alpha_i |_p = 1 \quad (4.4)$$

where $\alpha_i |_p$ is the value of the i^{th} interpolation function at the point p , h_i^p represents the distance of p to the face opposite to the i^{th} node, h_i is the distance of the i^{th} node to the corresponding face, V_T is the total tetrahedral volume, and V_i^p represents the volume of the subtetrahedron spanned by the coordinates of the point p and the face opposite the i^{th} node. The definition of these variables is further presented in Fig. 4.4a and 4.4b, where $A_i^{s/l}$ represents the relative areas of the solid-liquid interface for each of the shape functions.

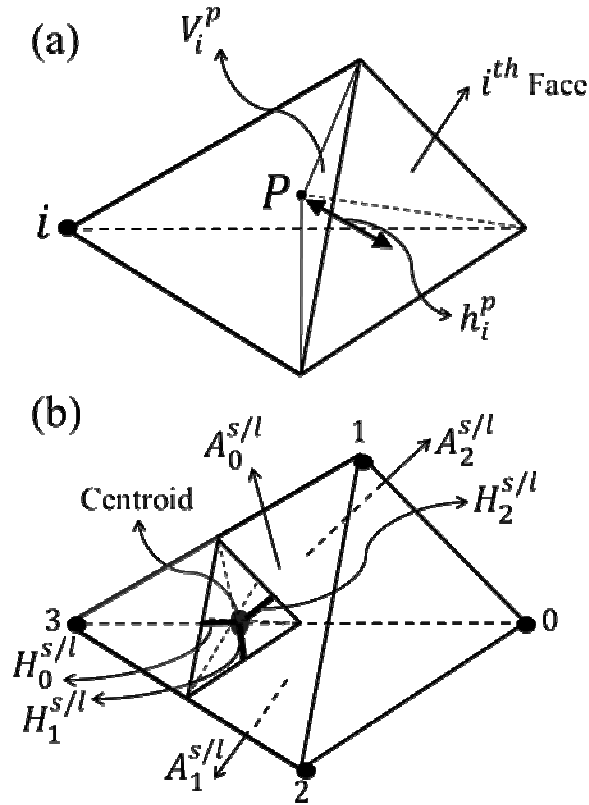


Fig. 4.4 (a) A reference tetrahedron element showing an arbitrary point (\mathbf{p}), the face opposite the \mathbf{i}^{th} node, subtetrahedron volume ($V_i^{\mathbf{p}}$) spanned by the point \mathbf{p} and the \mathbf{i}^{th} face, and also the distance of the point from the \mathbf{i}^{th} face ($h_i^{\mathbf{p}}$). (b) Shows the center of the triangular solidification front, and the geometrical characteristics (the area of the base ($A_i^{\mathbf{p}}$), and the height from the apex to the base ($H_i^{\mathbf{p}}$)) of the subtetrahedrons spanned by the coordinates of the centroid and the faces opposite the nodes 0, 1, and 2.

4.2.3 Solidification

The Voronoi tessellation represents the fully solidified microstructure. To model solidification within a tetrahedron, the solid/liquid interface is moved from the nucleus to the base facet, *i.e.* from node 3 in Fig. 4.3 towards nodes 0, 1, and 2 as a function of time. At the end of the solidification sequence, tetrahedrons from opposing grains come into contact with each other, and coalesce. In this study, the main focus is on the growth stage during solidification and only a simple thermal criterion is used to model nucleation. It is assumed

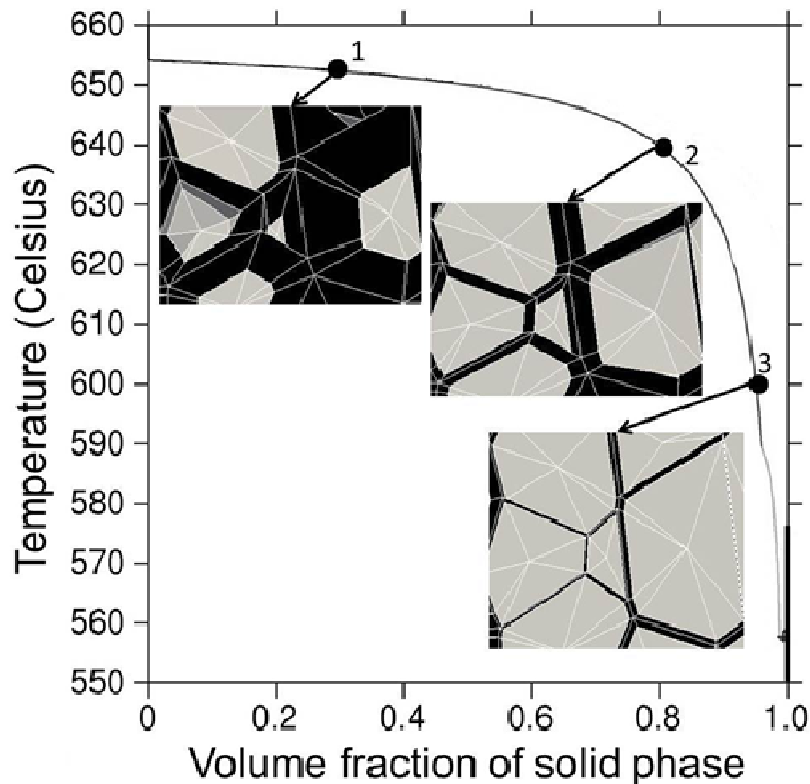


Fig. 4.5 The relation between the solid fraction and temperature for aluminum 6061 using a Scheil approximation within the Thermo-Calc software. Points 1, 2, and 3 and their corresponding images show the growth of the solid phase within the model during cooling.

that solidification starts in a tetrahedron element once the temperature at the nucleus of the element drops below the liquidus temperature.

Unlike previous granular-type solidification models [11, 12, 46], which used a 1-D microsegregation problem to model the interface evolution, Scheil-type solidification within individual elements is assumed in this study [7, 120-122]. This assumption avoids the need for developing a multi-component microsegregation model for the Al-Mg-Si system. In welding, the solidification rates are high and thus the Scheil assumption of complete diffusion in the liquid and no diffusion in the solid is appropriate. The Scheil equation links the temperature of an element to the fraction solid inside that element. The evolution in

fraction solid with temperature for AA6061 is plotted in Fig. 4.5. This curve was generated using the Thermo-Calc thermodynamics package assuming Scheil solidification conditions.

Once the fraction solid is known, the position of the solid/liquid interface within a tetrahedron can be calculated,

$$x^* = L\sqrt[3]{f_s} \quad (4.5)$$

where x^* represents the perpendicular distance from the apex of the tetrahedron to the solid/liquid interface, f_s , is the fraction solid at the given temperature as extracted from the Scheil model, and L is the perpendicular length of the element.

In order to apply the curve in Fig. 4.5 to model solidification during welding at the mesoscale, a single temperature must be assigned to each element at every time-step of the simulation. Due to the severe thermal gradients in welding, the four nodal temperatures calculated using Eq. (4.1) could be quite different, and consequently, an average temperature is inappropriate. Instead, it was assumed that the temperature at the center of the solid/liquid interface, $T_{s/l}$, controls the fraction solid within an element. Note that as the solid/liquid interface is small, the temperature gradient over the interface is negligible and thus, any point on the interface could have been chosen.

Since temperatures within any element are calculated via linear interpolation, the temperature at the center of the solid/liquid interface can be determined using Eq. (4.2). Based on the node numbering shown in Fig. 4.3, the value of the third shape function at this location is given by,

$$\alpha_3|_{s/l} = \frac{L - x^*}{L} = 1 - \frac{x^*}{L} . \quad (4.6)$$

Note that the node 3 corresponds to the nucleus of the solidifying element. Due to symmetry, the other three shape functions are equal, as they all have the same base area, $A_0^{s/l} = A_1^{s/l} = A_2^{s/l}$, and the same height from their base to their apex, $H_0^{s/l} = H_1^{s/l} = H_2^{s/l}$. Consequently,

$$\alpha_0|_{s/l} = \alpha_1|_{s/l} = \alpha_2|_{s/l} . \quad (4.7)$$

The combination of Eqs. (4.4), (4.6), and (4.7) give,

$$\alpha_0 |_{s/l} = \alpha_1 |_{s/l} = \alpha_2 |_{s/l} = \frac{x^*}{3L} . \quad (4.8)$$

By substituting Eqs. (4.6) and (4.8) into Eq. (4.2), the temperature at the center of the solid/liquid interface is given by,

$$T_{s/l} = \left(1 - \frac{x^*}{L}\right) T_3 + \left(\frac{x^*}{L}\right) T_{base} \quad (4.9)$$

where $T_{base} = (T_0 + T_1 + T_2)/3$ corresponds to the arithmetic average of the nodal temperatures at the base of the tetrahedron. Finally, Eqs. (4.5) and (4.9) can be combined to yield a master equation controlling the movement of the solid/liquid interface,

$$T_{s/l} = \left(1 - \sqrt[3]{f_s(T_{s/l})}\right) T_3 + \left(\sqrt[3]{f_s(T_{s/l})}\right) T_{base} \quad (4.10)$$

where $f_s(T_{s/l})$ is the fraction solid in Fig. 4.4 assuming a temperature at the solid/liquid interface.

The choice of using the solid/liquid interface as the controlling temperature for determining the fraction solid based on Fig. 4.5, in combination with the fact that there is a strong temperature gradient within an element based on Eq. (4.2) necessitates that Eq. (4.10) be solved via an iterative solution. An initial analysis of Eq. (4.10) shows that this equation is well behaved and has a unique solution. Therefore, the system equations were numerically solved using the Newton-Raphson method for each element to obtain $T_{s/l}$ at each time step. Then, the converged values were applied to Eq. (4.5) to extract the positions of the interface with time, and therefore, to track the growth of the solid phase within the RVE. Three different images have been inset into Fig. 4.5 in order to show the evolution of the solid/liquid interface and therefore the simulation of the growth of the solid phase with temperature. In these images, the dark (light) areas represent the liquid (solid) phases.

4.2.4 Coalescence

Coalescence during solidification corresponds to the point at which two neighbouring solid grains come into contact with each other and coalesce or bridge [11, 12]. This occurs near the end of solidification; two grains may be in mechanical contact but have not yet fused together, *i.e.* coalesced, due to thermodynamic considerations. Coalescence plays a large role

in defect formation since undercoolings on the order of 75°C below the equilibrium liquidus can be required [46], extending the temperature range where continuous liquid films exist prior to final solidification. The present model utilizes the thermodynamic criterion proposed by Mathier to reflect the nonuniformity of grain coalescence during solidification [49]. Based on this criterion, it is assumed that the neighbour grains with crystallographic misorientations of 15 deg. or less are attractive couples that coalesce immediately as their solidification fronts meet each other. On the other hand, once the misorientations exceed 15 deg., the grains are assumed to be repulsive couples that do not coalesce until a required undercooling is reached. The numerical implementation of this coalescence criterion can be found in Reference [12]. Note that since the amount of the eutectic phase in the aluminum 6061 is negligible [3], the formation of this phase in the solidification module and its role in the coalescence phenomenon are not considered in this model.

4.3 Deformation module²

The output of the solidification module presented in Section 4.2 consists of an assembly of solid grains and a network of micro liquid channels at the grain boundaries. The Deformation Module uses this geometry as the numerical mesh to characterize deformation within the weld mushy zone due to both self-induced strains and externally applied (augmented) strains.

The geometry of a single micro liquid channel is shown in Fig. 4.6a, along with the applied local coordinate system. The origin is fixed on one of the channel walls and the local z axis is orthogonal. The corresponding network of micro liquid channels, obtained by assembling the individual channels, is shown in Fig. 4.6b. As solidification evolves, the channel widths decrease until the grains coalesce. The solidification module outputs the channel width and velocity of the channel walls as a function of time during welding. The deformation module utilizes the outputs of the solidification module to analyze the deformation characteristics of the micro liquid channels within the weld mushy zone.

² Part of this section is published in: 1) Zareie Rajani, H. R., Phillion, A. B., "A Multi-scale Thermomechanical-Solidification Model to Simulate the Transient Force Field Deforming an Aluminum 6061 Semisolid Weld", *Metallurgical and Materials Transactions B* 46.4 (2015): 1942-1950, and 2) Zareie Rajani, H. R., Phillion, A. B., "3D multi-scale modelling of deformation within the weld mushy zone", *Materials & Design* 94 (2016): 536-545.

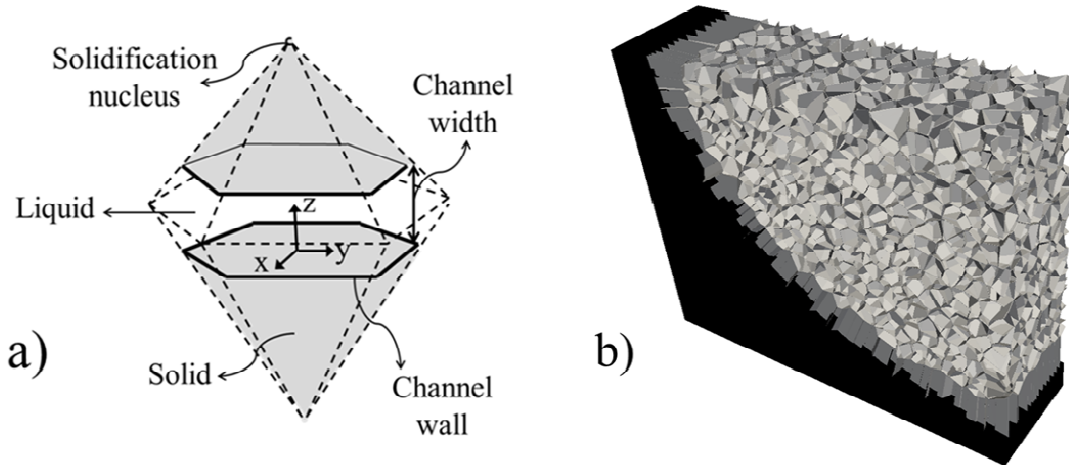


Fig. 4.6 (a) The geometry of a single micro liquid channel sandwiched between two parallel solidification fronts; (b) the reconstructed network of micro liquid channels for the mushy zone of the weld shown in Fig. 4.2a.

Assuming that the walls of the micro liquid channels within the RVE remain parallel during welding [4], the deformation rate vector $\overrightarrow{\delta}^i$ of a micro liquid channel, where i is a counter representing the channel number, can be decomposed into two components. The first is the normal deformation rate along the local z direction ($\overrightarrow{\delta}_z^i$), representing the separation rate of the channel walls. The second is the shear deformation rate ($\overrightarrow{\delta}_{xy}^i$), characterizing the relative displacement of the walls parallel to the local xy surface. According to previous micro-scale models of hot cracking [99, 100], it is only the separation rate of the channel walls that affects the formation of hot cracks within the micro liquid channel. Thus, the shear component of the deformation rate vector can be ignored.

The normal deformation rate (δ_z^i) can be further divided into internal and external components based on the source of deformation,

$$\delta_z^i = \delta_{z,int}^i + \delta_{z,ext}^i \quad (4.11)$$

where $\delta_{z,int}^i$ corresponds to the internal normal deformation rate caused by solidification shrinkage, and $\delta_{z,ext}^i$ is the external normal deformation rate induced by the external sources that act on the mushy zone and distort the entire network of micro liquid channels.

4.3.1 Internal normal deformation rate

It has been already shown that the recession rate of a solidification front due to solidification shrinkage is given by βv^* [12], where v^* is the velocity of the solidification front, $\beta = (\rho_s/\rho_l - 1)$ is the shrinkage factor, and ρ_l and ρ_s are the densities of the liquid and solid. As a result, the separation rate of the walls of any individual channel along the local z direction and consequently the internal normal deformation rate can be obtained by,

$$\dot{\delta}_{z,int}^i = \beta(v_1^* + v_2^*) \quad (4.12)$$

where v_1^* and v_2^* are the velocities of the two channel walls, given by the solidification module, that make up an individual micro liquid channel. The velocity of a channel wall is directly proportional to $\frac{dT}{dt} \frac{\partial f_s}{\partial T}$, *i.e.* the product of the cooling rate and the solidification rate. As shown in Fig. 4.5, the solidification rate for AA 6061 and consequently the velocity of the channel walls becomes significantly reduced as the temperature decreases and the solid fraction increases [100, 116]. The present model utilizes Eq. (4.12) to determine the evolution of the internal normal deformation rate of every single micro liquid channel within the weld pool at a given time. The values of v_1^* and v_2^* are taken from the output of the solidification module.

4.3.2 External normal deformation rate

Unlike the internal normal deformation rate, the external normal deformation rate applied to individual micro liquid channels cannot be directly determined through solidification models. Instead, it is quantified using a two-stage process. First, the average strain rate of the entire weld mushy zone, denoted global strain rate, $\dot{\epsilon}$, is determined and then translated to a global deformation rate, $\dot{\delta}$. Second, the global deformation rate is partitioned amongst each micro liquid channel to yield $\dot{\delta}_{z,ext}^i$. Note that the global deformation/strain rate refers to only the lateral tensile component (Y -dir in Fig. 4.1), *i.e.* the component perpendicular to the weld line since it is tensile deformation in this direction that governs hot cracking in welding [7, 115].

4.3.2.1 Calculation of the global strain rate

As the mushy zone solidifies, the base metal thermo-mechanically reacts to the thermal shrinkage and solidification shrinkage of the weld, and also temperature variations in the heat affected zone, evolving a transient thermo-mechanical force field that distorts the mushy zone [79, 80, 85]. Concurrently, the mushy zone can deform as a result of the restraining (augmented) forces applied to the base metal [52]. Hence, the global strain rate consists of,

$$\dot{\epsilon} = \dot{\epsilon}_{th} + \dot{\epsilon}_{re} \quad (4.13)$$

where $\dot{\epsilon}_{th}$ and $\dot{\epsilon}_{re}$ are the strain rates induced by the thermo-mechanical forces and the restraining forces. While the restraining strain can be directly controlled and measured based on the restraining forces explicitly applied to the base metal [52], the thermo-mechanical component of the global strain rate has a complex nature and cannot be simply controlled and measured.

There are two common approaches for treating the thermo-mechanical component of the global strain rate. First, $\dot{\epsilon}_{th}$ can be neglected assuming that $\dot{\epsilon}_{re}$ is significantly large and therefore dominates the deformation of the mushy zone. This assumption suits hot crack sensitivity tests such as V-restraint in which high external strain rates are applied to the base metal. However, this approach cannot be applied to self-restrained welding conditions where $\dot{\epsilon}_{re} = 0$. The self-restrained welding condition is defined as a welding condition in which every point on the edges of the workpiece is tightly clamped, and therefore the edges of the workpiece are fixed in all directions. Alternatively, $\dot{\epsilon}_{th}$ can be experimentally measured [115, 123]. However, the extensometer is usually located across the weld root in order to avoid a collision with the welding torch, which can cause significant measuring errors. In this research, a two-step numerical approach is proposed to simulate the thermo-mechanical component of the global strain rate. In the first step, the lateral thermo-mechanical stresses acting on the weld mushy zone are modeled. Then, assuming the behaviour of semisolid AA6061 is governed by a well-defined constitutive equation, the calculated stresses are translated into a thermo-mechanical strain rate. The details of each step are discussed below.

4.3.2.1.1 Simulation of the transient thermo-mechanical stress field

The transient thermo-mechanical force field acting on the weld mushy zone ($\vec{f}_{\partial\Omega_{\text{fusion|semisolid weld}}}$) results from a mechanical interaction between the semisolid weld and the base metal in response to the non-uniform thermal expansion and contraction of both the weld pool and base metal during welding. Utilizing Newton's third law of motion, the thermo-mechanical forces acting on the weld mushy zone are equal and opposite to the reaction forces that act on the base metal at the fusion surface ($\vec{f}_{\partial\Omega_{\text{fusion|base metal}}}^{\text{reaction}}$),

$$\vec{f}_{\partial\Omega_{\text{fusion|semisolid weld}}} = -\vec{f}_{\partial\Omega_{\text{fusion|base metal}}}^{\text{reaction}} \quad (4.14)$$

For this reason, the deformation module uses the finite element method to analyze the thermo-mechanical behaviour of the base metal adjacent to the mushy zone to determine $\vec{f}_{\partial\Omega_{\text{fusion|base metal}}}^{\text{reaction}}$ and consequently $\vec{f}_{\partial\Omega_{\text{fusion|semisolid weld}}}$. Specifically, as discussed later, the deformation module is linked with the Abaqus commercial finite element software to analyze the deformation of the base metal and determine the reaction force field.

The 3D simulation domain (Ω) for the thermo-mechanical analysis consists of the base metal itself with a small portion removed representing the semisolid weld line. Due to symmetry, only one-half of the weld, and only one side of the base metal are included in the domain. As illustrated in Fig. 4.7a, the base metal is separated from its surroundings via a boundary ($\partial\Omega$) composed of seven different surfaces: a parabolic fusion surface ($\partial\Omega_{\text{fusion|base metal}}$) representing the contact between the base metal and the weld line; a symmetry surface ($\partial\Omega_{\text{symmetry}}$) lying on the symmetry plane of the weld below the fusion surface; the back surface ($\partial\Omega_{\text{back}}$) that is assumed to be either free or constrained; and four free surfaces ($\partial\Omega_{\text{free}}$) that are not in contact with anything but the air. Based on the defined Cartesian coordinate system, the depth and width of the plate respectively lie along the X and Y directions, and the Z direction follows the line of welding. The width and thickness of the base metal are assumed to be 50 mm and 3 mm, and the simulated weld length is set at 20 mm. The shape of the material removed representing the weld pool is given by the input welding parameters [7]. As shown in Fig. 4.7b, the choice of welding parameter can significantly influence the geometry of the fusion surface. Therefore, a Python script was

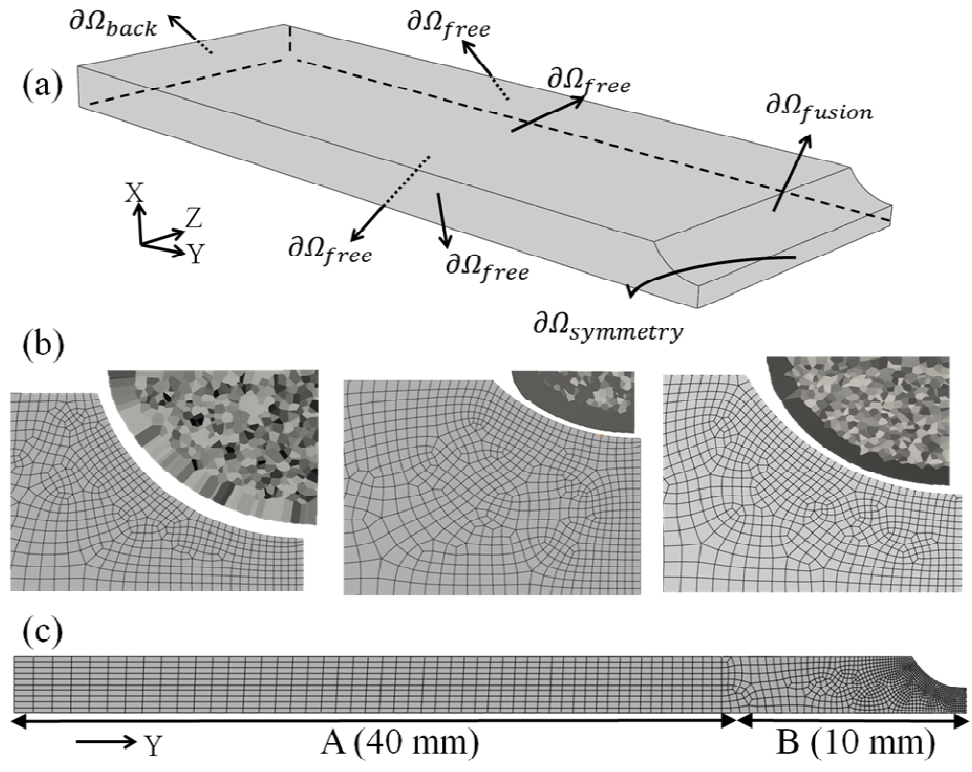


Fig. 4.7 (a) The boundaries of the base metal; (b) Variation in the size of the weld and consequently the shape and size of the base metal geometry due to using different welding parameters; (c) The discretized base metal in 2D.

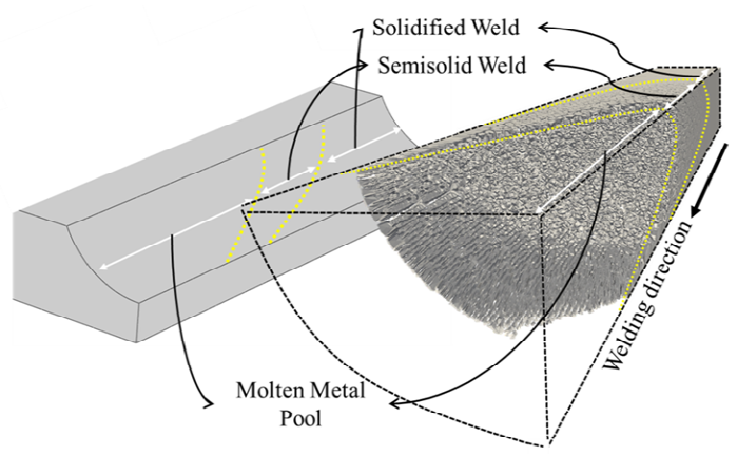


Fig. 4.8 Various transient regions on the fusion surface separating the base metal from the weld line.

developed within Abaqus to automatically generate a simulation domain based on the output of the solidification module.

Once the domain is defined, it is then discretized using a mesh composed of 8-node linear elements that vary in size depending on their position relative to the fusion surface. Fig. 4.7c depicts a 2D cross-section of the discretized domain. The area far from the weld surface, labeled A, contains elements with a gradient in average size from 1000 to 300 μm . The refined area near the weld surface, labeled B, contains elements varying in size from 300 to 100 μm . The need for a 3D simulation domain is demonstrated in Fig. 4.8, which shows a portion of the base metal and the fusion zone. As can be seen, the fusion zone is composed of three different areas along the weld line: the molten metal pool (represented by empty space); the semisolid weld forming right behind the molten metal; and finally the fully solidified weld. As the process is transient, and the welding torch is moving, each element on the fusion surface will first be in contact with the molten aluminum, then the semisolid weld, and finally the fully solidified metal. Note that the solid region in front of the molten metal pool is ignored as the model focuses on only the mechanical interaction between the fusion zone and the base metal.

The boundary conditions applied to the different surfaces are as follows:

- (1) $\partial\Omega_{\text{free}}$ – As the free surfaces (four) are only in contact with air, a homogeneous boundary condition, $\vec{f}|_{\partial\Omega_{\text{free}}} = 0$, is defined.
- (2) $\partial\Omega_{\text{symmetry}}$ – This surface is constrained in the Y direction due to symmetry, and also in X and Z directions since the weld line is normally clamped to prevent misalignment defects during welding.
- (3) $\partial\Omega_{\text{back}}$ – The back surface can be subject to different displacement boundary conditions, $\vec{U}|_{\partial\Omega_{\text{back}}} = \vec{U}_o$, where \vec{U} is the material flow, to model various welding constraints including clamped ($\vec{U}_o = 0$), and tension/compression ($\vec{U}_o \neq 0$). It is also possible to assume that the back surface of the base metal is not clamped during welding by setting a homogenous boundary condition, $\vec{f}|_{\partial\Omega_{\text{back}}} = 0$.

- (4) $\partial\Omega_{\text{fusion|base metal}}$ – The boundary condition applied to the fusion surface of the base metal is complex since the displacement field, $\vec{U}|_{\partial\Omega_{\text{fusion}}} = \vec{D}_{(\vec{x},t)}$ is imposed by the shrinkage associated with solidification rather than a mechanical tool such as a clamp. Due to the solidification conditions occurring during welding, the resulting shrinkage-related displacements are non-uniform across this interface and vary with time.

In order to determine the boundary condition applied to the fusion surface of the base metal, *i.e.* $\partial\Omega_{\text{fusion|base metal}}$, the deformation module uses the outputs of the solidification module to calculate $\vec{D}_{(\vec{x},t)}$. Specifically, considering the Cartesian coordinate system in Fig. 4.7, the total solidification shrinkage in the weld pool can be described as a deformation in the three primary directions X , Y , and Z . In the X and Z directions, it is assumed that the shrinkage is fully accommodated by displacement of a free end. In the case of X , the free end is the air/weld pool interface. In the case of Z , the free end is the fully liquid molten metal just below the weld torch. Such an assumption is justified by the observation of a concave surface seen at the top of a weld when filler metal is not used to compensate for shrinkage [7]. On the other hand, the fusion surface and the rigid symmetry plane at the centre of the weld line confine material flow in the Y direction. This confinement results in the application of a force on the fusion surface to accommodate the shrinkage component in Y direction, *i.e.* the lateral solidification contraction.

Based on conservation of mass, the lateral solidification contraction Y_{Sh} for a confined domain within the semisolid weld can be expressed as,

$$Y_{\text{Sh}} = Y_0 \sqrt[3]{f_s} (1 - \alpha_s) \quad (4.15)$$

where $\alpha_s = \sqrt[3]{\rho_l/\rho_s}$ is the linear shrinkage coefficient, ρ_l and ρ_s are the liquid and solid densities respectively, and Y_0 and f_s denote the lateral length and volumetric solid fraction. For a small solidification increment, Eq. (4.15) can be rewritten in differential form,

$$dY_{\text{Sh}} = \frac{1}{3} Y_0 (1 - \alpha_s) f_s^{-\frac{2}{3}} df_s . \quad (4.16)$$

Integration of Eq. (4.16) yields the gradual, accumulation of the lateral solidification contraction within the confined space as a function of solid fraction. Since the semisolid is not able to transfer stress before a continuous solid bridge forms across the confined domain,

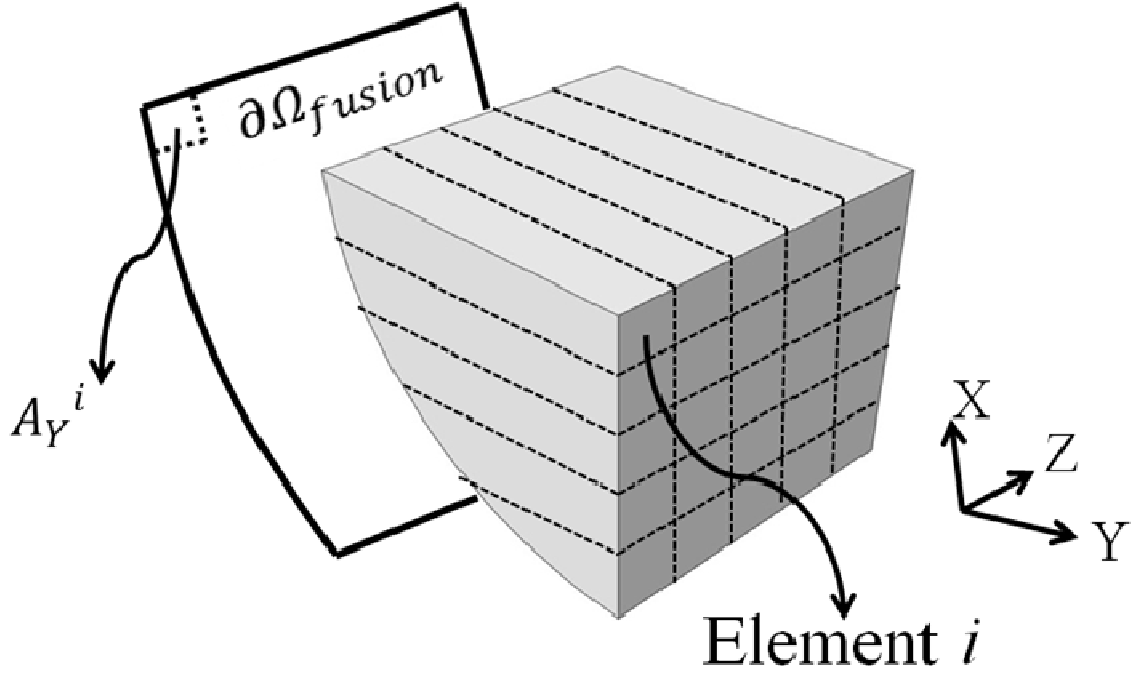


Fig. 4.9 The bar elements used to obtain the local solid fraction within the semisolid weld.

i.e. the percolation point or mechanical coalescence, the integration domain is limited to values of solid fraction at which the semisolid is percolated, *i.e.*,

$$Y_{sh}|_t = \int_{f_{s|p}}^{f_{s|t}} \frac{1}{3} Y_0 (1 - \alpha_s) f_s^{-\frac{2}{3}} df_s = Y_0 (1 - \alpha_s) \left(\sqrt[3]{f_{s|t}} - \sqrt[3]{f_{s|p}} \right). \quad (4.17)$$

In Eq. (4.17), $Y_{sh}|_t$ represents the evolution in linear solidification contraction with time, $f_{s|t}$ denotes the average solid fraction of the confined space as a function of time, and $f_{s|p}$ represents the average solid fraction at the percolation point, assumed to occur at a value of $f_s = 0.95$.

The confined elements used in this study are shown in Fig. 4.9. These elements, given the name bar elements, lie along the Y direction connecting the weld center to the fusion surface. The ensemble of the bar elements and their corresponding displacement functions ($Y_{sh}|_t^i$), where the index i represents an individual bar element, yields the Dirichlet boundary condition acting on the fusion surface,

$$\vec{U}|_{\partial\Omega_{fusion|base\ metal}} = \vec{D}_{(\vec{x},t)} = \begin{cases} D_Y|_t = Y_{sh}|_t^i \\ D_X|_t = D_Z|_t = 0 \end{cases}, \quad \vec{x} \in A_Y^i \quad (4.18)$$

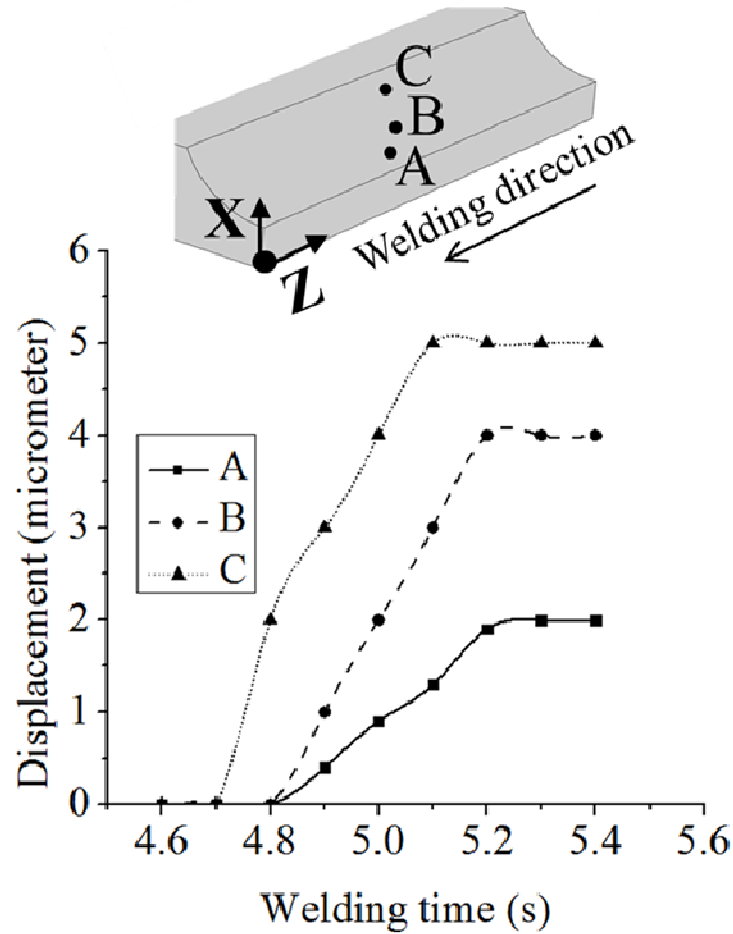


Fig. 4.10 The shrinkage displacement values, $\vec{D}_{(\vec{x},t)}$, at three different points on the fusion surface of a weld fabricated using a welding current of 120 A and a welding speed of 3 mm/s.

where the term A_{γ}^i refers to the projection of bar element i onto the portion of the fusion surface containing the given point in $\vec{D}_{(\vec{x},t)}$. In order to obtain $f_s|_t^i$, the deformation module is linked to the solidification module. The solidification module provides the average solid fraction of the bar elements during welding, and therefore, enables the model to define a time and position dependent boundary condition on the fusion surface of the base metal. Note that the semisolid weld is assumed to remain intact during solidification.

The shrinkage displacement values, $\vec{D}_{(\vec{x},t)}$, at three different points on the fusion surface of a weld fabricated using a welding current of 120 A and a welding speed of 3 mm/s are plotted as a function of welding time in Fig. 4.10. In this figure, the welding time of zero represents

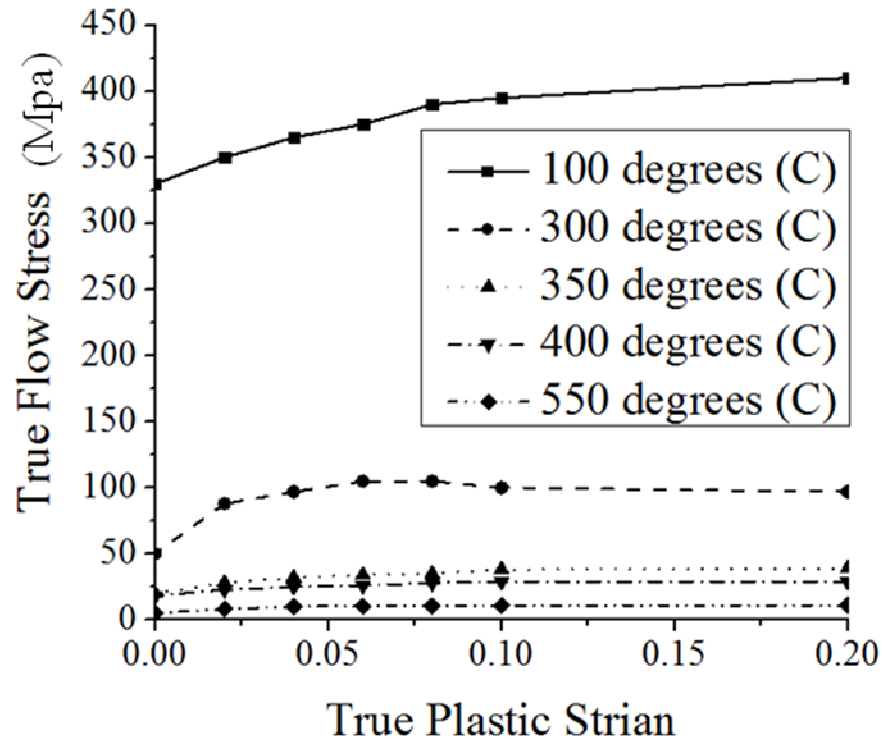


Fig. 4.11 The temperature-dependent flow stresses for AA6061 [124, 125].

the beginning of solidification in the domain. As the three points are at different locations on the fusion surface, they start to displace at different times. As can be seen, each also accumulates different amounts of shrinkage displacement since the percolation through the semisolid weld does not occur uniformly, and the size of the bar elements is different at each location. The bar element C is the largest, and thus, it experiences the largest displacement.

The mechanical properties provided to the Deformation Module follow an elastic-plastic constitutive law for AA6061 [124, 125] with work hardening and temperature-dependency, obeying the von Mises' plasticity criterion, *i.e.* $\sigma_o|_T = F(\epsilon_{eq}^{pl})|_T$, where $\sigma_o|_T$ denotes a temperature-dependent flow stress and ϵ_{eq}^{pl} is the equivalent plastic strain. The corresponding stress/strain curves are shown in Fig. 4.11. Since welding parameters do not significantly change the strain rate of the base metal [126] and also due to the relatively low sensitivity of AA6061 to strain rate [124, 125, 127], strain rate dependency is not included. Note that

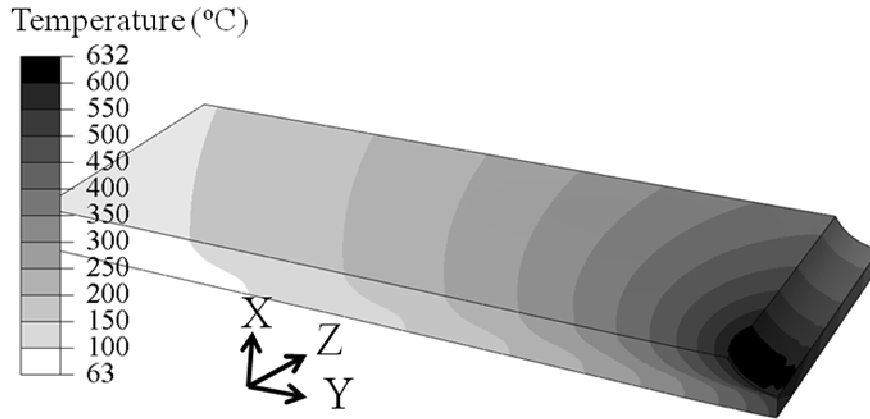


Fig. 4.12 The temperature field within the base metal for a weld fabricated with a speed of 3 mm/s and a current of 120 A.

Abaqus uses linear interpolation to calculate constitutive properties at temperatures other than the ones given in Fig. 4.11.

Simulation of the response of the base metal to a welding procedure requires knowledge of the thermal fields in order to include the effects of thermal expansion and contraction during the welding process, and to properly account for the variation in flow stress with temperature resulting from the thermal gradient. In addition, the temperature field is required since the material properties are defined as a function of temperature. Similar to the solidification module, the Rosenthal equation is used in the deformation module to determine the temperature field. Fig. 4.12 depicts the obtained temperature field within the base metal for a weld fabricated with a speed of 3 mm/s and a current of 120 A. The image shows the point when the fusion zone is molten only at the front edge of the weld pool. The remainder of the fusion surface sees temperatures in the semisolid regime. Utilizing the obtained temperature fields, this module generates a subroutine UTEMP through which the time-dependent temperature distribution during welding is assigned.

Finally, the deformation module performs a static mechanical analysis on the base metal using the Abaqus finite element code in order to obtain the reaction forces acting on the fusion surface, $\vec{f}_{\partial\Omega_{\text{fusion}}|\text{base metal}}^{\text{reaction}}$. Since the amount of plastic strain within the base metal is

small [7], the mechanical model is sequentially coupled to the thermal model instead of solving a fully coupled thermomechanical problem. Eq. (4.14) is then applied to extract the transient force field that deforms the semisolid weld, *i.e.* $\vec{f}_{\partial\Omega_{\text{fusion}}|\text{semisolid weld}}$.

Since the global strain rate and its thermo-mechanical component are assumed to have only lateral characteristics, the tensile components of $\vec{f}_{\partial\Omega_{\text{fusion}}|\text{semisolid weld}}$ in Y that apply on bar elements with $f_s > f_s|_p$ are averaged and then divided by the percolated area of the fusion surface to finally obtain the average time-dependent tensile stress acting on the semisolid weld.

4.3.2.1.2 Translation of the thermo-mechanical stress into the strain rate

In order close the loop, and determine the thermo-mechanical strain rates, $\dot{\varepsilon}_{th}$, acting on the semi-solid weld, the average lateral stress acting on the fusion surface, σ , is coupled with a visco-plastic constitutive equation for semisolid AA 6061 [128]. The constitutive equation for semisolid AA 6061 is of the form,

$$\sigma = e^{(a-bT)}(\varepsilon + \varepsilon_0)^n(\dot{\varepsilon} + \dot{\varepsilon}_0)^m(1 - \alpha_c f_l) \quad (4.19)$$

where a , b , n , m , $\dot{\varepsilon}_0$, ε_0 , and α_c are empirical constants [128], T represents the average temperature of the mushy zone in Kelvin and f_l is the average liquid fraction of the mushy zone. By rearranging Eq. (4.19), one can express the thermo-mechanical strains at t_2 and t_1 , *i.e.* ε_2 and ε_1 , as a function of their corresponding thermo-mechanical stress values, *i.e.* σ_2 and σ_1 ,

$$\varepsilon_2 = \left[\frac{\sigma_2}{e^{(a-bT)}(\dot{\varepsilon}_2 + \dot{\varepsilon}_0)^m(1 - \alpha_c f_l)} \right]^{1/n} - \varepsilon_0 \quad (4.20)$$

$$\varepsilon_1 = \left[\frac{\sigma_1}{e^{(a-bT)}(\dot{\varepsilon}_1 + \dot{\varepsilon}_0)^m(1 - \alpha_c f_l)} \right]^{1/n} - \varepsilon_0 \quad (4.21)$$

Further, $\dot{\varepsilon}_{th}$ can be given by the difference in strain between one time increment and the next,

$$\dot{\varepsilon}_{th} = \frac{\varepsilon_2 - \varepsilon_1}{t_2 - t_1} \quad (4.22)$$

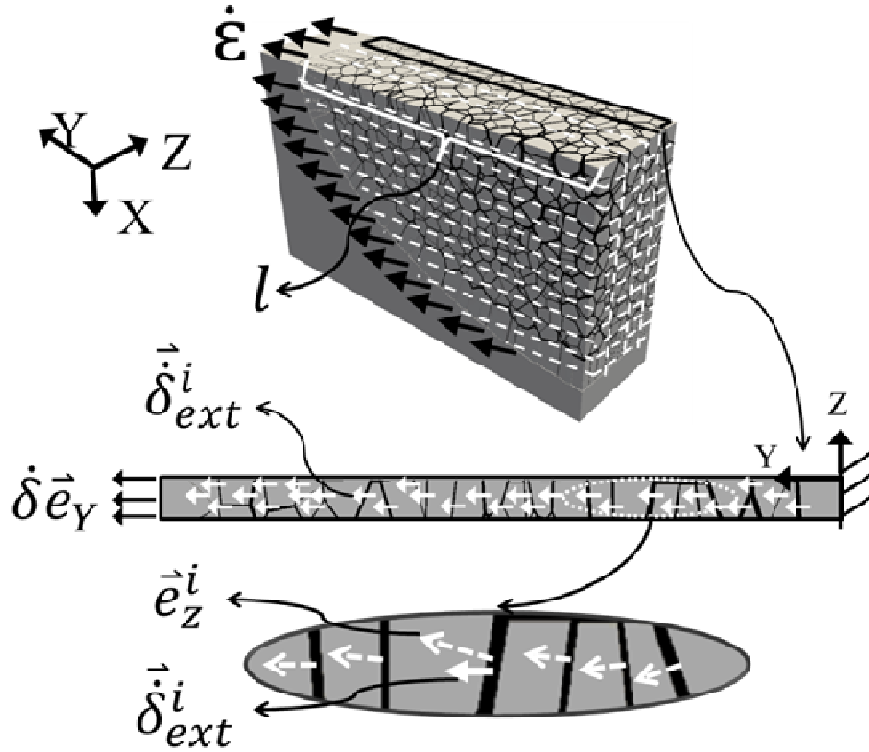


Fig. 4.13 The decomposition of the global deformation rate vector into external normal deformation rate vectors.

Assuming a small time interval, $\Delta t = t_2 - t_1$, such that $\frac{\partial \dot{\epsilon}_{th}}{\partial t} |_{t \in \Delta t} \approx 0$ and that liquid fraction remains unchanged, $\dot{\epsilon}_2 = \dot{\epsilon}_1 = \dot{\epsilon}_{th}$. Substituting Eqs. (4.20) and (4.21) into Eq. (4.22) leads to,

$$\dot{\epsilon}_{th} = A(\dot{\epsilon}_{th} + \dot{\epsilon}_o)^{-m/n}, \quad A = (1/\Delta t) \left[\frac{1}{e^{(a-bT)(1-\alpha f_l)}} \right]^{1/n} (\sigma_2^{1/n} - \sigma_1^{1/n}). \quad (4.23)$$

Eq. (4.23), being implicit, is solved at different time values using the Newton-Raphson method. The $\dot{\epsilon}_{th}$ value calculated above is then added to restraining strains $\dot{\epsilon}_{re}$ to yield the variation in the global strain rate $\dot{\epsilon}$ with time. Finally, $\dot{\epsilon}$ is translated into the global deformation rate as,

$$\dot{\delta} = l \dot{\epsilon} \quad (4.24)$$

where l is the initial lateral length of the mushy zone. Note that the weld mushy zone has a variable lateral length along the global X direction due to the shape of the weld pool and therefore Eq. (4.24) cannot be applied directly to the mushy zone as a single body. Instead, the weld mushy zone is discretized into lateral bar elements as shown in Fig. 4.13 that lie along the global Y direction. Each bar element has a Known length and cross section area given by the grain size. Note that these bar elements are different from the ones used to calculate solidification contraction (Fig. 4.9). In those elements, the bar cross sectional area is independent of the grain size.

4.3.2.2 Partitioning to individual micro liquid channels

After calculating the global deformation rate acting on the weld mushy zone, the deformation module distributes this global value among the micro liquid channels. Specifically, a partitioning technique proposed by Coniglio and Cross [115, 123] is utilized to distribute the global deformation rate of a bar element among the micro liquid channels within it. This method treats the mushy zone as a composite material composed of solid and liquid phases and decomposes the global deformation rate vector into a series of local deformation rate vectors. The local vectors have the same direction as the global vector and are applied to every fully solid grain and every micro liquid channel between partially solidified grains. Therefore,

$$\dot{\delta} = \sum_{j=1}^{j=\dot{N}} \vec{\delta}_{Grain}^j + \sum_{i=1}^{i=N} \vec{\delta}_{ext}^i \quad (4.25)$$

where $\vec{\delta}_{Grain}^j$ are the local deformation rate vectors of the solid grains, $\vec{\delta}_{ext}^i$ are the local deformation rate vectors of the micro liquid channels induced by the external sources, and \dot{N} and N are the number of solid grains and micro liquid channels. Since the liquid phase is significantly weaker than the solid phase, the role of the solid grains in partitioning the global deformation rate can be neglected. Therefore, Eq. (4.25) can be reduced to,

$$\vec{\delta}_{ext}^i = \frac{\dot{\delta}}{N} \quad (4.26)$$

assuming that the micro liquid channels equally contribute to the global deformation rate. Fig. 4.13 depicts the visual interpretation of Eq. (4.26) for a bar element in a 2-D view.

This method does not yet consider the dendrite coherency phenomenon at high solid fractions [115, 123]. Dendrite coherency corresponds to the moment when the secondary dendrite arms on the walls adjoining grains merge and form a solid bridge across the micro liquid channel [129]. Note that the dendrite coherency phenomenon is different than the coalescence phenomenon simulated in the solidification module. The coalescence phenomenon does not account for the dendritic feature of grains. Coherency corresponds to the point when the dendrites first become in mechanical contact whereas coalescence corresponds to the point where, because of thermodynamics, the last liquid between the grains vanishes. From a mechanical point of view, the walls of a bridged channel are interlocked and cannot separate unless the bridging dendrite arms break apart. Therefore, the bridged channels behave similar to solid grains [45, 100] and their contribution to the deformation of the mushy zone is negligible. With the same reasoning, an isolated cluster of micro liquid channels that is fully surrounded by the bridged channels and not connected to the base metal or the surface of the weld do not contribute to the distribution of the global deformation rate either. In order for this partitioning technique to reflect the effect of the dendrite coherency, Eq. (4.26) is modified as follows,

$$\vec{\delta}_{ext}^i = \eta \frac{\delta}{N_u}, \quad \begin{cases} \eta = 0 & \text{if } f_s \geq f_s^{coh} \\ \eta = 1 & \text{if } f_s < f_s^{coh} \end{cases} \quad (4.27)$$

where N_u is the number of the unbridged channels of a bar element that do not belong to an isolated cluster, f_s represents the solid fraction in the vicinity of the micro liquid channel i , and f_s^{coh} represents the solid fraction at which the dendrite coherency occurs, assumed to be 0.95.

As Fig. 4.13 shows, the micro liquid channels have random orientations within the mushy zone and they are not necessarily perpendicular to their local deformation rate vectors, *i.e.* $\vec{\delta}_{ext}^i$ is not parallel to the local z direction of channel i . Hence, Eq. (4.27) is further modified to yield the component of $\vec{\delta}_{ext}^i$ along the local z direction of the channel i as,

$$\delta_{z,ext}^i = \eta \frac{\delta(\vec{e}_Y \cdot \vec{e}_z^i)}{N_u} = \eta \frac{l(\dot{\epsilon}_{th} + \dot{\epsilon}_{re})(\vec{e}_Y \cdot \vec{e}_z^i)}{N_u}, \quad \begin{cases} \eta = 0 & \text{if } f_s \geq f_s^{coh} \\ \eta = 1 & \text{if } f_s < f_s^{coh} \end{cases} \quad (4.28)$$

where \vec{e}_Y and \vec{e}_z^i represent unit vectors in the global Y and the local z directions for channel i .

The deformation module uses this master equation, *i.e.* Eq. (4.28), to determine the local normal deformation rate of each micro liquid channel as a function of welding time. This deformation rate, representing the normal separation rate of the channel walls, accounts for both self-induced and externally applied strains, and varies for different welding conditions.

In summary, the deformation module characterizes deformation within the weld mushy zone as a function of welding conditions. In this module, all the strains including both internally and externally induced strains are considered. The module first receives welding conditions as input data. Then, it models the transient stress field that acts on the weld mushy zone resulting from solidification shrinkage and the response by the base metal. Using this stress field, the module then obtains the global strain rate across the weld mushy zone. Finally, the global strain rate is distributed among the micro liquid channels to calculate the local deformation rates induced by external sources.

4.4 Fluid flow module

The external deformation of the micro liquid channels during welding, along with the solidification shrinkage, acts as a driving force and sucks the molten metal from the weld pool into the mushy zone [12, 45, 130], inducing fluid flow throughout the network of micro liquid channels. As discussed in chapter 2, the characteristics of this fluid flow including pressure and flow rate play a key role in hot crack formation. The fluid flow module characterizes semisolid fluid flow within all the fluid channels that have not yet coalesced.

4.4.1 Mathematical approach

The fluid flow module implements a model for flow developed specifically by Sistaninia et al. [12] for application to granular models of solidification. In this model, the pressure drop across an individual micro liquid channel is related to the deformation characteristics of the channel, and flow is assumed to occur within the interconnected intergranular regions only and not through the interdendritic regions within grains.

As discussed in the work of Sistaninia [12], the flow in micro liquid channels can usually be assumed to be laminar and parallel to the facets of the micro liquid channel. Through these assumptions, the system can be described as Poiseuille flow between two parallel plates [12, 130]. By combining the Poiseuille flow equation describing the flow velocity with mass conservation across a micro liquid channel taking into account solidification shrinkage and deformation of the solid, the steady-state differential equation that governs the pressure field is given by,

$$\frac{2h'^3}{3\mu_l} \nabla^2 P_l = \beta(v_1^* + v_2^*) + \Delta v_{sn} \quad (4.29)$$

where h' and μ_l represent the half-thickness of the micro liquid channel and the dynamic viscosity of the liquid (given a value of 0.0023 (pa.s) [130]), P_l denotes the local pressure inside the channel, $\beta = (\frac{\rho_s}{\rho_l} - 1)$ is the shrinkage factor with ρ_l , and ρ_s being the densities of liquid and solid, v_1^* and v_2^* are the solidification velocities associated with each wall of the channel, and $\Delta v_{sn} = v_s - v_n$ measures the normal separation velocity of the channel walls caused by externally applied (augmented) strains and self-induced strains except for solidification shrinkage. Note that v_s and v_n denote the local velocities for the walls of a channel along the normal vector of the walls. Eq. (4.29) further assumes that the liquid inside the channel is incompressible and therefore ρ_l does not vary. The left hand side of Eq. (4.29), *i.e.* $\frac{2h'^3}{3\mu_l} \nabla^2 P_l$, represents the local velocity inside the channel while the right hand side represents the rate of the change in the size of the volume due to solidification shrinkage and externally applied deformation. Furthermore, Eq. (4.29) implies that the thickness of the micro liquid channel, itself a function of solid fraction, can significantly affect the local pressure and fluid velocity.

4.4.2 Numerical implementation

In this thesis, the fluid flow module developed by Sistaninia [12] for granular modelling of solidification was modified for application to welding. The module consists of a purpose-written finite element C++ code to solve Eq. (4.29) for the reconstructed mushy zone. Since

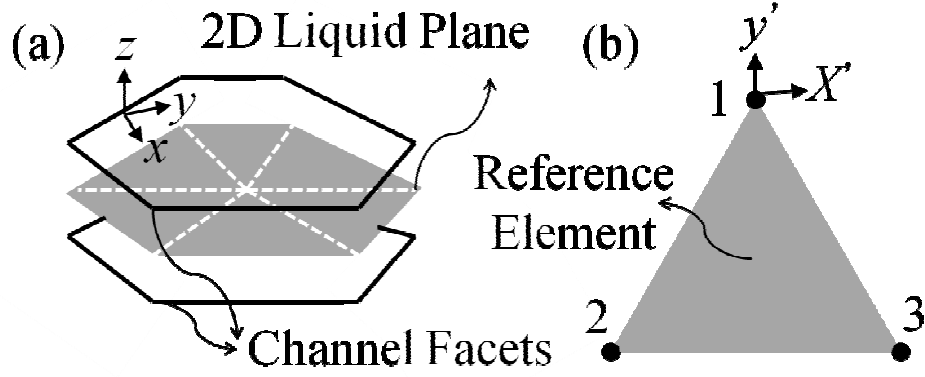


Fig. 4.14 (a) Schematic of a 2D plane inside a micro liquid, and (b) the triangular reference element.

it is assumed that the flow is parallel to the facets of each element, this module considers each 3D micro liquid channel as a 2D plane, as shown in Fig. 4.14a.

The 2D channels are then discretized into 3-noded 2D triangular elements for finite element analysis. In this technique, the pressure inside each triangular element is described by,

$$P_l = \sum_{i=1}^{i=3} N_i p_i \quad (4.30)$$

where N_i and p_i , ($i = 1,2,3$) denote the shape functions and nodal pressures of the triangular element shown in Fig. 4.14b in a reference coordinate systems (x', y', z') in which the z' direction is perpendicular to the surface of triangle, while $x' = y' = 0$ corresponds to node 1. The three shape functions of the reference element are given by [12],

$$N_1 = \frac{1}{2S_{sl}^e} [x'_2 y'_3 - x'_3 y'_2 - (y'_3 - y'_2)x' + (x'_3 - x'_2)y'] \quad (4.31)$$

$$N_2 = \frac{1}{2S_{sl}^e} [x'_3 y'_1 - x'_1 y'_3 - (y'_1 - y'_3)x' + (x'_1 - x'_3)y'] \quad (4.32)$$

$$N_3 = \frac{1}{2S_{sl}^e} [x'_1 y'_2 - x'_2 y'_1 - (y'_2 - y'_1)x' + (x'_2 - x'_1)y'] \quad (4.33)$$

where S_{sl}^e is the area of the triangular element e . Using the reference coordinate system along with the Galerkin finite element method [12], the discretized version of Eq. (4.29) for an arbitrary triangular element, e , can be written in matrix form as,

$$[K]^e \begin{Bmatrix} p_1 \\ p_2 \\ p_3 \end{Bmatrix} = \{b\}^e + \{\psi\}^e \quad (4.34)$$

where $[K]^e$, is the element stiffness matrix, $\{b\}^e$ denotes the body load vector associated with solidification shrinkage and externally applied strains, and $\{\psi\}^e$ is the boundary conditions vector associated with the intergranular flow leaving or entering the perimeter of the element e ,

$$[K]_{ij}^e = \frac{2h'^3}{3\mu_l} \int_{S_{sl}^e} \left(\frac{\partial N_i}{\partial x'} \frac{\partial N_j}{\partial x'} + \frac{\partial N_i}{\partial y'} \frac{\partial N_j}{\partial y'} \right) dS. \quad (4.35)$$

$$\{b\}_i^e = - \int_{S_{sl}^e} (\beta(v_1^* + v_2^*) + \Delta v_{sn}) N_i dS. \quad (4.36)$$

$$\begin{aligned} \{\psi\}_{ij}^e &= \int_{\partial S_{sl}^e} (\vec{q} \cdot \vec{n}) N_i d\Gamma = \int_{\partial S_{sl}^e} (q_{x'} n_{x'} + q_{y'} n_{y'}) N_i d\Gamma \\ &= \frac{2h'^3}{3\mu_l} \int_{\partial S_{sl}^e} \left(\frac{\partial N_j}{\partial x'} n_{x'} + \frac{\partial N_j}{\partial y'} n_{y'} \right) p_j N_i d\Gamma. \end{aligned} \quad (4.37)$$

In Eq. (4.37), $\vec{q} = (q_{x'}, q_{y'})$ is the fluid velocity vector field inside the micro liquid channel and $\vec{n} = (n_{x'}, n_{y'})$ represents the outward-pointing unit vector perpendicular to the perimeter of the element, ∂S_{sl}^e , in the reference coordinate system. The fluid flow module thus uses the internal and external normal deformation rates given by the deformation module to determine $\beta(v_1^* + v_2^*)$ and Δv_{sn} for each element.

After developing the stiffness matrix, load vector, and boundary conditions vector for each element, the fluid flow module assembles these matrices into the global system of equations, which is then solved numerically to obtain the nodal pressure values. The system of

equations is solved with a Conjugate Gradient linear iterative method using a free open source C++ program known as IML++ [131]. Note that the average size for the global stiffness matrix is 150,000 by 150,000 and therefore using Gaussian elimination techniques for solving the system of equations rather than iterative methods would be very computationally expensive.

Finally, a single pressure value is assigned to each triangular element, *i.e.* each micro liquid channel, through arithmetic averaging of nodal pressure values,

$$P_{ave} = \frac{\sum_{i=1}^3 p_i}{3} . \quad (4.38)$$

Further, the fluid velocity entering or leaving each micro liquid channels is given by,

$$\vec{q}^j = q_{x'}^j + q_{y'}^j = \frac{2h'^3}{3\mu_l} \int_{\partial S_{sl}^e|_j} \frac{\partial N_i}{\partial x'} p_i d\Gamma + \frac{2h'^3}{3\mu_l} \int_{\partial S_{sl}^e|_j} \frac{\partial N_i}{\partial y'} p_i d\Gamma \quad (4.39)$$

where $j = (1,2,3)$ denotes an edge, and $\partial S_{sl}^e|_j$ represents the length of the edge. The global system of equations will yield a unique answer if a well-posed domain [43] with known boundary conditions is defined. Therefore, it is important to discuss the geometry/domain and boundary conditions for the case of welding to ensure its suitability.

4.4.3 Domain and boundary conditions

As Fig. 4.15 illustrates, solving Eq. (4.34) over the RVE given by the solidification module requires knowledge of boundary conditions on the following surfaces: 1) inlet surface through which the molten metal enters the RVE, 2) outlet surface through which the liquid leaves the RVE, 3) top surface representing the top surface of the weld that is in contact with atmosphere, 4) fusion surface separating the weld mushy zone from the base metal, and 5) symmetry surface at the center of the weld.

There are two choices for fluid flow related boundary conditions. The first is to set an imposed pressure value (Dirichlet condition) on the boundary. The second is to set a boundary fluid velocity (Neumann), which itself is a function of $\frac{\partial p}{\partial n}$, *i.e.* the normal derivative of pressure. The boundary conditions on the fusion and the top surface are Neumann, and are

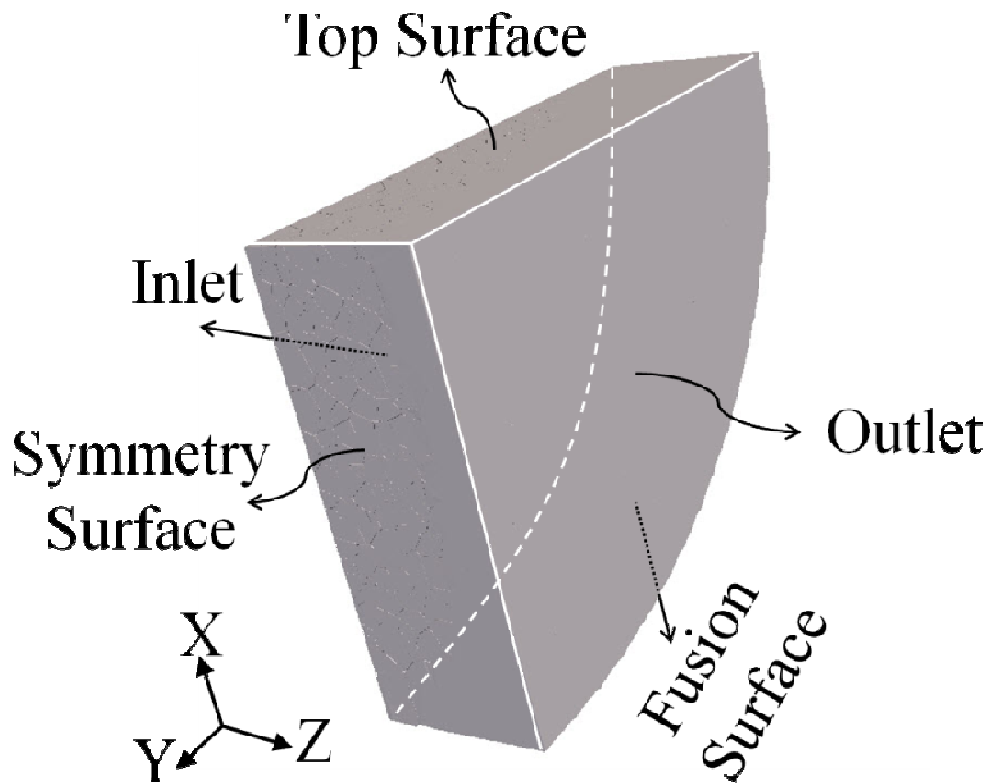


Fig. 4.15 Surfaces of the RVE analyzed by the fluid flow module.

set to $\vec{q} = 0$ since the molten metal cannot flow into a solid, nor escape into the atmosphere. On the symmetry surface, the boundary condition is homogeneous, *i.e.* $\frac{\partial p}{\partial n} = 0$. The inlet and outlet boundary conditions are however more complicated. Since the RVE can be located anywhere within the mushy zone³, the boundary fluid velocity and boundary pressure values on the inlet and outlet are, in general, also unknown. For each of these surfaces, there is only one position along the weld mushy zone at which the boundary condition is known. If the RVE is located right behind the weld pool, the boundary pressure on the inlet surface equals the static pressure inside the weld pool. Since the size of the weld pool is relatively small, this static pressure can be assumed to be the same as the arc pressure that acts on top of the

³ The RVE does not represent the entire mushy zone, but only a thin section with a given average solid fraction. Higher average solid fractions indicate that the selected RVE is closer to the fully solidified weld, whereas lower average solid fractions move the RVE near the weld pool.

weld pool. Conversely, if the RVE is located at the end of the weld mushy zone where the average fraction solid approaches 1, it can be assumed that $\vec{q} = 0$ on the outlet surface since liquid cannot flow into the fully solidified weld.

The above discussion implies that the fluid flow module can only be applied to an RVE consisting of the entire mushy zone extending from the weld pool to the fully solidified weld (Fig. 4.16). To overcome this limitation, the fluid flow module follows an iterative approach first proposed by Sistaninia [12] to generate a simulation of fluid flow within the whole mushy zone based on smaller-sized RVEs. As shown in Fig. 4.17, this whole mushy zone has continuity in average solid fraction at the interface between RVE blocks. The iterative process for determining the inlet and outlet boundary conditions on each of the RVEs and thus to solve Eq. (4.34) for the entire mushy zone is given below.

In the first step, the analysis of fluid flow begins by solving Eq. (4.34) in the RVE that is in contact with the solid weld, with an outlet boundary condition of $\vec{q} = 0$. Since fluid flow is a function of pressure gradient and not the actual pressure value [12], the pressure boundary condition for the inlet surface is not critical to the volume flow computation, and is simply set to an arbitrary value of zero. The nodal pressure values given by the solution of Eq. (4.34) are then used in Eq. (4.39) to calculate the fluid velocity field (\vec{q}) on the inlet surface of this RVE, which is shown as $q_{4,5}$ in Fig. 4.17. This velocity field is then imposed on the outlet surface of the next RVE, and the process is continued in a sequential fashion up to the last RVE that is in contact with the weld pool to obtain the fluid velocity field throughout the weld mushy zone.

The pressure field obtained in the first step can be only used for calculating the pressure gradient, not actual nodal pressures, since an arbitrary pressure boundary condition is initially applied to each of the inlet surfaces. In a second step, the analysis is repeated to correct the calculated nodal pressures. In this step, the process is reversed, beginning with the RVE in contact with the weld pool and setting the arc pressure as the boundary condition on the inlet surface. Here, the arc pressure is assumed to be 3 atm, *i.e.* the value measured in the welding experiments discussed in section 4.6. The fluid velocity field obtained in the first step is applied as the boundary condition at the outlet. This allows for calculation of the actual

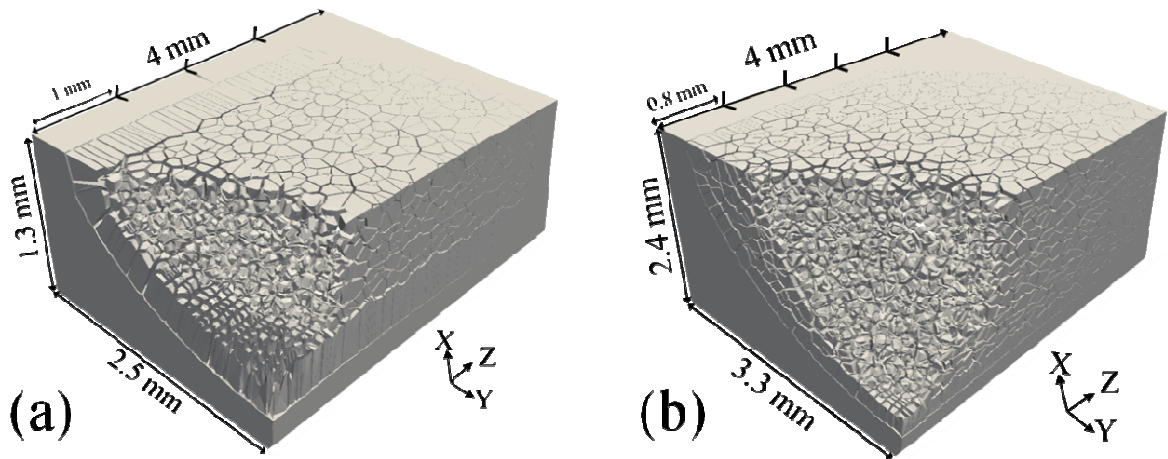


Fig. 4.16 The 3D view of the whole mushy zone reconstructed by the fluid flow module; (a) welding speed of 2 mm/s and welding current of 100 A, (b) welding speed of 4 mm/s and welding current of 120 A.

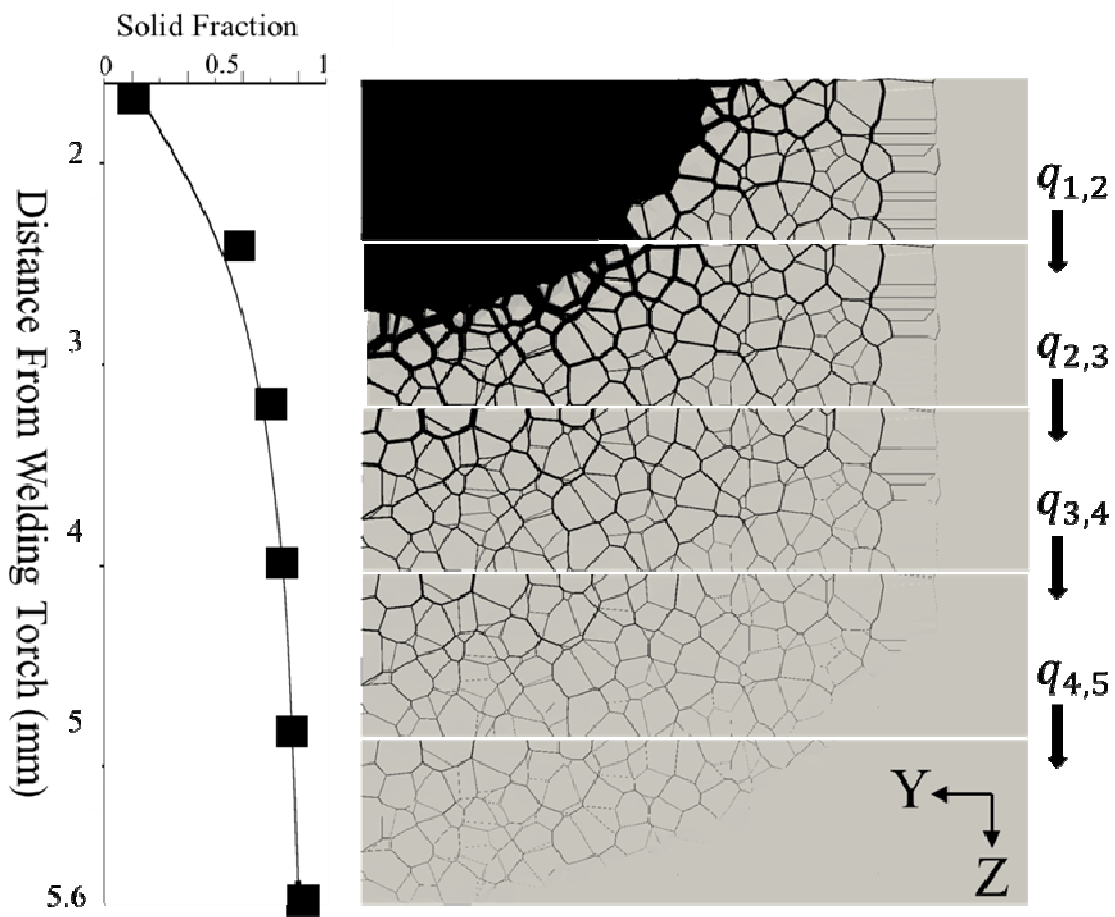


Fig. 4.17 The 2D top view of the mushy zone reconstructed by the fluid flow module. Here welding speed is 4 mm/s and welding current is 120 A.

pressure on the surface $q_{1,2}$. This process is continued until the pressure drop across the entire weld mushy zone is determined.

4.5 Defect formation module

The defect formation module implements three different micro-scale models to simulate the occurrence of hot cracks and hydrogen porosity during welding. Specifically, this module uses as inputs the local deformation rate, local pressure, and local fluid velocity from the solidification, deformation, and fluid flow modules to locate the triangular elements that are defected. Thus, all four modules are connected. For each of these defects, a defect index criterion is then defined within the entire RVE as,

$$Defect\ index = \frac{The\ number\ of\ defected\ elements}{The\ total\ number\ of\ elements} \times 100 . \quad (4.40)$$

The methods used for modelling these solidification defects are discussed below. Note that the defect formation module assumes that the defected elements do not influence the fluid flow analysis, nor the deformation analysis. Such an assumption is common in most studies on the formation of micro defects in semisolids [132-137].

4.5.1 Cracks

4.5.1.1 Kou's Model

The defect formation module applies Kou's micro-scale hot cracking criterion discussed in chapter 2 to determine whether cracking occurs in any of the triangular elements representing the micro liquid channels. In this criterion, a liquid channel cracks once the intergranular space opening rate exceeds the liquid feeding rate. The application of Kou's model, given in Eq. (2.3), requires the following terms: 1) the local normal deformation rate ($\frac{d\varepsilon_l}{dt}$), 2) the term $(1 - \beta)^m \frac{df_s^m}{dT} \frac{dT}{dt}$ representing the growth rate within the channel due to solidification, and 3) the term $\frac{d((1-(1-\beta)^m f_s^m) v_l)}{dz_{flow}}$ that is associated with the feeding rate inside the channel.

All of this information is available from this multi-scale and multi-physics model of solidification. Specifically, the summation of the internal and external normal deformation

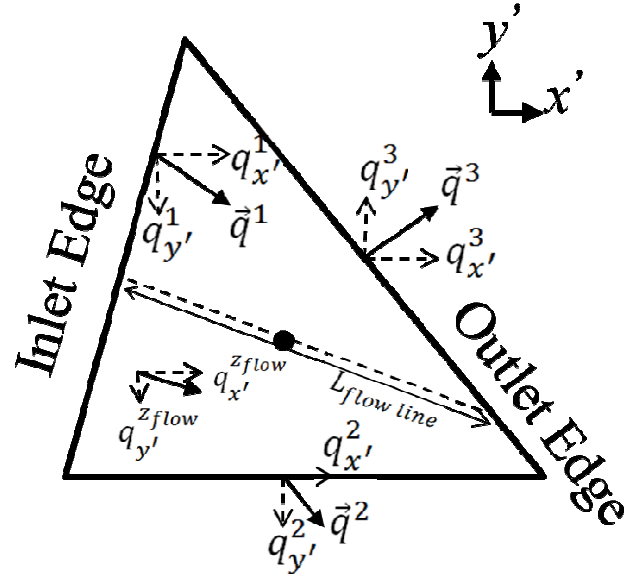


Fig. 4.18 Fluid velocity characteristics of a triangular element.

rates given by the deformation module is used to obtain $\frac{d\varepsilon_l}{dt}$, and the terms $\frac{df_s^m}{dT}$, $\frac{dT}{dt}$, and f_s^m are calculated directly by the solidification module. The only challenging term is $\frac{dv_l}{dz_{flow}}$, *i.e.* the first derivative of the fluid velocity along the flow direction. As Fig. 4.18 shows, the fluid flow module does not yield a single flow direction inside a triangular element – only a fluid velocity vector, $\vec{q}^j = q_{x'}^j + q_{y'}^j$, at each edge. To determine the dominant flow direction inside a triangular element, the arithmetic mean is taken from the components of each edge as

$$q_{x'}^{z_{flow}} = \frac{\sum_{j=1}^{j=3} q_{x'}^j}{3}, \quad q_{y'}^{z_{flow}} = \frac{\sum_{j=1}^{j=3} q_{y'}^j}{3} \quad (4.41)$$

where $q_{x'}^{z_{flow}}$ and $q_{y'}^{z_{flow}}$ are the components of the single flow direction. This flow direction is then used to identify the flow line within the element. This line is parallel to the flow direction and passes the center of the element as shown in Fig. 4.18. The edges that intersect the flow line represent the inlet and outlet edges, respectively. Since the triangular elements in this model are very small, the derivative of the fluid velocity along the flow direction can be obtained by,

$$\frac{dv_l}{dz_{flow}} = \frac{\|\vec{q}^{outlet}\| - \|\vec{q}^{inlet}\|}{L_{flow\ line}} \quad (4.42)$$

where, $\|\vec{q}^{inlet}\|$ and $\|\vec{q}^{outlet}\|$ represent the magnitude of the fluid velocity vector at the inlet and outlet edges, while $L_{flow\ line}$ denotes the length of the flow line confined between the inlet and outlet edges. Knowing all the required terms for the Kou's model, Eq. (2.3) is then applied to each triangular element to locate cracked elements.

4.5.1.2 Atmosphere-induced rupture model

As discussed in chapter 2, the liquid within the semisolid structure can also rupture due to propagation of the atmosphere-liquid interface at the top surface of the RVE into the micro liquid channels. Therefore, the micro-scale criterion given by Eq. (2.5) is used to simulate surface rupture for the weld mushy zone. Based on this propagation criterion, a surface micro liquid channel cracks once $P_a - P_l \geq \frac{2\gamma\cos\phi}{h}$, where P_a , P_l , and h are atmospheric pressure, local pressure inside the channel, and the width of the micro liquid channel, respectively. The $\gamma\cos\phi$ value can be fixed to 5 Jm^{-2} for aluminum alloys for channels containing an oxide skin, *i.e.* at the component's surface, and 2 Jm^{-2} for interior channels without an oxide skin. The defect formation module incorporates this criterion through a multi-step technique. The first step is intended to model initiation of surface rupture. In this step, Eq. (2.5) is applied to all the triangular elements that are connected to the top surface of the RVE. Since these elements are directly in contact with atmosphere, it is assumed that the interface is covered by a thin oxide layer. The elements that meet the surface rupture criterion are considered defected. The rest of the steps intend to model propagation of the initiated surface cracks into the weld mushy zone. In each of these steps, the cracking criterion is applied to the triangular elements that are connected to the defected elements identified by the previous steps. Using this technique, the propagation of the surface cracks is incrementally simulated. It is assumed that the surface cracks propagate immediately, and therefore the triangular elements involved in the propagation steps are oxide-free. The step in which no defected element is located is considered as the final step. In this model, P_a is assumed 1 atm, while P_l equals the average pressure inside the triangular element, *i.e.* P_{ave} , given by the fluid flow module.

4.5.2 Hydrogen porosity

As discussed in chapter 2, the dissolved gas in the weld pool facilitates cavitation. For aluminum alloys, it is shown that the dissolved hydrogen inside the molten metal is the main cause of porosity formation [7, 136]. In order to simulate nucleation of hydrogen porosity, a common technique for modeling formation of gas bubbles in molten metals [108, 136, 138] is applied in this module. In this method, it is assumed that gas bubbles nucleate from pre-existing gas pockets on dust particles and oxide films. In this technique, the mechanism behind nucleation revolves around the pore stability criterion discussed in chapter 2. According to this micro-scale criterion (Eq. (2.4)), a hydrogen pore forms once $P_H - P_l \geq \frac{2\gamma}{r}$, *i.e.* when the partial pressure of hydrogen inside the liquid (P_H) exceeds the local pressure of the liquid (P_l) by $\frac{2\gamma}{r}$. Therefore, Eq. (2.4) is applied to each triangular element to model the formation of hydrogen porosity. The required terms for this criterion are determined as follows:

In the defect formation module, only the porosity that form within the mushy zone is considered and not the bubbles that nucleate inside the weld pool. In other words, hydrogen porosity is assumed to form inside the micro liquid channels and not within an open liquid domain. Therefore, the pore radius, r , cannot exceed the half-width of the micro liquid channel (h'). Since the lower limit for the pore radius is unknown, h' given by the solidification module is considered as the pore radius to minimize $\frac{2\gamma}{r}$ and therefore simulate the worst case scenario in the formation of hydrogen porosity. In this module, $\gamma = 0.814 \text{ Nm}^{-1}$ [109], and the local pressure value, *i.e.* P_l , equals the average pressure inside a triangular element given by the fluid flow module, P_{ave} . The partial pressure of hydrogen inside a triangular element, P_H , requires further analysis to be determined. The hydrogen partial pressure corresponds to the concentration of hydrogen inside the micro liquid channel. According to Sivert's law [7], P_H (atm) is directly proportional to the dissolved hydrogen content inside the micro liquid channel, *i.e.* $[H]_l$ (ml/100g),

$$P_H = \left(\frac{[H]_l}{K_S}\right)^2 \quad (4.43)$$

where K_S is the Sivert's constant given by the Van't Hoff equation for aluminum alloys [109],

$$K_s = \exp\left(\frac{-2700}{T} + 2.72\right) \quad (4.44)$$

where temperature (T) is in Kelvin. The temperature field given by the solidification module is used to obtain T and therefore determine K_s for each triangular element during welding. According to Eq. (4.43), the dissolved hydrogen content inside the channel is still required in order to calculate the partial pressure of hydrogen. In aluminum alloys, hydrogen is much more soluble in the liquid phase rather than the solid phase, and therefore as the solid phase evolves within the weld pool, hydrogen will be rejected into the liquid phase. This results in a rising hydrogen content inside the micro liquid channels during welding. Assuming equilibrium at the solid-liquid interface and complete mixing inside a micro liquid channel, the Lever rule [109] is applied to determine the dissolved hydrogen content for a triangular element at any welding time,

$$[H]_l = \frac{[H]_o}{(1 - K_H)(1 - f_s) + K_H} \quad (4.45)$$

where $[H]_o$ denotes the initial hydrogen content inside the weld pool. It is assumed that hydrogen is uniformly distributed inside the weld pool and $[H]_o$ is an independent input variable. In Eq. (4.45), K_H represents the hydrogen partition coefficient, *i.e.* $\frac{[H]_s}{[H]_l}$, where $[H]_s$ is the hydrogen content in the solid phase. For AA6061, the hydrogen partition coefficient equals 0.05 [109]. f_s is obtained through the solidification module. Using Eqs. (4.43), (4.44), and (4.45), the partial pressure of hydrogen in each triangular element at any welding time is calculated. This allows for the application of the pore stability criterion (Eq. (2.4)) and consequently locating the defected elements by hydrogen porosity.

4.6 Welding Experiments

This section outlines the welding experiments performed to provide input information related to the grain structure and thermal analysis occurring under different welding conditions, along with image analysis performed to quantify the formation of defects during welding.

4.6.1 Process maps

In this study, a series of 28 bead-on-plate weld experiments were conducted in order to capture the required input parameters for the solidification module: depth of penetration, width of the weld, and length of the columnar zone. Welding speed and welding amperage were selected as independent variables. An automatic TIG welding machine was used to fabricate the welds, on aluminum AA6061 plates, 200 mm long, 100 mm wide, and 3 mm thick. Prior to welding, each plate was cleaned using a three-step procedure. The plates were first mechanically polished and then were cleaned by Ethanol. Finally, a blow dryer was used to dry the plates. After cleaning, the plates were tightly clamped on the automatic TIG welding machine. Prior to each welding, the tungsten electrode was sharpened using an electrode sharpener. The same stand-off distance between the electrode and the base metal was applied to all the welds to ensure consistent welding voltage. Also, pure argon gas with a constant flow rate of 18 (cfh) was used to protect all the welds. Note that welding conditions in this thesis are identified by VXIXXX, where the digit following V is welding speed (mm/s) and the digits following I show welding current (A).

At the completion of the experiments, each welded specimen was analyzed via optical microscopy in order to extract the macro-scale weld characteristics as a function of process parameters. The resulting relation defines the variation of the RVE (size of the cuboid and also the size of the fusion zone) with respect to welding parameters. Fig. 4.19a and b illustrate the measurement methodology, while Fig. 4.20a and b provide process maps for these two characteristics. Electron Backscattered Diffraction (EBSD) imaging was then used to detect the location of the columnar zone within the fusion weld pool and to calculate an average columnar grain length. The process map for this characteristic is shown in Fig. 4.20c. Note that in this process map, the values for columnar grain length have been normalized with respect to the depth of penetration since smaller welds normally have smaller absolute values for columnar grains and vice versa. The details of the results for eight different welding conditions are listed in Table 4.1.

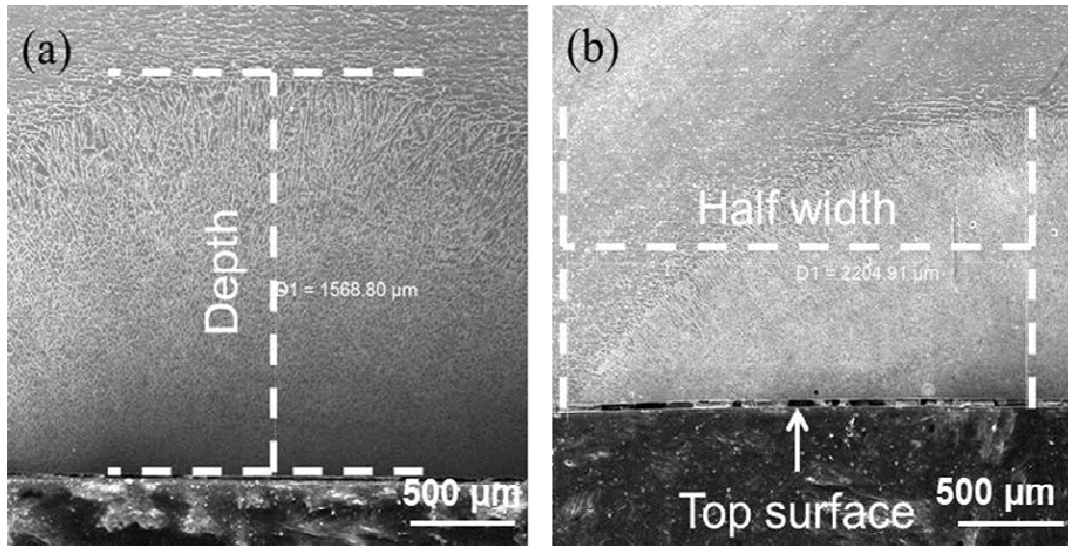


Fig. 4.19 Example scanning electron microscopy images showing the measurement methodology for (a) depth of penetration, and (b) weld width.

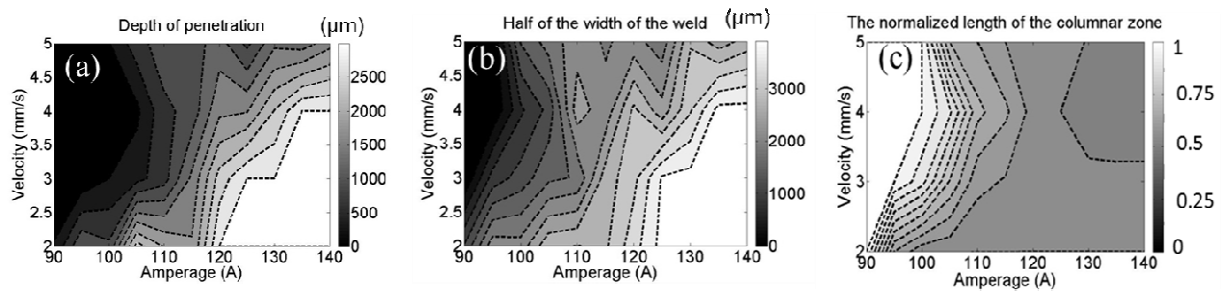


Fig. 4.20 Process maps from welding experiments linking weld characteristics to welding parameters including amperage and speed: (a) Depth of penetration, (b) Weld half-width, and (c) Normalized length of the columnar zone.

The obtained results and process maps are utilized as input data since they link the weld geometry and microstructure to welding parameters, and therefore enable the RVE used for the solidification module to vary based on welding procedure. As can be seen in Fig. 4.20, slow welding speeds, and high welding currents leading to high welding powers, yield RVEs with larger welds but with a microstructure in which the columnar zone is shrunk. On the other hand, lowering the welding power and increasing the welding speed will lead to RVEs with smaller welds and longer columnar grains.

Table 4.1 Welding parameters and resulting microstructure characteristics.

Case study	Welding speed (mm/s)	Welding amperage (A)	The size of the base metal grains (μm)	The length of the columnar grains (μm)	The size of the equiaxed grains (μm)	Depth of penetration (μm)	The half width of the weld (μm)
V2I110	2	110	80	220	65	2300	3300
V3I105	3	105	80	220	55	800	2000
V3I120	3	120	80	330	60	2800	3500
V4I110	4	110	80	350	48	1100	2800
V4I130	4	130	80	130	65	2700	3500
V5I105	5	105	80	310	55	1000	2200
V5I125	5	125	80	130	65	1100	2200
V5I140	5	140	80	140	68	2000	3100

4.6.2 Thermal analysis

As discussed in section 4.2.2, thermocouple data obtained from the welding experiments was used to calibrate the Rosenthal equation predicting the temperatures in the mushy zone and in the base metal. The main unknown in Eq. (4.1) is Q , since the actual heat transferred from the torch to the metal will depend on the welding conditions. This heat transfer coefficient was used as a fitting parameter to match the predictions made by the Rosenthal equation to thermocouple data from each of the 28 welding experiments with each experiments having a different Q value. Specifically, maximum temperature was considered as the main matching criterion. Since the Rosenthal equation does not account for time, but instead outputs the thermal field around the weld pool at steady-state, the quasi-static approximation was applied. Specifically, as the welding torch travels, the quasi-static isothermal surfaces attached to the weld pool also travel. Thus, a given point on the workpiece experiences variations in temperature during welding. In this model, the isothermal surfaces given by the Rosenthal equation were moved with the same traveling speed as of the welding torch to plot the thermal histories of the desired points. The results from one example fitting exercise are given in Fig. 4.21, for a weld fabricated at welding speed of 5 mm/s and welding current of 140 A. Fig. 4.21a and b show the location of these points in relation to the weld line. The obtained thermal histories corresponding to three thermocouples are shown in Fig. 4.21c. As can be seen, an excellent fit is found between the experiments and the predictions from the fitted Rosenthal equations.

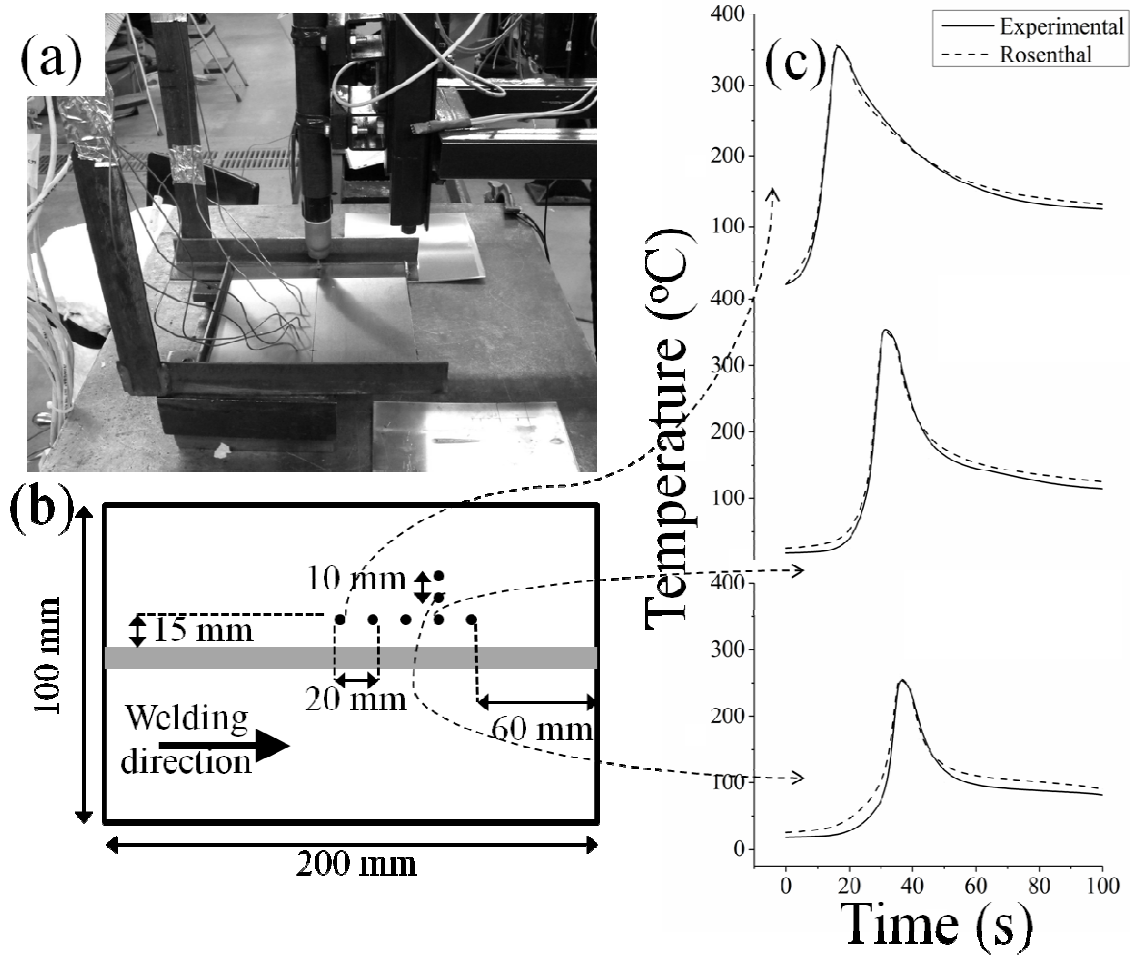


Fig. 4.21 (a) Experimental setup before welding; (b) Schematic of the location of the thermocouples, and (c) the numerical and experimental thermal histories of the three points shown in part (b).

4.6.3 X-ray Tomography

The experimental welded coupons listed in Table 4.1 were then analyzed to investigate the effects of welding current and welding travel speed on the formation of hot cracks and porosity. Specifically, X-ray micro-computed tomography (μ CT) was carried out on each sample, at the midpoint of the weld line, to reveal the internal defects. The tomographic imaging was performed using a Zeiss μ XCT-400 computed tomography microscope, acquiring 3D images at a voxel size of 0.9 mm. Each 3D data set was post-processed using the Avizo software to reduce noise and extract internal defects in order to qualitatively characterize the internal porosity and hot tears. Specifically, a median filter was applied to

reduce noise, and then a manual threshold value was applied to segment the defects from the background for each weld sample.

4.7 Computation

The developed multi-physics model utilizes several programming languages. Specifically, the 3D multi-scale microstructure of the weld, the solidification module, and the fluid flow module are directly developed using the C++ programming language (Visual Studio Express 2012). In addition, the thermal analysis module utilizes Matlab (Release 2010a), and the deformation module uses a combination of Fortran (Intel Fortran 77 compiler 14.0), C++, and the Abaqus commercial finite element software (Abaqus 6.10) in order to characterize the deformation of the weld mushy zone. All the modules of this model are compatible with a standard desktop Personal Computer, without any special configurations. The results presented in this thesis are all obtained using a PC equipped with an Intel Core i7 processor, 8 GB of Random-Access-Memory (RAM), and a Windows 7 operating system. The collective total running time for all these modules on such a hardware is approximately ~90 minutes.

5 Results and Discussion

In this chapter, the application of the multi-physics meso-scale model of solidification to study hot cracking during welding is presented. First, the results of the solidification module are discussed. This includes an analysis of the reconstructed mushy zone as well as a study examining the role of welding parameters on the semisolid weld characteristics. Second, the estimates of semisolid deformation made by the deformation module are presented through two major topics : 1) evolution of the transient stress field acting on the weld mushy zone, and 2) local deformation rates inside the micro liquid channels induced by solidification shrinkage and the transient stress field. The effects of welding conditions on the deformation of the weld mushy zone are also discussed. Third, the pressure field within the weld mushy zone given by the fluid flow module is analyzed in order to study the role of welding conditions on the liquid pressure inside the weld mushy zone. Fourth, the predictions made by the defect module upon combining all three prior models are presented and discussed. Specifically, the effects of welding conditions on the formation of hot cracks and hydrogen porosity is studied through analysis via the different defect indices corresponding to the defect formation models in chapter 4. Finally, using the X-ray tomography results, a qualitative study has been carried out in order to investigate the role of welding conditions on the formation of solidification defects.

5.1 Solidification⁴

As discussed in section 4.2, the solidification module is intended to reconstruct the evolving microstructure of the weld mushy zone. This microstructure, composed of solid grains and a network of micro liquid channels, acts as the geometry for the other modules. Also, since the features of the weld mushy zone developed by this module vary as a function of welding parameters, one can study the effects of welding conditions on the characteristics of the weld mushy zone. In this study, the impact of welding parameters on the width of the micro liquid channels is studied through analysis of the results of the solidification module.

⁴ This section has been published in : Zareie Rajani, H. R., Phillion, A. B., “A mesoscale solidification simulation of fusion welding in aluminum–magnesium–silicon alloys” *Acta Materialia* 77 (2014): 162-172.

5.1.1 Structural analysis of the semisolid weld

Fig. 5.1 shows the type of solidification result that can be obtained under transient welding conditions for the AA6061 alloy. The welding conditions were a welding speed of 3 mm/s and an amperage of 120 A, giving a depth of penetration of 2.8 mm, a weld half-width of 3.5 mm, and a grain size of 330 μm in the columnar region and 60 μm in the center-line weld region. The total number of grains simulated was 4562. As can be seen in Fig. 5.1, the model is able to reconstruct the evolution in welding microstructure with time. In this figure, the empty space represents the liquid phase, and the filled space represents the individual solid grains.

At a welding time of zero, the RVE is only composed of base metal and a fully liquid weld pool, corresponding to the $t=0$ image in Fig. 4.1. At this point, all of the elements within the weld pool are assumed to be in the liquid state. As the welding torch advance, the RVE cools, enabling solidification. Solidification is initiated close to the fusion surface, and as shown in Fig. 5.1a (0.2 s after start of welding), the solidifying columnar grains start to grow towards the weld centerline. The elements within the solidifying grains are each composed of both liquid and solid, though only material that is solid can be seen. At each time-step, the nodal temperatures are calculated using the Rosenthal equation, and the location of the solid/liquid interface is determined assuming Scheil conditions for solidification. As time progresses, the equiaxed grains at the center of the weld will gradually start to form, and eventually block the growth of the columnar zone, resulting in a Columnar-to-Equiaxed transition (CET). Note, however, that the model does not specifically simulate the CET since the length of the columnar zone is fixed as a model input based on the experimental data shown in Figs 4.19 and 4.20. The state at which the centerline equiaxed grains first nucleate and block the advancing columnar grains is shown in Fig. 5.1b, 0.7 s after start of welding. Fig. 5.1c, 1.8 s after start of welding, represents the microstructure at a later time once the welding torch has moved further away from the RVE. Overall, Fig. 5.1 shows the formation and evolution of micro liquid channels within the mushy zone. These channels are located along the grain boundaries, and form a continuous network of liquid linking the base of the columnar grains with the center of the weld pool. As solidification proceeds, smaller channels will close while larger ones remain open. As can be seen, the micro liquid channels become narrower with the

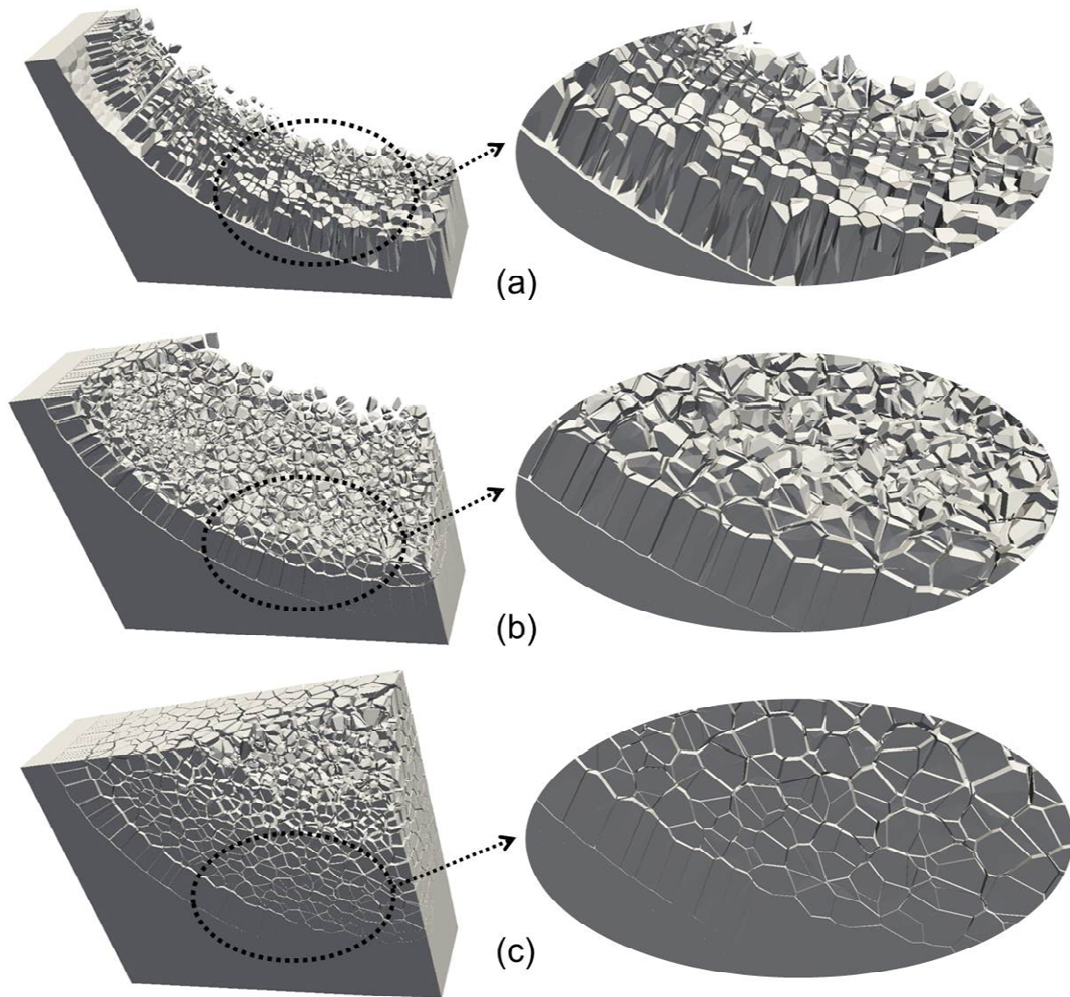


Fig. 5.1 The gradual evolution of the weld mushy zone as predicted by the model at welding time of (a) 0.2 s, (b) 0.7 s, and (c) 1.8 s. The weld was fabricated using a welding speed of 3mm/s and welding amperage of 120 A.

transition from Fig. 5.1a to Fig. 5.1c; at later stages they will finally become blocked due to coalescence.

The ability of the present model to create a mushy zone structure at the meso-scale composed of many solidifying grains and an interlocking network of micro liquid channels is an important step towards modelling solidification defects [14, 114]. In comparison, existing solidification models for welding are not able to provide a proper replica of the structure of the semisolid weld upon which to perform fluid-flow and deformation simulations [11, 12] for predicting hot cracking and porosity. The majority of the previous models (e.g. [40, 42,

44]) focus on only a few grains, and thus, cannot simulate the network of micro liquid channels. Although some of the models extend their simulation domain over a larger number of grains (e.g. [45, 84]), they still suffer from ignorance of the third dimension. Sistaninia *et al.* [12] has shown that consideration of 3D effects is key for predicting hot crack formation since it strongly affects the continuity of the micro liquid channel network.

5.1.2 Effect of welding procedure on semisolid weld characteristics

The new multi-scale welding model can be used to investigate the effects of welding procedure on semisolid weld characteristics. A key microstructural feature affecting the feeding ability of the mushy zone is the width of the micro liquid channels [12, 14]; the wider the channels are, the easier they can feed the molten metal into to the solidifying weld pool and hence reduce hot cracking. The micro liquid channels within a semisolid medium can be classified into two major types: 1) interdendritic micro liquid channels that circulate the molten metal through the interdendritic spaces within a solidification envelope and affect the micro-scale feeding ability of the mushy zone, and 2) intergranular micro liquid channels forming between neighbour grains that feed molten metal into the interdendritic micro liquid channels, and affect the meso-scale feeding ability of the mushy zone. Since the current model does not simulate the dendritic feature of the grains, it can only analyze the meso-scale feeding ability of the semisolid weld, and therefore, the micro liquid channels in this study all refer to intergranular micro liquid channels.

As shown in Fig. 4.2, the choice of welding speed and welding power directly affects grain morphology. The flexibility of the new multi-scale welding model enables study of these effects in order to link variability in the width of the micro liquid channels to processing. Figs. 5.2 to 5.4 present an analysis showing the effects of grain manipulation techniques and welding parameters on the average width of the micro liquid channels, along with the standard deviation. The calculation of average width is based on the fraction solid within an element, as shown below,

$$W_c = L - X^* = L(1 - \sqrt[3]{f_{s(T_s/l)}}) \quad (5.1)$$

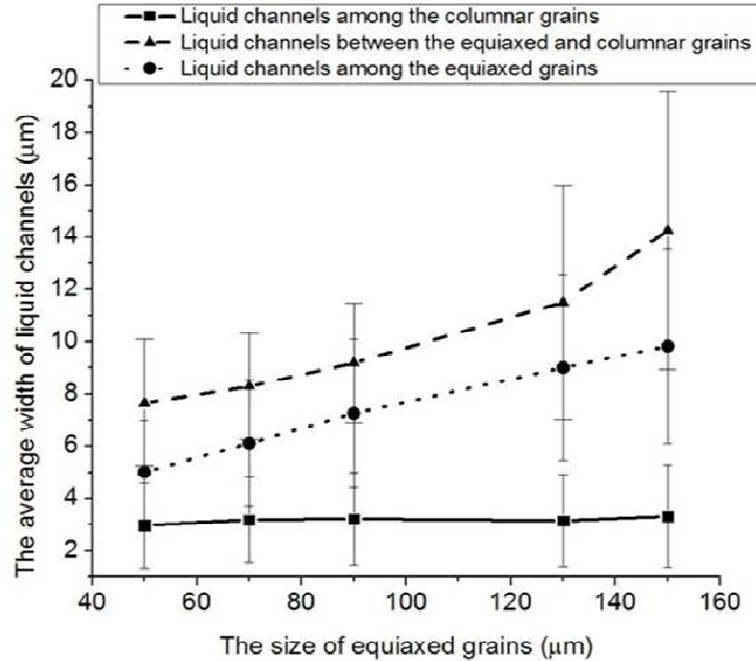


Fig. 5.2 Process map from a series of simulations examining the effect of equiaxed grain size at the center of the weld on the average width of the micro liquid channels near grains with high f_s .

where W_c is the half-width of a micro liquid channel, X^* denotes the perpendicular distance from the apex of the tetrahedron to the solid/liquid interface, and L is the perpendicular length of a tetrahedral element. As the critical solid fraction in which the feeding ability of the weld pool will directly influence hot cracking is known to occur between $0.8 < f_s < 0.9$ [7, 123], the analysis was only carried out on micro liquid channels located between grains in this range. This range was chosen because good feeding is known to occur at values less than $f_s = 0.8$, while little or no feeding is assumed to occur for $f_s > 0.9$. Moreover, since the microstructure of the weld pool is composed of both columnar and equiaxed grains, the micro liquid channels were classified into three different groups based on location: amongst the columnar grains, between columnar and equiaxed grains, and finally amongst the equiaxed grains at the center of the weld. Note that both the average width of micro liquid channels for each group and the corresponding error with a confidence interval of 68% are reported.

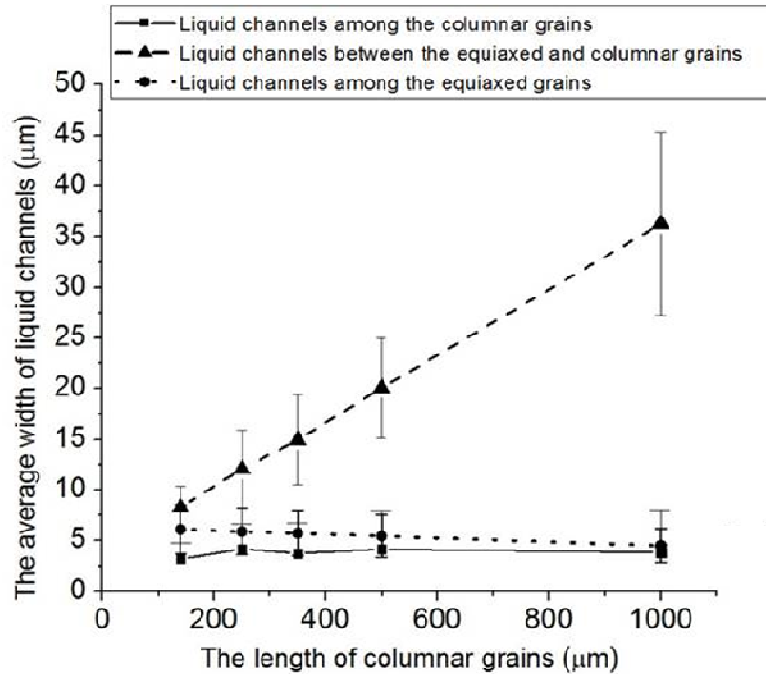


Fig. 5.3 Process map from a series of simulations examining the effect of columnar grain length on the average width of the micro liquid channels near grains with high f_s

The effect of grain manipulation techniques such as addition of nucleants to the weld pool on micro liquid channels is shown in Fig. 5.2 (equiaxed grain size) and Fig. 5.3 (length of columnar grains). In these simulations, a welding speed of 5 mm/s and amperage of 140 A was assumed. As can be seen in both figures, the weld mushy zone does not have a uniform network of micro liquid channels, and therefore different areas of the weld show a non-uniform feeding ability. This is due to the use of a Voronoi tessellation to create the microstructure, which causes non-uniformity in grain size and in micro liquid channel width.

Returning to Eq. (5.1), it can be seen that for a given solid fraction, the length of the element (L) is the only term that affects the width of the liquid channels. In other words, a dense arrangement of nuclei generates smaller elements and consequently causes channels to shrink, whereas a sparse arrangement of nuclei creates wider channels at the same solid fraction. Fig. 5.2 shows that lowering of the density of equiaxed nuclei, and thus enlarging the equiaxed grains at the center of the weld widens the micro liquid channels both amongst the equiaxed grains and also between the columnar and equiaxed regions. In this case, since

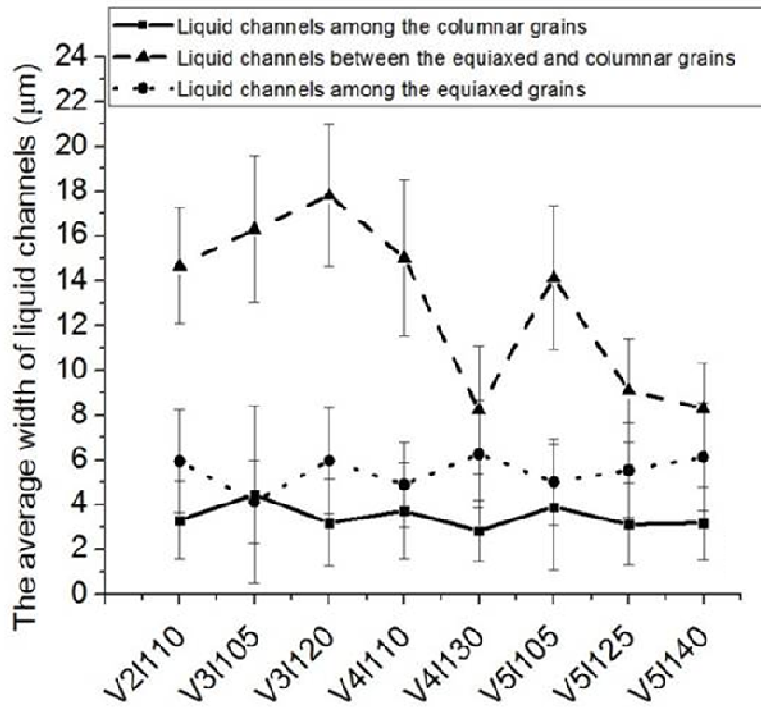


Fig. 5.4 Process map from a series of simulations examining the effect of welding parameters on the average width of the micro liquid channels near grains with high f_s .

the arrangement of the columnar nuclei remains unchanged, the width of these channels does not vary. Fig. 5.3 shows that the length of the columnar grains also has little effect on the size of the micro liquid channels within the mushy zone, neither within the columnar zone nor within the equiaxed zone. Together, however, Figs. 5.2 and 5.3 reveal that the micro liquid channels between the columnar and equiaxed grains are always the widest, and that the micro liquid channels amongst the columnar grains usually have the smallest width. This observation can be explained through the fact that the columnar grains are normally quite long, and therefore there is a severe lack of nuclei through the area between the columnar and equiaxed nuclei. On the other hand, the dense arrangement of the columnar nuclei shrinks the channels among the columnar grains as compared to the equiaxed grains.

The influence of welding parameters on the micro liquid channels is shown in Fig. 5.4. The results for eight different case studies, listed in Table 4.1, are given. In these cases, the welding speed was varied from 2 to 5 mm/s while the amperage was varied from 110 – 140

A. The results indicate that welding parameters strongly affect the width of the liquid channels in different areas of the mushy zone and consequently affect the feeding ability of the solidifying weld pool. These observations are due to the fact that various welding parameters change the microstructure and consequently the arrangement of the solidification nuclei within the weld. For instance, the narrow micro liquid channels between the columnar grains and the equiaxed grains for a weld fabricated by welding speed of 4 mm/s and amperage of 130 A can be associated with the short columnar grains in this weld (Fig. 4.20).

Since the structural characteristics of a semisolid medium affect the deformation behaviour [12] and feeding ability [11] of the semisolid, and consequently formation of hot cracks [99], the obtained results of the solidification module suggest that welding procedure directly influences the formation of hot cracks within the weld pool. Hence, modification of welding procedure can be assumed as a potential technique to prevent hot cracking in welding.

5.2 Deformation of the semisolid weld⁵

As discussed in section 4.3, the deformation module enables characterization of the transient deformation of the weld mushy zone as a function of welding conditions. Specifically, the normal deformation rate of the micro liquid channels due to solidification (internal deformation rate) and thermo-mechanical/augmented strains (external deformation rate) are investigated.

5.2.1 Internal normal deformation rate

Using the technique detailed in section 4.3.1, the model simulates the normal deformation rate of the micro liquid channels caused by solidification shrinkage. Note that the deformation of a micro liquid channel refers to enlargement of the space confined inside the channel due to separation of channel walls, and not deformation as generally applied within solid mechanics.

⁵ Part of this section is published in: 1) Zareie Rajani, H. R., Phillion, A. B., "A Multi-scale Thermomechanical-Solidification Model to Simulate the Transient Force Field Deforming an Aluminum 6061 Semisolid Weld", *Metallurgical and Materials Transactions B* 46.4 (2015): 1942-1950, and 2) Zareie Rajani, H. R., Phillion, A. B., "3D multi-scale modelling of deformation within the weld mushy zone", *Materials & Design* 94 (2016): 536-545.

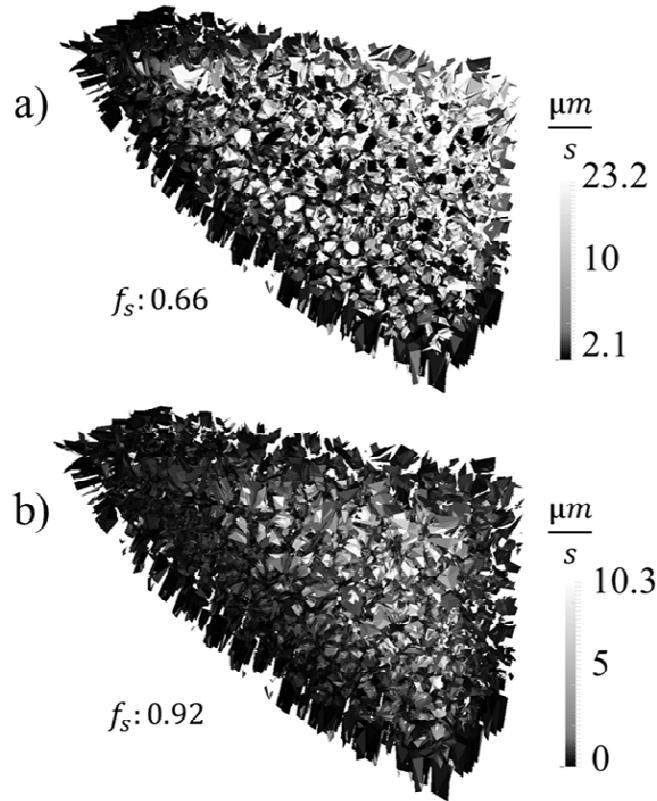


Fig. 5.5 The internal normal deformation rate of the micro liquid channels within the reconstructed mushy zone of a weld for (a) an average solid fraction of 0.66 and (b) an average solid fraction of 0.92. The weld is fabricated by a welding velocity of 4 mm/s and a welding current of 120 A.

The variation in the internal normal deformation rate within the reconstructed mushy zone of a weld is depicted in Fig. 5.5 for two different average solid fractions, 0.66 and 0.92. The numerically reconstructed mushy zone corresponds to a welding velocity of 4 mm/s and a welding current of 120 A. For a constant average solid fraction during welding, the results show that the internal normal deformation rates are highest when the channels are closer to the symmetry surface, *i.e.* closer to the center of the mushy zone. This result indicates, through Eq. (4.12), that the micro liquid channels at the center of the weld have higher solidification velocities and consequently experience larger solidification shrinkage. As discussed in Section 4.2.3, higher temperatures and higher cooling rates increase the solidification velocity and lead to faster separation of the walls of the micro liquid channels. Therefore, this variation in the internal normal deformation rate can be associated with a

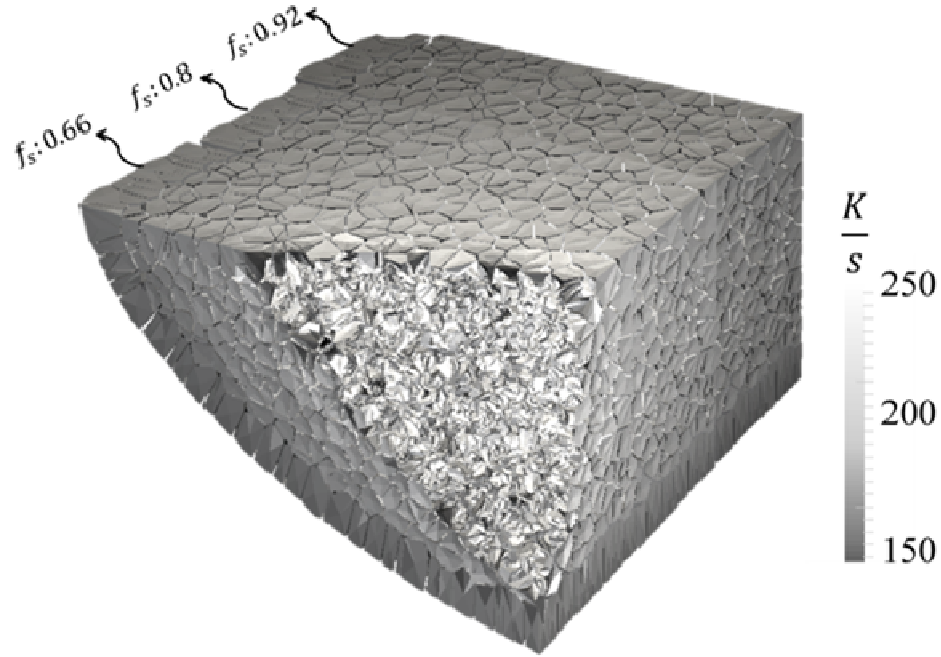


Fig. 5.6 The cooling rate over the mushy zone of a weld fabricated by a welding travel speed of 4 mm/s and a welding current of 120 A.

nonuniform thermal field within the mushy zone. Fig. 5.6 shows the distribution of the cooling rate over a reconstructed mushy zone corresponding to a welding travel speed of 4 mm/s and a welding current of 120 A. As can be seen, the cooling rate is highest at the center of the mushy zone. Also, the micro liquid channels at the center of the weld have the highest temperatures since they are closer to the heat source [7].

Comparison of Figs. 5.5a and b reveals that the variation in the internal normal deformation rate is strongly dependent on the average solid fraction of the domain. In order to analyze this relationship, the average internal normal deformation rate, $\bar{\delta}_{z,int}$, has been calculated at various average solid fractions as,

$$\bar{\delta}_{z,int} = \frac{\sum_{i=1}^{i=N} \delta_{z,int}^i}{N} \quad (5.2)$$

where N represents the total number of micro liquid channels within the mushy zone at a specific average solid fraction.

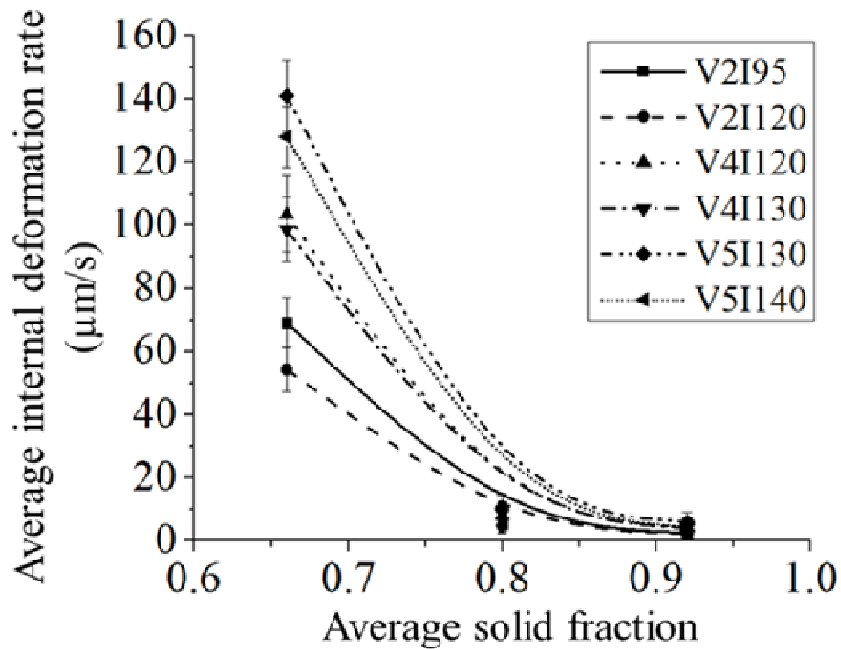


Fig. 5.7 The variation of the average internal normal deformation rate as a function of average solid fraction for various welding parameters.

Fig. 5.7 shows the variation in $\bar{\delta}_{z,int}$ as a function of average solid fraction for various welding conditions. As mentioned earlier in chapter 4, each welding condition is labeled as VXIXXX where the single digit after V shows the simulated welding travel speed in mm/s and the digits following I indicate the simulated welding current in Amperage. Examining any one curve, *e.g.* V2I95, it can be seen that increasing the average solid fraction of the mushy zone significantly reduces $\bar{\delta}_{z,int}$. This effect can be linked to the fact that at higher average solid fractions the mushy zone becomes colder and the cooling rate also drops, see Fig. 5.6, leading to a reduction in the solidification velocity. By comparing different curves, it can be seen that (1) increasing the welding travel speed increases $\bar{\delta}_{z,int}$ for a given average solid fraction and (2) lower welding currents at a constant welding travel speed slightly increase the average internal normal deformation rate. These observations can be associated with the role of welding parameters on the thermal field of the mushy zone; lower welding currents at a constant welding travel speed lead to higher maximum cooling rates within the mushy zone and consequently higher $\bar{\delta}_{z,int}$.

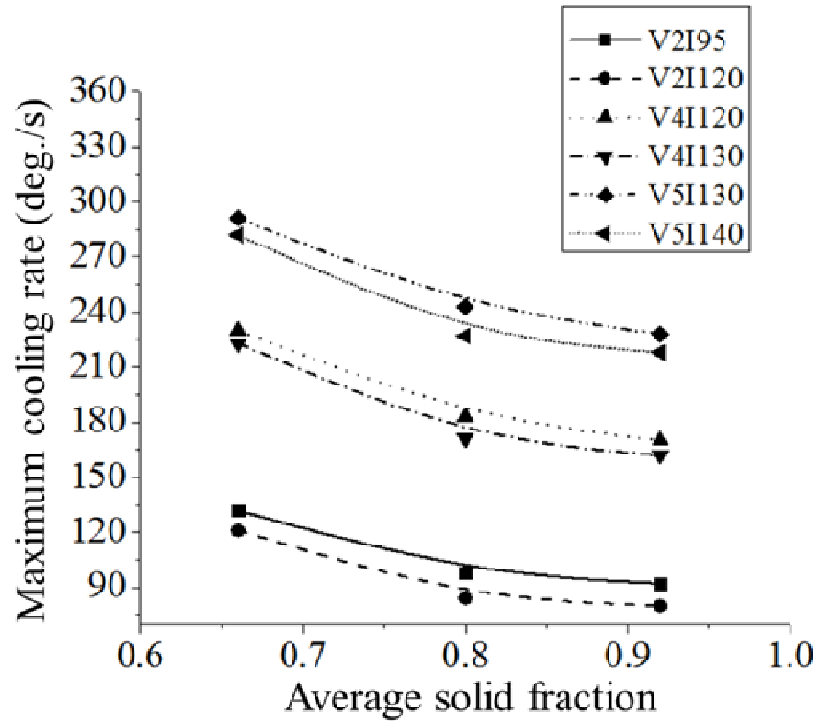


Fig. 5.8 The variation of the maximum cooling rate along the mushy zone of six welds fabricated by different welding parameters.

The maximum cooling rate inside the mushy zone as a function of average solid fraction for the various welding conditions is shown in Fig. 5.8. Additional simulations, not shown, indicate that the effect of the weld microstructure on the internal normal deformation rate is negligible. Specifically, applying the same thermal field to various weld microstructures shows little variation in the average internal normal deformation rate. This demonstrates that welding parameters modify the internal normal deformation rate mainly because of their ability to change the thermal field, and not the corresponding change in weld microstructure.

5.2.2 External normal deformation rate

As discussed in section 4.3.2, the process of simulating the external normal deformation rate of the micro liquid channels consists of three steps. First, the transient force field caused by thermo-mechanical and external sources is modeled. Second, using the transient forces, the global deformation rate across the weld mushy zone is calculated. Finally, the global

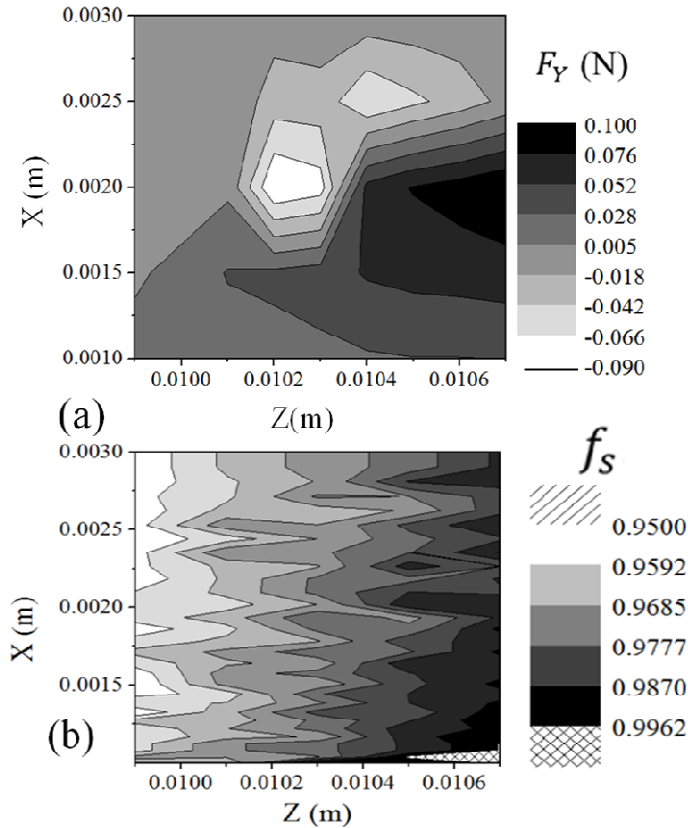


Fig. 5.9 (a) The lateral component of the force field acting on the fusion surface of the semisolid weld at welding time of $t=1.8$ s; (b) The corresponding distribution of the solid fraction projected on the fusion surface.

deformation rate is partitioned to individual micro liquid channels. The results of each of these steps are discussed below.

5.2.2.1 External transient force field

Since the deformation of the semisolid weld is dominated by lateral stresses [7, 126], *i.e.* the stresses normal to the weld line, the deformation module focuses on the Y component of the simulated force field. Fig. 5.9a shows the spatial variation in the lateral component of the calculated force field acting on the fusion surface at welding time of $t=1.8$ s. The weld is fabricated on a clamped aluminum 6061 plate using a welding current of 120 A and a welding speed of 3 mm/s. Welding time of zero is assumed to be the time at which solidification begins in this section of the weld. Also, note that positive force values represent

tensile lateral forces, while negative force values are associated with compressive lateral forces. Fig. 5.9b shows the variation in solid fraction across the fusion surface. Although the calculated forces are closely linked to the solidification behaviour, as can be seen the variation in solid fraction across the fusion surface is considerably less than the variation in the simulated force field.

Based on the obtained results, the transient external force field has a complex nature where both tensile and compressive forces simultaneously act on the semisolid weld. Such behaviour can be linked to the complex nature of deformation within the base metal, where non-uniform transient thermal stresses combine with transient solidification contraction and also externally applied forces to control the material flow.

The obtained results are then used to determine the average tensile stress acting on the semisolid weld. To calculate this value, the tensile force components in Y that apply on bar elements (Fig. 4.9) with $f_s > f_s|_p$ are averaged and then divided by the percolated area of the fusion surface. The calculated average tensile stresses acting on the fusion surface of clamped AA 6061 semisolid welds as a function of time fabricated by various welding parameters are shown in Fig. 5.10 for different welding speeds between 2 and 5 mm/s. The results indicate that at a constant welding speed, increasing the welding current generates larger average tensile stresses. In other words, using higher welding currents at a fixed welding speed will increase the risk of severe deformation within the semisolid weld, and will make the weld more susceptible to hot cracking. Such an observation can be explained through the phenomenon of solidification shrinkage. By increasing the welding current, larger welds form, leading to larger amounts of solidification contraction, as given by Eq. (4.15). Higher magnitudes of shrinkage contraction will then create larger reaction forces on the fusion surface. This result qualitatively matches prior experimental studies [94], where it was shown that high welding current and large weld pools increase the risk of hot cracking.

Fig. 5.10 indicates that the welding speed also affects the average tensile stress deforming the semisolid weld. As shown in Fig. 5.10a, the maximum average tensile stress is relatively low at a low welding speed of 2 mm/s, but rises significantly (Figs. 5.10b and c) with increasing

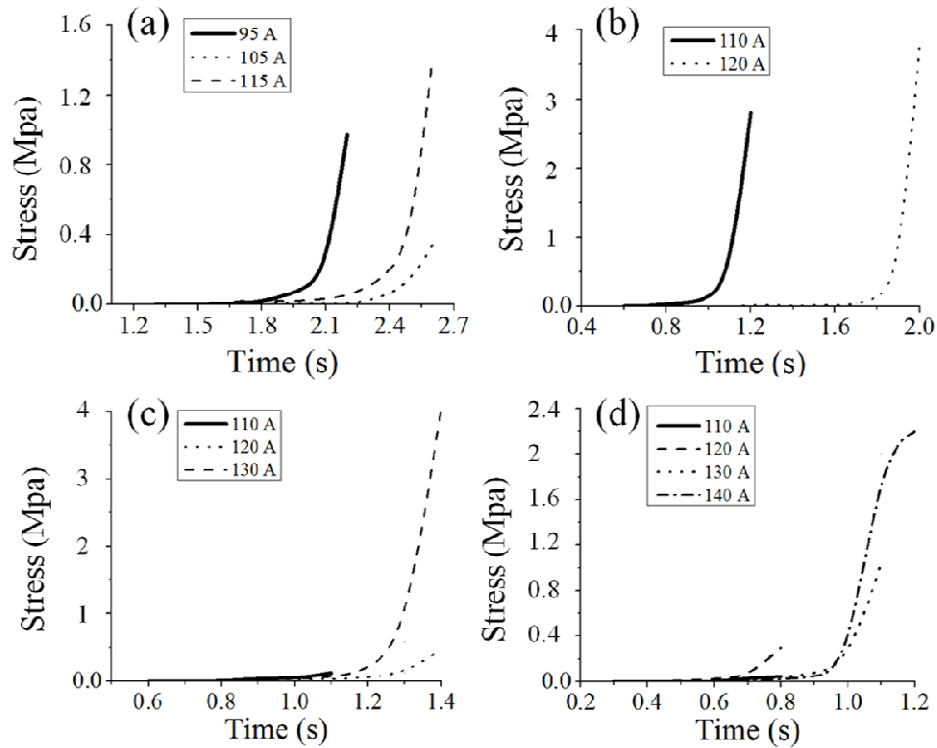


Fig. 5.10 The calculated average tensile stress for various welding currents at welding speeds of: (a) 2 mm/s; (b) 3mm/s; (c) 4 mm/s; (d) 5 mm/s.

welding speed to 3 and 4 mm/s. However, this ascending behaviour in tensile stress does not continue over higher welding velocities. As shown in Fig 5.10d, the maximum average tensile stress drops at a welding speed of 5 mm/s. In other words, the results show that the maximum average tensile stress is highest at a medium range of welding velocity. This result can be explained through the interaction between two main parameters that control the material flow within the base metal: 1) solidification shrinkage causing material flow within the base metal since larger welds are accompanied by more lateral solidification contraction and consequently bigger driving forces for the materials flow, and 2) the amount of resistance against material flow that strongly depends on the temperature of the base metal since colder base metals are accompanied by higher elastic moduli and larger yield strengths. High temperature conditions soften the base metal and lower the amount of resistance. As a result of Newton's third law of motion, cold base metals and large welds generate higher

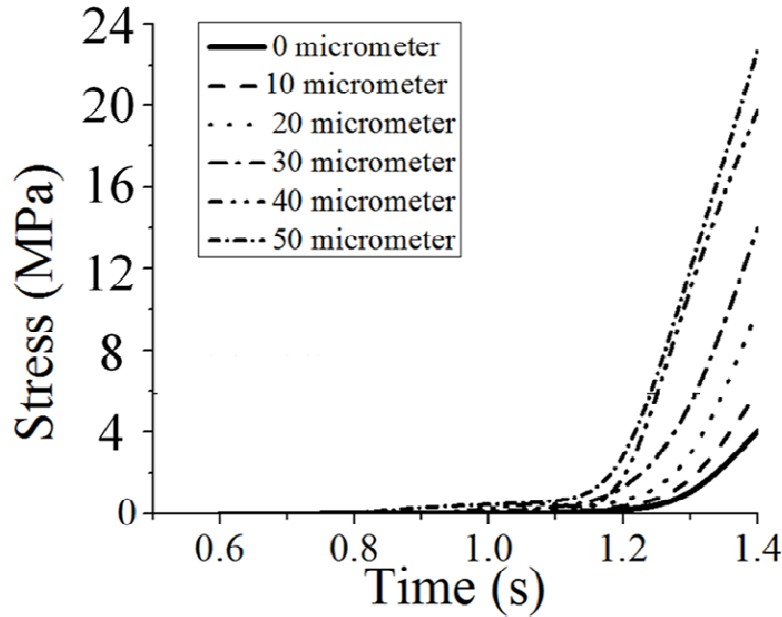


Fig. 5.11 The average tensile stresses on the weld fusion surface under different constraining conditions.

magnitudes of reaction forces, while hot base metals and smaller welds create reaction forces of lower magnitude. Therefore, the small average tensile stresses observed at low welding speeds can be linked to the excessive softness of the base metal that stems from high temperature conditions during slow welding. By increasing the welding speed, the heat input decreases leading to a colder base metal. As a result, the reaction forces and consequently the average tensile stress deforming the semisolid weld increase. Although the base metal is coldest at high welding velocities, the reaction forces do not keep growing since there is a significant drop in the size of the weld. In this simulation, by increasing the welding speed from 4 mm/s to 5 m/s at a constant welding current of 120 A, the depth of weld penetration decreased from 2 mm to 1 mm. It is hypothesized that very small welds do not generate enough linear solidification contraction to maintain the ascending trend of the reaction forces.

Another welding parameter that is well known to affect the susceptibility of the weld to hot cracking is the constraining condition of the weld [7]. Hence, the developed model is also utilized to investigate how welding constraints change the external force field deforming the

semisolid weld. To do so, six different constraining conditions were simulated by applying different Dirichlet boundary conditions to the back surface of the plate welded by a welding speed of 3mm/s and a welding current of 120 A. In the first, the back surface of the plate was clamped ($\bar{U}_0 = 0$). In the remaining five tests, the back surface was displaced in tension along the Y direction a value of 10, 20, 30, 50 or 100 μm . The displacement was initiated at the time corresponding to the time that at least one of the bar elements within the semisolid weld had percolated, and reached the maximum value when the weld had fully solidified. The obtained average tensile stresses are shown in Fig. 5.11. As shown in Fig. 5.11, applying constraining tensile deformations to the plate during welding drastically increases the average tensile stress acting on the weld mushy zone.

5.2.2.2 Global deformation rate

Using the technique discussed in section 4.3.2.1, the average lateral tensile stress acting on the weld mushy zone can be translated into the average lateral tensile strain rate, *i.e.* the global strain rate $\dot{\epsilon}$. The variation in $\dot{\epsilon}$ with time is shown in Fig. 5.12 for different welding procedures. Note that for these simulations, the simulated plate is clamped during welding. Note also that the welding time of zero corresponds to the time at which the weld pool begins to solidify.

As can be seen in the figure, the lateral deformation of the mushy zone induced by the external force field occurs primarily at later times, corresponding to the last stages of solidification. The rapid rise in $\dot{\epsilon}$ at later times is due to the coalescence effect. However, near the end of welding, the rigidity of the semisolid weld increases since coalescence has largely occurred and thus the growth rate of $\dot{\epsilon}$ decreases. If the external stress field is not strong enough, $\dot{\epsilon}$ will drop at the very end of the solidification. As an example, this can be seen in Fig. 5.12c in the case with a welding current of 110 A. These model estimates of external deformations can also be compared against experimental data, at least to a qualitative level. In a prior set of studies, Coniglio and Cross [72] used an extensometer located across the weld root to measure the evolving thermomechanical strain rate across the weld mushy zone during welding.

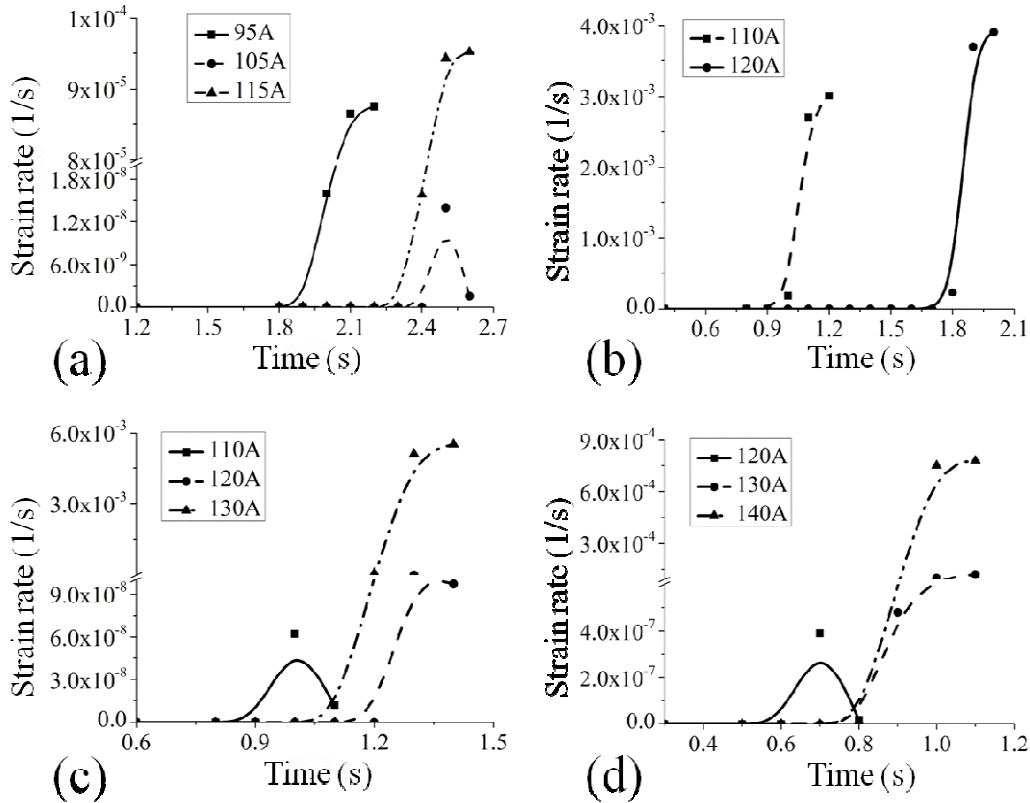


Fig. 5.12 The calculated global strain rate for various welding currents at welding speeds of: (a) 2 mm/s; (b) 3mm/s; (c) 4 mm/s; (d) 5 mm/s.

For welding speed of 4 mm/s and welding current of 130A, this measured thermomechanical strain rate for AA6061 was reported to rise from 0 to 0.01 s^{-1} from the start to end of welding. The estimates made by the thermomechanical model for the same welding conditions show an increase from 0 to 0.0058 s^{-1} over the same period. Considering all the assumptions made in the model, the similarity in the two values is exceptional. Comparing the different curves of Fig. 5.12, it can be seen that an increase in the welding current leads to an increase in $\dot{\epsilon}$. This observation can be linked to the fact that higher welding currents amplify the lateral component of the external tensile stress acting on the mushy zone (see Fig. 5.10).

5.2.2.3 Partitioning to individual micro liquid channels

In this model, the obtained global strain rates are translated into global deformation rates using Eq. (4.24). Through Eq. (4.28), the model then calculates the external normal deformation rate of each micro liquid channel based on the variation in the global deformation rate with time. Fig. 5.13 shows the external normal deformation rate of the micro liquid channels within the reconstructed mushy zone of a weld for two different average solid fractions, 0.66 and 0.92. The weld corresponds to a welding velocity of 4 mm/s and a welding current of 120 A under a restraining strain rate of 0.1 s^{-1} . As can be seen in the figure, the external normal deformation rate is very low near the fusion boundary, indicating that the channel walls in this region do not separate too much due to the external forces. This observation can be linked to dendrite coherency since the micro liquid channels near the fusion boundary have higher solid fractions as compared to the center of the weld and therefore experience coherency earlier in the welding process. Thus, the walls of these bridged channels become interlocked and therefore cannot separate from each other, forming an unaffected region in the vicinity of the fusion boundary. A comparison of Figs. 5.13a and b reveals that this unaffected region grows towards the center of the mushy zone, as expected, since an increase in the average solid fraction must also lead to an increase in the number of bridged channels.

As is well known, the choice of welding parameters affects the quality of a weld, inducing porosity, hot cracking, etc., depending on the choice of variables. Figs. 5.14a, b, and c illustrate the effect of welding parameters on the average external normal deformation rate of the mushy zone, $\bar{\delta}_{z,ext}$, for three different values of $\dot{\epsilon}_{re}$. Arithmetic averaging similar to Eq. (5.2) is used to calculate $\bar{\delta}_{z,ext}$. Note that the bridged channels are not considered in averaging the external normal deformation rate of the micro liquid channels since they do not participate in deformation.

A comparison of Figs. 5.14a, b, and c indicates that welding parameters do not affect the $\bar{\delta}_{z,ext}$ of a self-restrained mushy zone ($\dot{\epsilon}_{re} = 0$) and an externally-restrained mushy zone ($\dot{\epsilon}_{re} \neq 0$) in the same way. This difference in behaviour can be understood by examining the

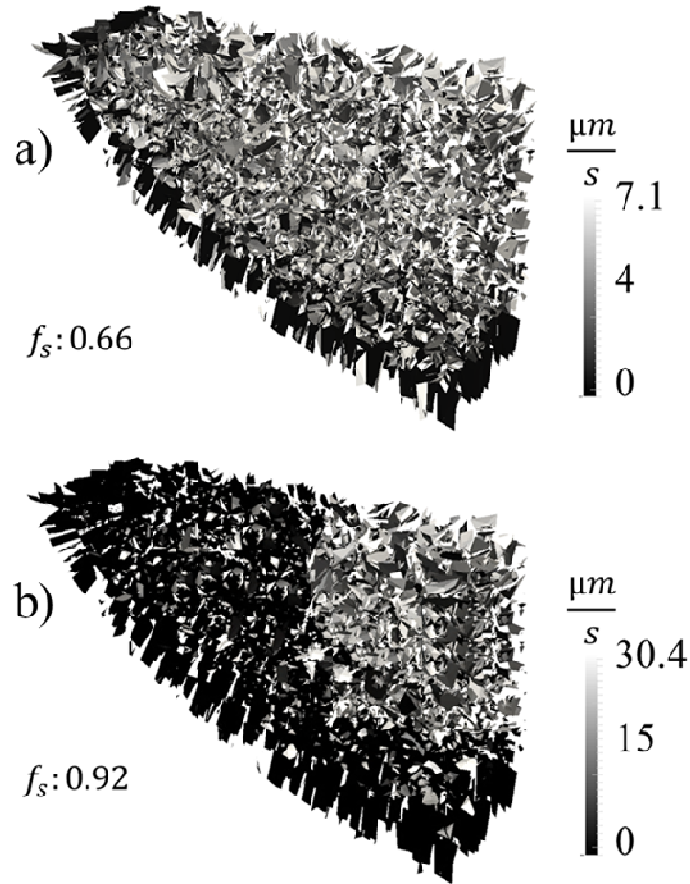


Fig. 5.13 The external normal deformation rate of the micro liquid channels within the reconstructed mushy zone of a weld for (a) an average solid fraction of 0.66 and (b) an average solid fraction of 0.92. The weld is fabricated by a welding velocity of 4 mm/s and a welding current of 120 A and under a restraining strain rate of 0.1 s^{-1} .

mechanisms by which welding parameters affect the external normal deformation rate of the channels. For the self-restrained mushy zone shown in Fig. 5.14a, welding parameters strongly affect both $\dot{\epsilon}_{th}$, and also the mushy zone morphology since different welding parameters generate different microstructures [7]. As can be seen in Figure 5.14a, a welding travel speed of 4 mm/s accompanied by a welding current of 130 A yields the maximum $\bar{\delta}_{z,ext}$. However, for the externally-restrained mushy zones shown in Figs. 5.14b and c, $\dot{\epsilon}_{re}$ becomes the dominant source of deformation as compared to $\dot{\epsilon}_{th}$ and therefore the change in

the mushy zone morphology is the only mechanism by which welding parameters noticeably affect the average external normal deformation rate.

In terms of the weld microstructure and the mushy zone morphology, welding conditions that lead to finer grains reduce the external normal deformation rate. This is because weld microstructures with smaller grains have more micro liquid channels. Based on Eq. (4.28), the global deformation rate is then partitioned amongst more micro liquid channels, resulting in a decrease in the external normal deformation rate in any individual channel. As can be seen in Fig. 5.14, the largest $\bar{\delta}_{z,ext}$ for externally-restrained mushy zones occurs for a welding travel speed of 2 mm/s and a welding current of 95 A. The weld microstructure contained a low number of micro liquid channels as compared to all other simulations.

As Figs. 5.13 and 5.14 show, the external normal deformation rate of the micro liquid channels increases significantly with an increase in the average solid fraction. In other word, the micro liquid channels near the solidus surface have higher external normal deformation rates. As the average solid fraction rises, more liquid channels meet the dendrite coherency criterion and consequently the number of unbridged channels decreases. This is because, through Eq. (4.28), the transformation of unbridged micro liquid channels into the bridged ones as fraction solid increases lowers N_u . Consequently, the deformation of the mushy zone localizes over a few micro liquid channels.

Although the deformation module is not intended to predict the formation of hot cracks, it can however explain the formation of centerline cracks [7] that very commonly occur as part of hot cracking. As shown above, the micro liquid channels at the center of the weld have the greatest internal and external normal deformation rates. Therefore, based on the micro-scale models of hot cracking [12, 99, 100], the centerline of the weld will be highly susceptible to the formation of hot cracks. The model also shows that welding parameters can affect the deformation rate of the channels and consequently impact the degree of the hot crack susceptibility of welds.

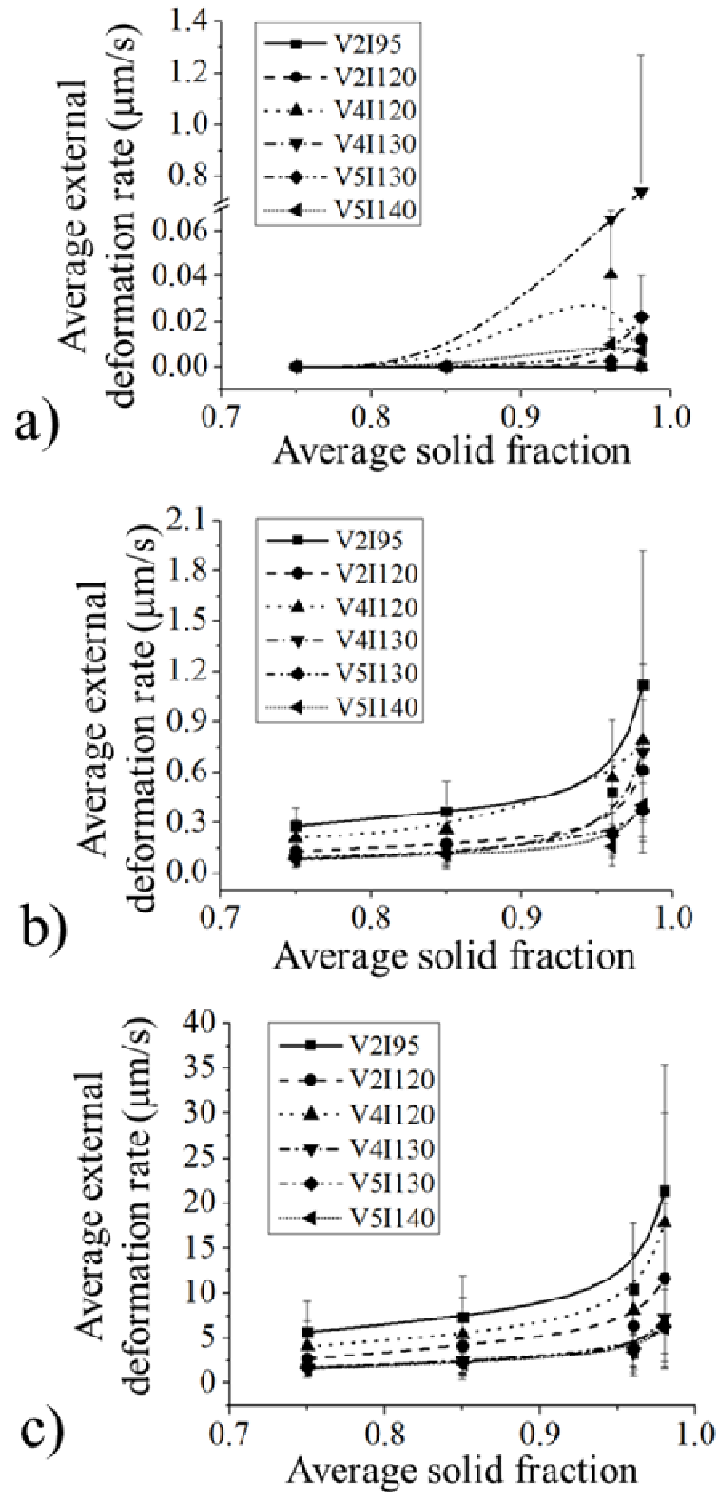


Fig. 5.14 The effect of various welding parameters on the average external normal deformation rate of the mushy zone for three different restraining strain rates: (a) 0 s^{-1} , (b) 0.005 s^{-1} , and (c) 0.1 s^{-1} .

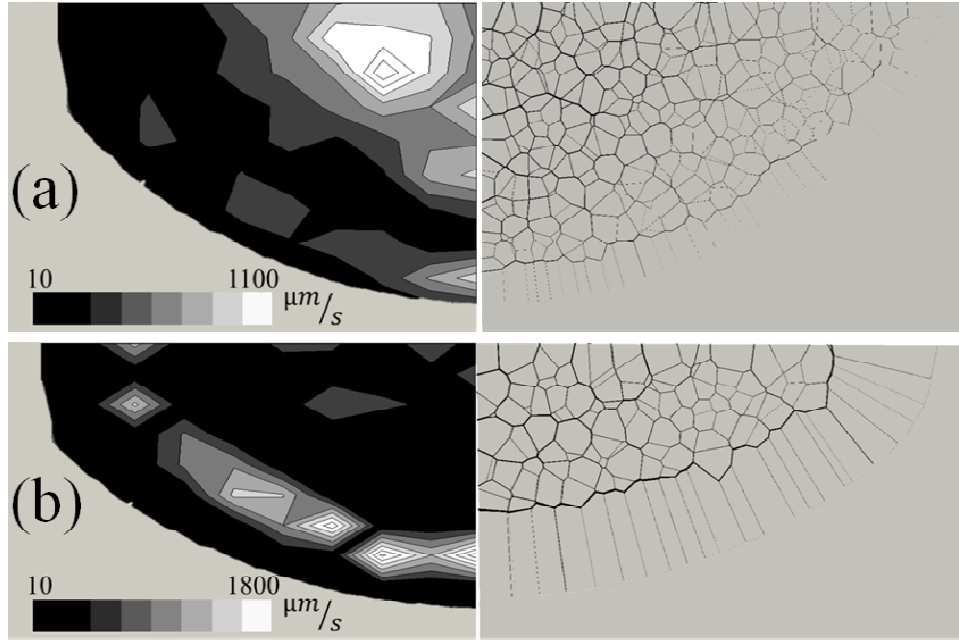


Fig. 5.15 Cross-sectional distribution of the magnitude of the fluid velocity vector at an average solid fraction of 0.85 for a weld fabricated on a clamped plate with a welding velocity of 5 mm/s and a welding current of 140 A; (a) average columnar length of 250 μm ; (b) average columnar length of 800 μm . The contours on the left show the distribution of the magnitude of the fluid velocity, while the images on the right show their corresponding microstructure.

5.3 Fluid flow

As discussed in section 4.4, a two-step technique is applied to solve the system of equations for fluid flow (Eq. (4.34)) across the entire mushy zone of the weld. First, the fluid velocity field is calculated. Using the obtained velocity field as the boundary condition, the pressure field within the network of micro liquid channels is then simulated.

Fig. 5.15 shows the cross-sectional distribution of the magnitude of the fluid velocity vectors, *i.e.* $\|\vec{q}\|$, for two different welding conditions at the same average solid fraction of 0.85. The semisolid weld shown in Fig. 5.15a corresponds to a weld fabricated on a clamped plate using a welding current of 140 A and a welding velocity of 5 mm/s. The semisolid weld shown in Fig. 5.15b belongs to a weld fabricated by the same welding parameters, but with longer columnar grains, simulating the weld microstructure manipulation techniques discussed in chapter 4. As shown in Fig. 5.15, the model indicates that the fluid velocity is

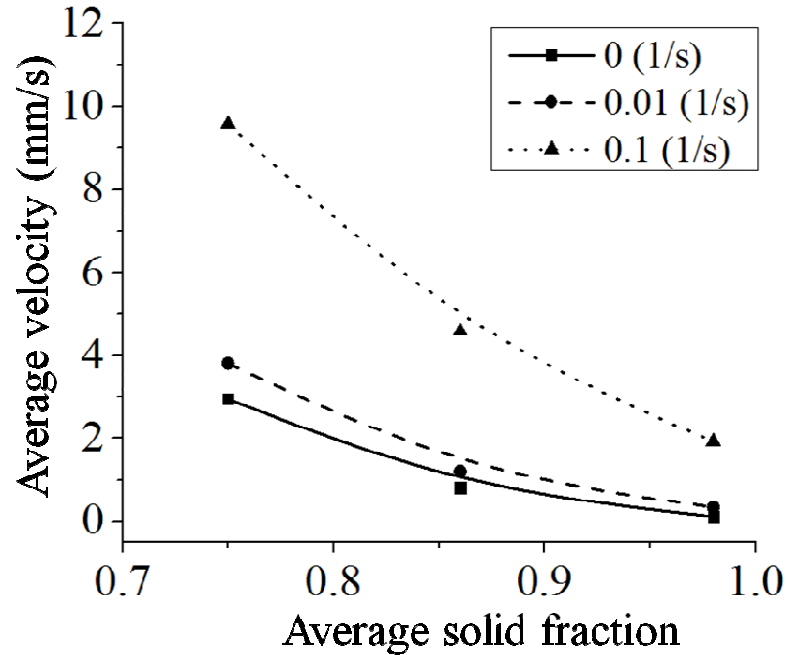


Fig. 5.16 The variation in the average fluid velocity versus average solid fraction for a weld fabricated by a welding current of 140 A and a welding speed of 5 mm/s under three different external lateral tensile strain rates.

not uniform across the cross-section of the weld mushy zone. Specifically, Fig. 5.15a shows that the fluid velocity experiences severe localization near the center of the weld. This can be associated with the localization of deformation rate inside the weld mushy zone. As discussed in section 5.2, the micro liquid channels located near the centre of the weld experience higher internal and external deformation rates during welding. Based on Eq. (4.34), this amplifies the load vector and consequently induces higher fluid velocities to compensate for the faster separation of the wall channels near the centre of the weld.

A comparison between Fig. 5.15a and Fig. 5.15b shows that longer columnar grains intensify the localization of fluid flow within the columnar region of the weld. This observation can be explained through the fact that a longer columnar region generates a wider liquid film separating the columnar grains from the equiaxed grains (see section 5.1). Such a wide liquid film can transfer higher volumes of molten metal towards the columnar grains, increasing the volumetric feeding rate for the micro liquid channels inside the columnar zone.

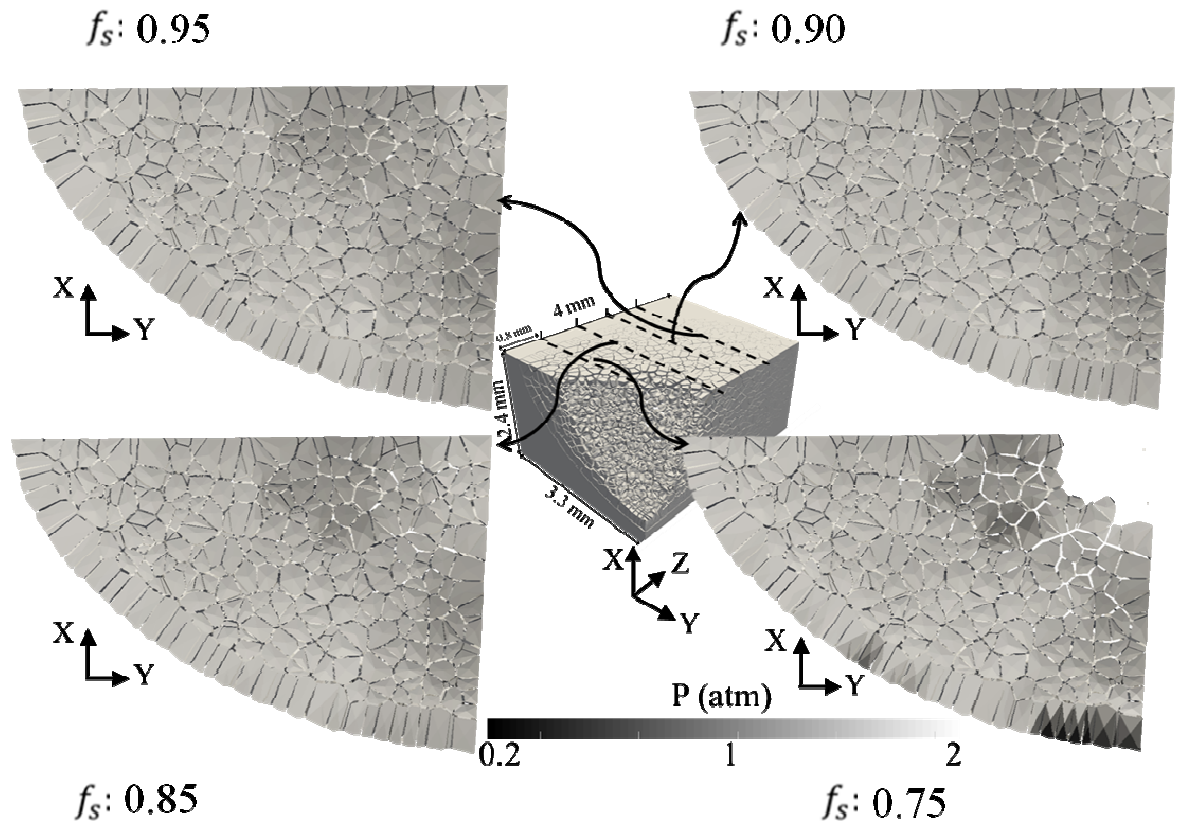


Fig. 5.17 Cross-sectional distribution of pressure at different average solid fractions for a semisolid weld fabricated at a welding speed of 4 mm/s and a welding current of 120 A.

Due to conservation of mass, higher inlet volumetric flow rates induce higher fluid velocities inside the columnar region. The results of the model demonstrate that the solid fraction also impacts the fluid velocity within the weld mushy zone. In order to investigate the effects of the solid fraction on the fluid velocity field, the average fluid velocity, *i.e.* the arithmetic average of the magnitude of the fluid velocity vectors, is calculated for different average solid fractions along the weld mushy zone. The variation in the average fluid velocity versus average solid fraction for a weld fabricated by a welding current of 140 A and a welding speed of 5 mm/s is shown in Fig. 5.16. The results indicate that the average fluid velocity decreases near the fully solidified end of the weld mushy zone. This observation can be linked to a stopping force induced by the closed end of the mushy zone. The fully solidified end causes a force acting in the opposite direction of the fluid flow, inducing deceleration in

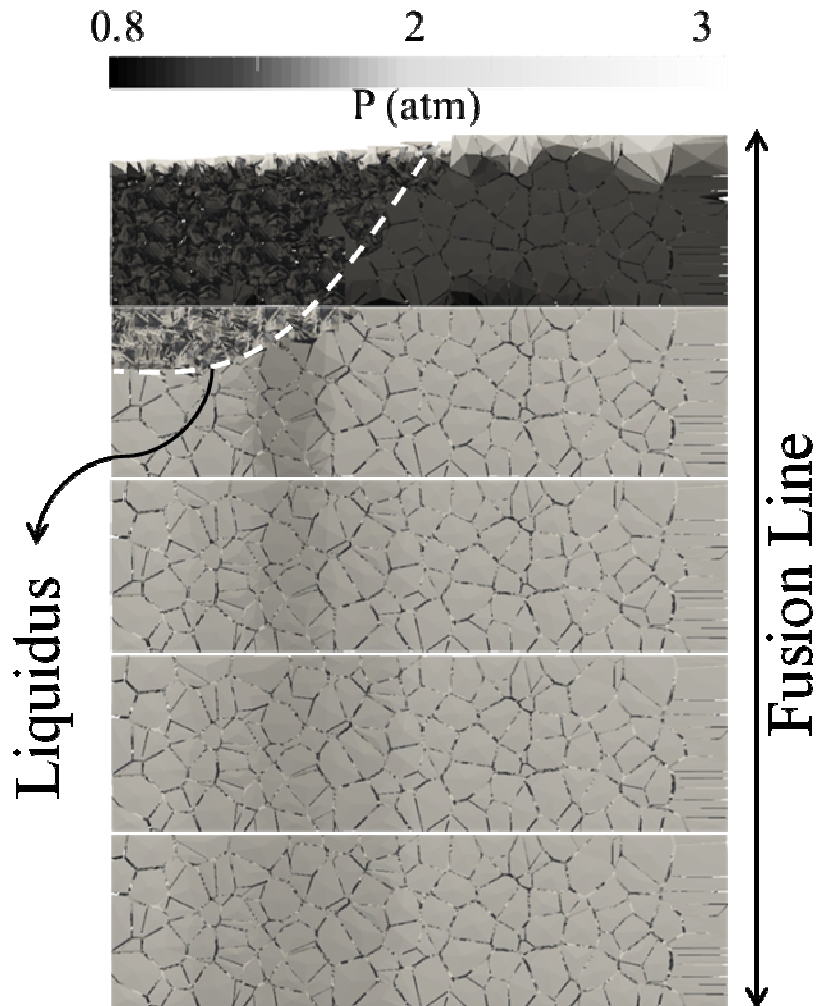


Fig. 5.18 The localization of pressure drop along the mushy zone is shown from the top view of the weld mushy zone.

fluid flow through the mushy zone. Fig. 5.16 also shows that welding constraints significantly impact the fluid velocity field. The model shows that increasing the external lateral tensile strain rate acting on the plate raises the fluid velocity through the weld mushy zone. As discussed in section 5.2, higher external strain rates increase the external deformation rates inside the micro liquid channels. Based on Eq. (4.34), larger deformation rates within the weld mushy zone demand faster flows in order to compensate for the semisolid deformation.

After simulating the fluid velocity field, the pressure field within the mushy zone is calculated. Fig. 5.17 illustrates the cross-sectional distribution of pressure at different average solid fractions for a semisolid weld fabricated at a welding speed of 4 mm/s and a welding current of 120 A. For the sake of illustration, the solid grains are coloured with respect to the pressure values of their neighbour channels. The results show that the pressure field is not uniform through the network of micro liquid channels. Specifically, the channels near the centre of the weld have the lowest pressure values. The localization of pressure drop along the mushy zone is shown from a different angle in Fig. 5.18, where a low pressure trail near the weld centre can be observed in the top view of the weld mushy zone. According to Darcy's law [139], two major factors affect the pressure drop within a porous medium: 1) the velocity of the fluid flowing through the medium, and 2) the permeability of the porous medium. In general, a porous medium with higher fluid velocity and lower permeability requires a larger driving force and therefore induce higher pressure drops across the medium. Therefore, the localization of pressure drop at the centre of the weld can be associated with the higher fluid velocities in this region (see Fig. 5.15).

In order to investigate the variation of the pressure field along the weld mushy zone, the average pressure, *i.e.* the arithmetic average of the nodal pressure values, is calculated for different average solid fractions along the weld mushy zone. The results for a clamped plate welded at six different sets of welding parameters are shown in Fig. 5.19. These curves show that the average pressure initially decreases to a minimum value near the average solid fraction of 0.8. This initial pressure drop along the weld mushy zone can be linked to variation of permeability. For a semisolid structure, the permeability is strongly influenced by the width of the channels and therefore solid fraction, where wider channels at lower solid fractions have higher permeability [12]. Therefore, as the average solid fraction behind the weld pool rises from 0 to 0.8 and hence the permeability of the weld mushy zone decreases, the average pressure inside the weld mushy zone drops in order to provide the required driving force and maintain a relatively fast fluid flow in that region. This pressure drop however does not extend to the regions with high solid fractions near the fully solidified end of the weld mushy zone. As shown in Fig. 5.19, the average pressure has an ascending characteristic at high average solid fractions.

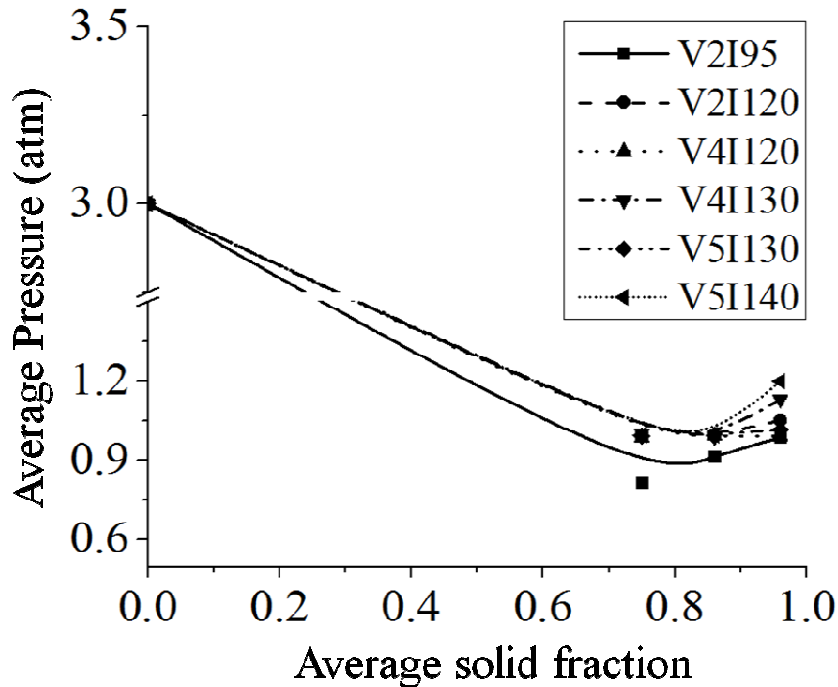


Fig. 5.19 The variation of the average pressure as a function of average solid fraction for a clamped weld with various welding parameters.

This phenomenon can be associated with the severe decrease in the fluid velocity near the fully solidified end of the mushy zone (see Fig. 5.16). This increase in pressure creates the stopping force that decelerates the fluid flow within the weld mushy zone.

As shown in Fig. 5.19, welding parameters slightly affect the pressure field. The model indicates that a weld fabricated by a welding speed of 2 mm/s and a welding current of 95 A has the smallest minimum average pressure value inside the weld mushy zone. This prediction can be explained through the microstructure of the weld where V2I95 has a long columnar zone (the normalized length of the columnar zone is 0.65). As discussed earlier, larger columnar grains intensify the fluid velocity through the columnar zone, inducing larger pressure drops.

The model also shows that welding constraints impact the pressure field. Fig. 5.20 illustrates the variation in the average pressure along the weld mushy zone for four different external lateral tensile strain rates. The weld is fabricated at a welding current of 120A and a welding

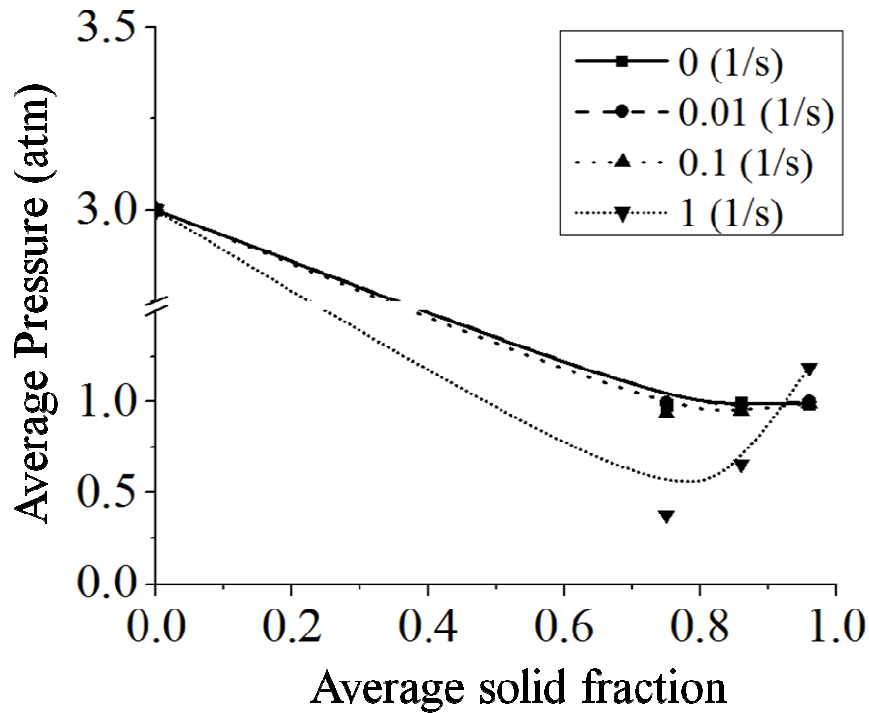


Fig. 5.20 The variation in the average pressure along the weld mushy zone for four different external lateral tensile strain rates. The weld is fabricated at a welding current of 120A and a welding speed of 4 mm/s.

speed of 4 mm/s. Based on the obtained results, increasing the external strain rate from 0 to 0.1 s^{-1} slightly amplifies the pressure drop inside the weld mushy zone. This correlation becomes more significant once the external strain rate exceeds 0.1 s^{-1} . The model shows that external strain rates greater than 0.1 s^{-1} considerably lower the minimum average pressure within the weld mushy zone. This phenomenon can be linked to the effects of welding constraints on the fluid velocity field. As Fig. 5.16 shows, increasing the external lateral tensile strain rate beyond 0.1 s^{-1} significantly raises the average fluid velocity through the weld mushy zone, inducing larger pressure drops.

For a clamped weld, the results of the model show that the pressure drop between the weld pool and high average solid fraction regions at the end of the weld mushy zone is nearly 2 atm (Fig. 5.19). This result is fairly close to the pressure drop range calculated by Coniglio and Cross in GTA welding of clamped aluminum plates [72]. Using the RDG model, they

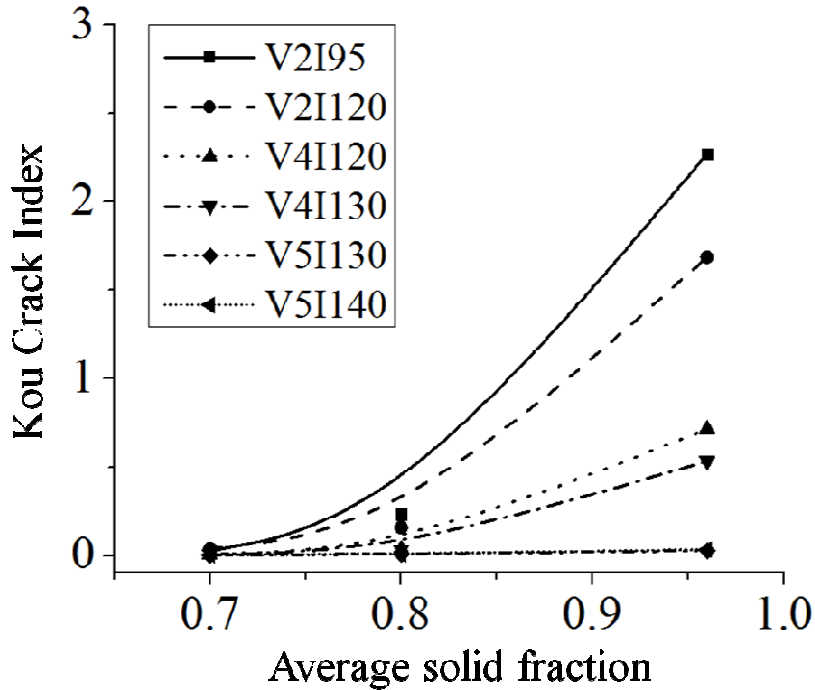


Fig. 5.21 The Kou crack index for different RVE's with different average solid fractions along the weld mushy zone. The welds are fabricated on a plate under an external lateral tensile strain rate of 0.1 s^{-1} with six different sets of welding parameters.

have reported that the pressure drop between the aluminum weld pool and the end of the mushy zone with a solid fraction of 0.98 varies in the range of 0.11 and 0.55 atm.

5.4 Defect formation

As discussed in section 4.5, three different defect formation models and consequently three defect indices are used in this work to investigate the formation of hot cracks and hydrogen porosity inside the RVEs with different average solid fractions along the weld mushy zone. Specifically, hot cracking is studied through the Kou crack and the atmosphere-induced rupture indices, while the hydrogen porosity index indicates the susceptibility of the weld to the formation of hydrogen porosity. Note that the term defect index refers to the ratio of defected channels to the total number of channels, as defined in Eq. (4.40). Note also that the overall accumulation of defects is not considered in this analysis in order to obtain a better understanding regarding the role of the different regions along the weld mushy zone on the

formation of defects, *i.e.* the phenomenon of localization. In other words, the defected channels formed in the early stages of solidification within the RVEs with low average solid fractions are not transferred to RVEs with high average solid fractions at later stages of solidification. Hence, the defect indices calculated in this section only account for the new defected channels formed within the RVE and not the defects transferred from one time to the next. Also, the RVEs with solid fractions smaller than 0.7 are not considered since it is assumed that the healing phenomenon occurs, and does not allow defects to survive in these areas of the mushy zone.

5.4.1 Hot cracking

In order to investigate the formation of hot cracks through the Kou's model, Eq. (4.40) is used to calculate the Kou crack index for different RVE's with different average solid fractions along the weld mushy zone. The results for six welds fabricated on a plate under an external lateral tensile strain rate of 0.1 s^{-1} with different sets of welding parameters are shown in Fig. 5.21. This figure indicates that the areas with higher average solid fractions near the fully solidified end of the weld mushy zone are the most susceptible regions to hot cracking, whereas the zones closer to the weld pool have a negligible contribution to the formation of hot cracks.

As discussed in section 4.5.1, the Kou cracking criterion suggests that a conjunction of slow fluid flow and fast deformation induces hot cracking. This can explain the obtained results regarding the variation of hot cracking susceptibility across the weld mushy zone. The relatively fast fluid flow within the RVEs occurring at low average solid fractions (Fig. 5.16) can accommodate for the deformation of the semisolid structure and hence limits the occurrence of hot cracking to a few channels. As Fig. 5.22 illustrates, the defected channels formed at low average solid fractions are mainly located inside the columnar zone where the micro liquid channels experience high deformation rates (see section 5.2). However, upon approaching the fully solidified end of the weld mushy zone, the fluid velocity significantly decreases (Fig. 5.16), while the external deformation rate inside the channels increases (Fig. 5.13). This causes a noticeable increase in the Kou crack index. The model shows that the cracks forming at high average solid fractions are mainly located within the equiaxed region and near the weld centre (Fig. 5.22). Such a shift from the columnar zone to the centre of the

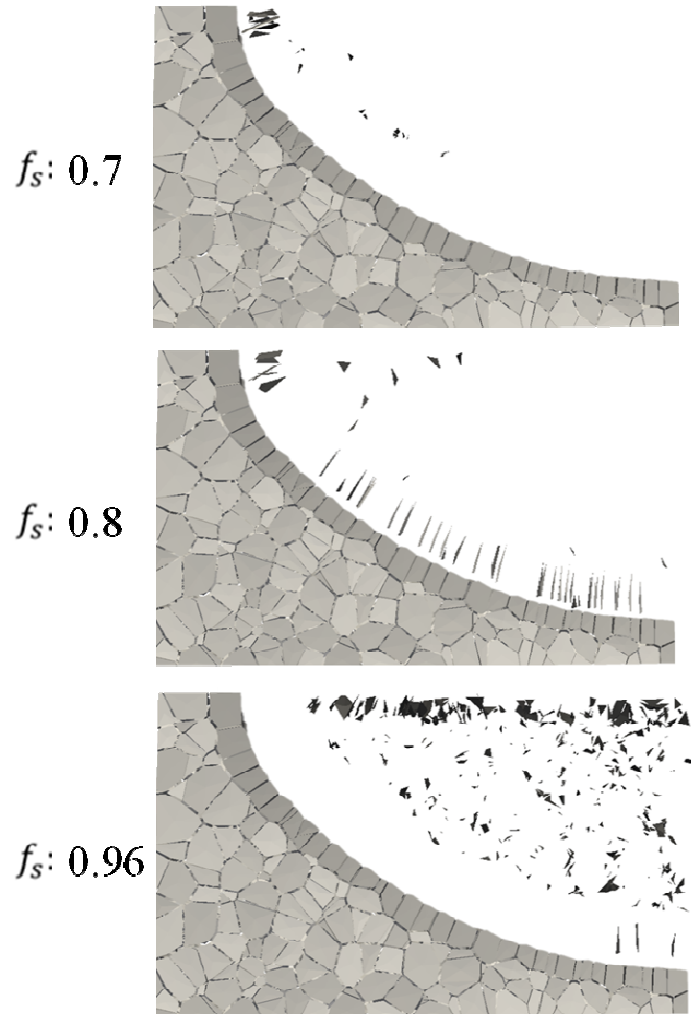


Fig. 5.22 The distribution of new defected channels at three different average solid fractions based on the Kou cracking criterion. The weld is fabricated on a plate under an external lateral tensile strain rate of 0.1 s^{-1} with a welding speed of 2 mm/s and a welding current of 120 A .

weld can be linked to the fact that the deformation inside the weld mushy zone localizes at the centre of the weld since that is the last region to solidify (see section 5.2). The results shown in Fig. 5.21 also reveal the role of welding parameters and specifically the role of welding speed on the formation of hot cracks. The model shows that increasing the welding travel speed lowers the susceptibility of the mushy zone to hot cracking defined by Kou's criterion. This can be associated with the impact of welding travel speed on the cooling rate inside the weld mushy zone, where faster travel speeds increase the cooling rate (Fig. 5.8). At higher cooling rates, the micro liquid channels bridge faster, lowering the number of open

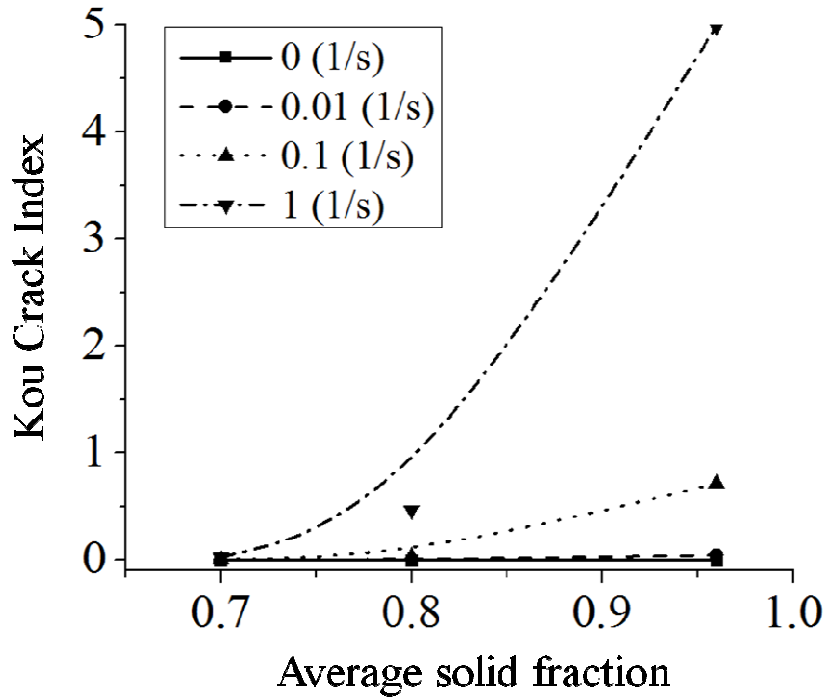


Fig. 5.23 The variation of the Kou crack index along the mushy zone of a weld fabricated at a welding speed of 4 mm/s and a welding current of 120 A under various external lateral tensile strain rates.

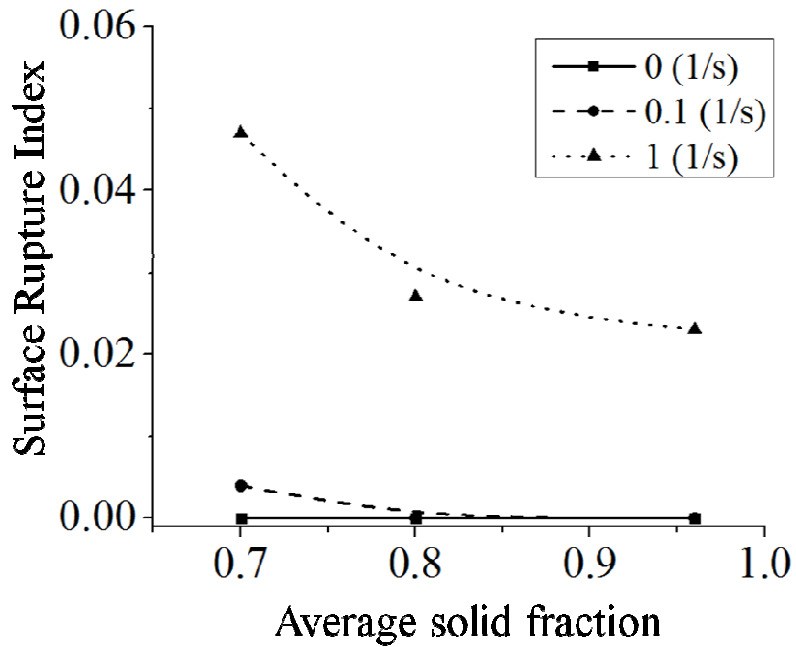


Fig. 5.24 The variation of the surface rupture index along the mushy zone of a weld fabricated at a welding speed of 4 mm/s and a welding current of 120 A under various external lateral tensile strain rates.

channels capable of developing defects at high average solid fractions where accumulated deformation and slow fluid velocities can cause cracking.

The model shows that the external lateral tensile strain rate strongly affects the formation of hot cracks. As shown in Fig. 5.23, increasing the external strain rate raises the Kou crack index. This effect becomes significant for strain rates above 0.1 s^{-1} , allowing one to take this value as the critical strain rate for the formation of hot cracks. The observed correlation between external strain rate and the formation of hot cracks is linked to the direct role of external strain rate in the deformation rate of the micro liquid channels. As discussed in section 5.2 and shown in Fig. 5.14, higher external strain rates increase the deformation rate inside the micro liquid channel, making the weld mushy zone more susceptible to hot cracking.

Besides the Kou crack index, the atmosphere-induced surface rupture criterion discussed in section 4.5 is used to define another index, *i.e.* surface rupture index, to study hot cracking. Unlike the Kou criterion, the surface rupture model directly accounts for the local pressure values inside the micro liquid channels, where smaller pressure values increase the susceptibility of the weld mushy zone. Similar to the Kou crack index, the surface rupture index is calculated for different RVEs with various average solid fractions along the weld mushy zone. The weld is assumed to be fabricated at a welding speed of 4 mm/s and a welding current of 120 A under three different external lateral tensile strain rates. The results shown in Fig. 5.24 indicate that the areas with an average solid fraction close to 0.8 are more prone to surface rupture than the zones close to the fully solidified end of the mushy zone. This observation is linked to the distribution of pressure across the mushy zone. As discussed in section 5.3, the minimum average pressure value occurs within the RVEs with an average solid fraction around 0.8. Therefore, the local liquid pressure inside the surface channels in this zone may not be high enough to resist against the propagation of liquid-atmosphere interface into the weld mushy zone. By approaching the fully solidified end of the mushy zone, the local pressure values increase (Fig. 5.19), lowering the surface rupture index.

Figs. 5.24 and 5.25 also reveal the role of the external strain rate in the formation of surface cracks. Based on the obtained results, external lateral tensile strain rates smaller than 0.1 s^{-1} barely induce surface cracks. By increasing the external strain rate value beyond 0.1 s^{-1} , the

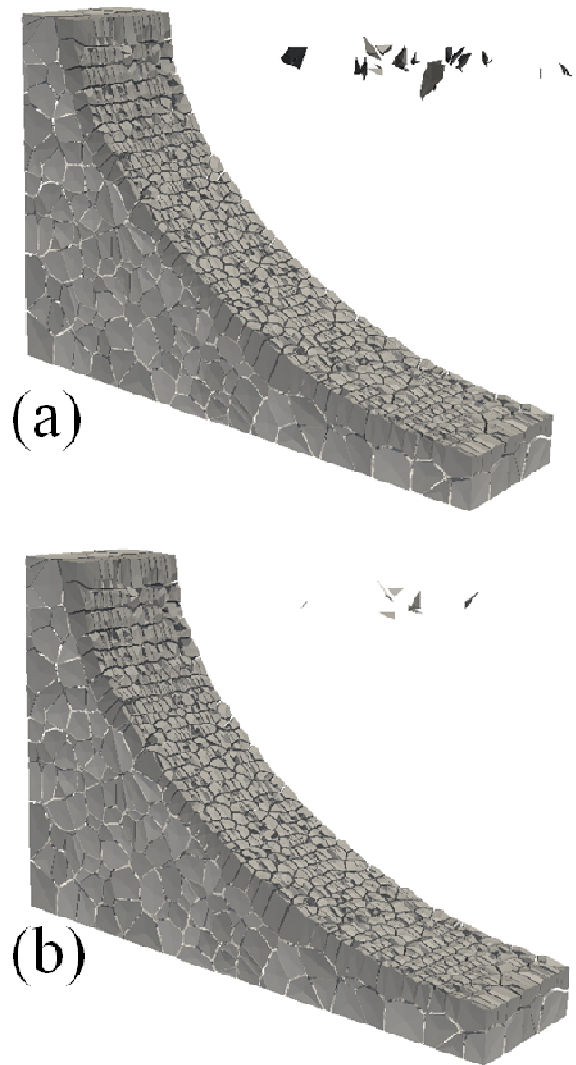


Fig. 5.25 The distribution of surface cracks inside a RVE with average solid fraction of 0.7 for a weld fabricated at a welding speed of 4 mm/s and a welding current of 120 A. (a) external strain rate of 0.1 s^{-1} ; (b) external strain rate of 1 s^{-1} .

surface rupture index significantly increases. This can be associated with the impact of the external strain rate on the pressure field inside the weld mushy zone (Fig. 5.20), where strain rate values greater than 0.1 s^{-1} noticeably amplify the pressure drop. As shown in Fig. 5.25, the model predicts that the surface cracks occur at the centre of the weld. The localization of surface cracks at the centre of the weld can be explained through the characteristics of the

pressure field. As discussed in section 5.3, the areas near the centre of the weld mushy zone have the lowest pressure values, raising the risk of surface rupture.

The results of the model regarding the formation of hot cracks are quite close to the outcomes of several experimental studies. First, the model can be used to explain that why hot cracks are often reported to occur at the centre of the weld [7]. Second, the estimated critical external strain rate, *i.e.* 0.1 s^{-1} , is close to the values reported in the literature. Arata et al. [76] have reported a critical strain rate value of 0.25 s^{-1} for hot cracking in arc welding of Al-Mg-Si alloys. Cross et al. [60] have also shown that the critical strain rate for hot cracking in welding of aluminum alloys does not exceed 5 s^{-1} . In addition, the experimental studies by Coniglio and Cross [72] show that the critical external strain rate for hot cracking during GTA welding of aluminum alloys varies in the range of 0.05 s^{-1} and 0.3 s^{-1} . Third, the predictions of the model regarding the effect of welding travel speed on the formation of hot cracks can be verified by several experimental studies. Matsuda et al. [77] have reported that, in aluminum alloys, increasing the travel speed from 2.5 mm/s to 13 mm/s during GTAW can improve the hot cracking resistance. Furthermore, experimental investigations by Chihoski [70, 80] showed that at high welding travel speeds, a compressive stress field forms near the mushy zone, preventing hot cracking. Niel et al. [84] showed that for a constant welding current in GTAW, increasing the welding travel speed can prevent hot cracking in welding of AA 6061 aluminum alloys. Finally, similar to the outcomes of the model, welding experiments show that shortening the columnar zone through grain size manipulation techniques can reduce hot cracking. In separate studies, Mousavi et al. [73], Warrington et al. [74], and Dvornak et al. [21] each demonstrated that a reduction in aluminum alloy hot crack susceptibility could be achieved through the addition of grain refiners.

5.4.2 Hydrogen Porosity

Following the technique discussed in section 4.5.2, the hydrogen porosity index is calculated for different RVEs with different average solid fractions along the weld mushy zone. In this technique, the pressure field plays a direct role, where small local pressure values and large hydrogen partial pressure values inside the micro liquid channels increase the susceptibility of the mushy zone to the formation of porosity.

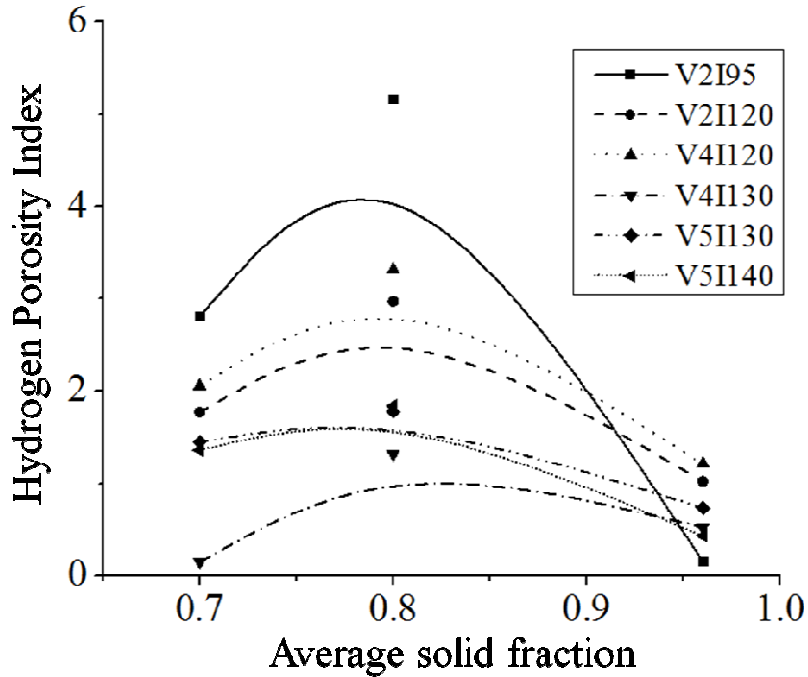


Fig. 5.26 The hydrogen porosity index for different RVE's with different average solid fractions along the weld mushy zone. The welds are fabricated on a clamped plate with six different sets of welding parameters. The initial hydrogen content is assumed to be 2 (ml/100gr).

As shown in Fig. 5.26, for an initial hydrogen content of 2 ml/100gr, the hydrogen porosity index rises to a maximum value at the average solid fraction of 0.8, and then drops to lower values at higher average solid fractions near the fully solidified end of the weld mushy zone. This behaviour can be linked to the variation of two terms along the weld mushy zone: 1) the term $P_H - P_l$ that is the difference between the hydrogen partial pressure value and the local liquid pressure value inside a channel, and 2) the term $\frac{2\gamma}{r}$ which is a function of the width of the channel. Based on Eq. (2.4), a channel experiences the formation of porosity once the pressure difference, *i.e.* $P_H - P_l$, inside the channel exceeds $\frac{2\gamma}{r}$. At low average solid fractions near the weld pool, although $\frac{2\gamma}{r}$ is relatively small, the hydrogen partial pressure is too low inside the majority of the micro liquid channels to induce hydrogen porosity. Therefore, only a few channels with small liquid pressure values see the formation of porosity. As Fig. 5.27 shows, these channels are mainly located inside the columnar zone where the pressure drop is more intense.

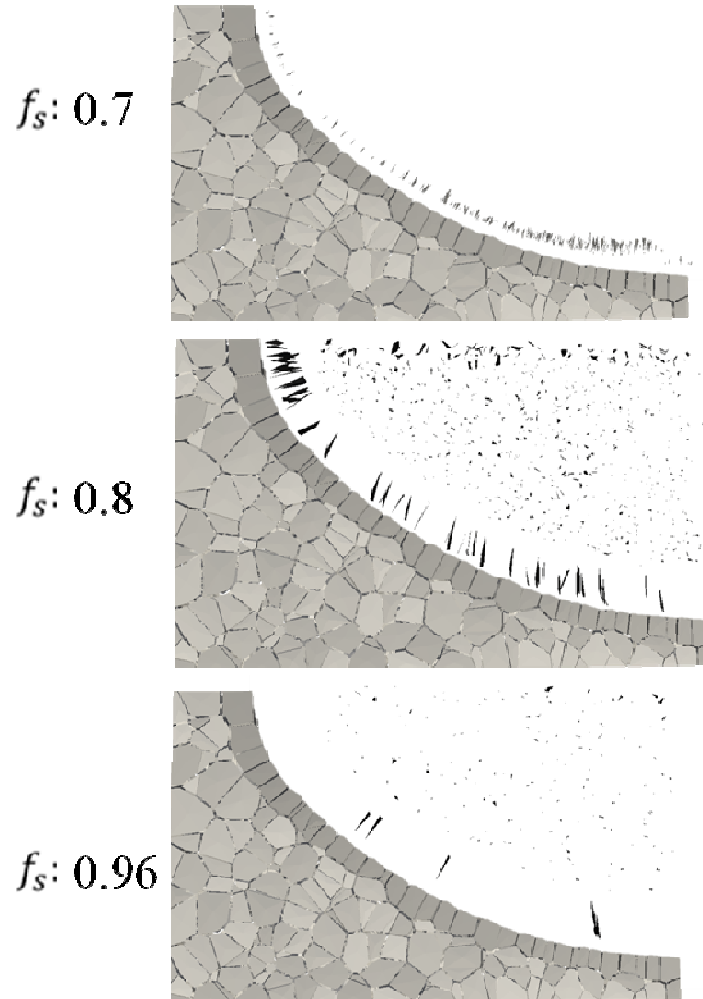


Fig. 5.27 The distribution of new defected channels due to hydrogen porosity at three different average solid fractions. The weld is fabricated on a clamped plate with a welding speed of 2 mm/s and a welding current of 120 A. The initial hydrogen content is assumed to be 2 (ml/100gr).

As the average solid fraction increases, the hydrogen content inside the micro liquid channels rises (Lever law, Eq. (4.45)). According to Sivert's law (Eq. (4.43)), higher hydrogen contents consequently increase the partial pressure of hydrogen inside the micro liquid channels, raising the susceptibility of the mushy zone to the formation of porosity. The hydrogen porosity index increases to a maximum value at an average solid fraction of 0.8, where the average liquid pressure is minimum (see Fig. 5.19). As Fig. 5.27 shows, the distribution of hydrogen porosity in this area is more uniform. For average solid fractions greater than 0.8, although the hydrogen partial pressure continues to grow, the channels

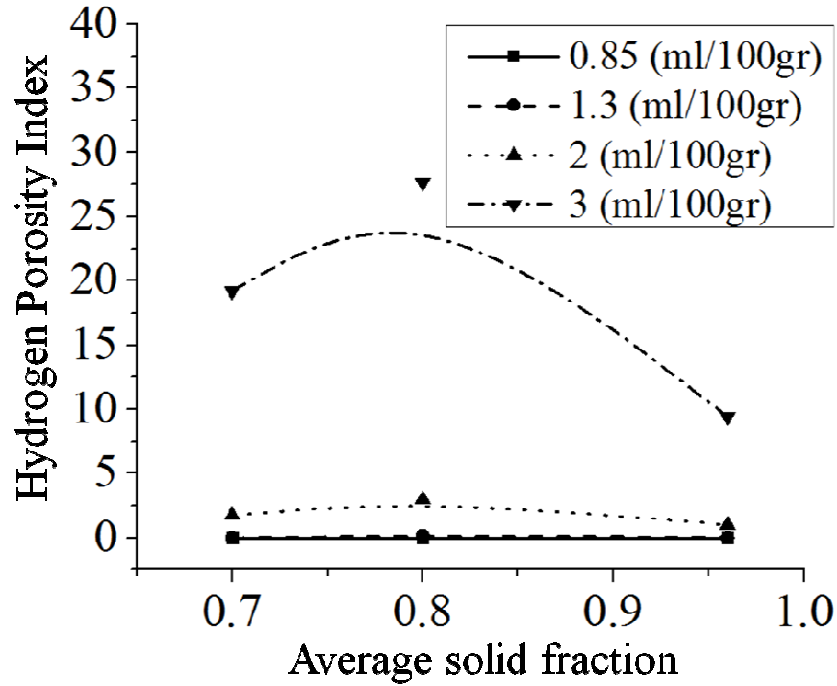


Fig. 5.28 The variation of the hydrogen porosity index along the weld mushy zone for different initial hydrogen contents. The weld is fabricated on a clamped plate with a welding speed of 4 mm/s and a welding current of 120 A.

become very narrow and therefore $\frac{2\gamma}{r}$ drastically increases, lowering the hydrogen porosity index. This reduction in hydrogen porosity is more noticeable inside the columnar zone where the channels are much narrower (Fig. 5.27).

Fig. 5.26 shows that welding parameters impact the hydrogen porosity index. Based on the obtained results, the mushy zone of a weld fabricated at a welding speed of 2 mm/s and a welding current of 95A has the highest level of susceptibility to the formation of hydrogen porosity. This can be associated with the role of welding parameters in the characteristics of the pressure field. As discussed in section 5.3, various welding parameters lead to different pressure fields within the weld mushy zone. Fig. 5.19 shows that the minimum average pressure value occurs in the case study of V2I95. Therefore, one can conclude that the local pressure values are the lowest for this mushy zone, raising $P_H - P_l$ inside the micro liquid channels and consequently leading to a maximum hydrogen porosity index.

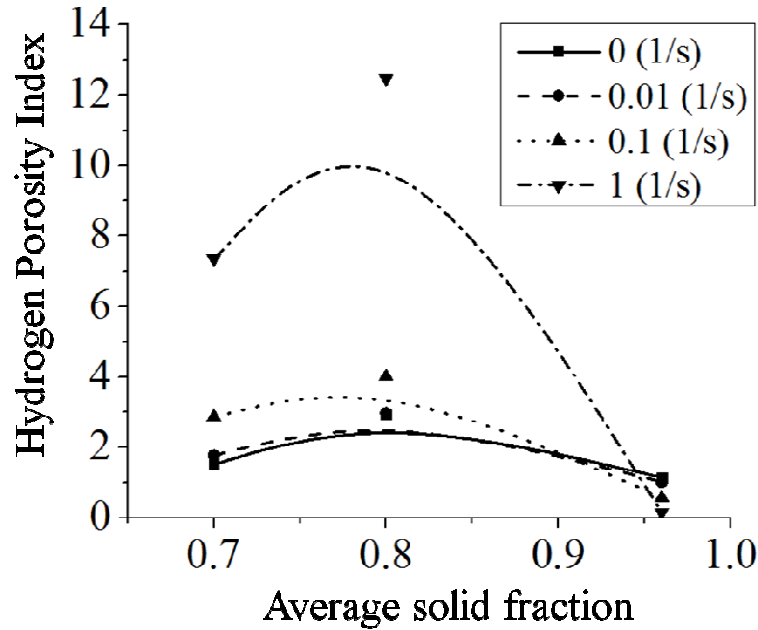


Fig. 5.29 The variation of the hydrogen porosity index along the weld mushy zone for various external lateral tensile strain rates. The weld is fabricated at a welding speed of 4 mm/s and a welding current of 120 A. The initial hydrogen content is assumed to be 2 ml/100gr.

The results indicate that the initial hydrogen content dissolved in the weld pool also affects the hydrogen porosity index. Fig. 5.28 illustrates the variation of the hydrogen porosity index along the weld mushy zone for different initial hydrogen contents. The weld is fabricated on a clamped plate with a welding speed of 4 mm/s and a welding current of 120 A. The model shows that the hydrogen porosity index for initial hydrogen contents less than 1.3 ml/100gr is almost negligible. By increasing the initial hydrogen content, the weld mushy zone becomes more susceptible to the formation of hydrogen porosity. The results shown in Fig. 5.28 indicate a critical hydrogen content between 2 and 3 ml/100gr above which the hydrogen porosity index drastically increases. The effect of the initial hydrogen content on the formation of hydrogen porosity can be explained through Eq. (4.43), where higher initial hydrogen contents lead to higher hydrogen partial pressure values.

As shown in Fig. 5.29, the model also predicts that the external strain rate affects the formation of hydrogen porosity. This figure illustrates the variation of the hydrogen porosity index along the weld mushy zone for various external lateral tensile strain rates. The weld is

fabricated at a welding speed of 4 mm/s and a welding current of 120 A. The initial hydrogen content is assumed to be 2 ml/100gr. Similar to hot cracking, the model shows a critical strain rate between 0.1 and 1 s⁻¹ above which the weld mushy zone becomes significantly susceptible to the formation of hydrogen porosity. This observation can be linked to the large pressure drops inside the weld mushy zone induced by high external strain rates (Fig. 5.20).

The results discussed above match fairly well to the experimental studies on the formation of hydrogen porosity in welding. Several investigations [7, 140] show a direct link between the initial content of hydrogen and the amount of pores inside the weld. Coniglio et al. [72] have reported a critical hydrogen content of 1.00 ml/100gr for the formation of porosity during welding of AA6061. This value is close to the critical range predicted by the model, *i.e.* 2 to 3 ml/100gr. Also, Devletian et al. have shown that low welding velocity can increase the amount of hydrogen porosity [140], similar to the results given by the model.

Finally, the the 3D X-ray tomography images taken from the weld samples can be used to qualitatively assess the results of the model regarding the role of welding parameters on the formation of hydrogen porosity. Unfortunately, these images cannot be used to conduct a quantitative analysis because: 1) very small pores may be missed due to the limited resolution of the X-ray tomography machine, 2) it is not clear if the observed pores inside the weld are formed within the micro liquid channels or are hydrogen bubbles inside the weld pool that are trapped during solidification, and 3) the initial hydrogen content inside the weld pool is unknown. However, as discussed in section 4.6.3, since similar welding conditions (except for welding speed and welding current) that are applied during the fabrication of welding samples as similar to the welding simulations, the X-ray tomography images can be used for comparison purposes.

Figs. 5.30-5.32 depict the X-ray tomography images of three different weld samples. A comparison between these images indicate that a weld fabricated by a welding speed of 2 mm/s and a welding current of 95 A has the highest amount of pores. Also, the images show that increasing welding speed lowers the amount of pores. However, they do not reveal a significant difference between the susceptibility of the weld samples fabricated at higher welding speeds (Figs. 5.31, and 5.32). These observations verify the predictions of the model shown in Fig. 5.26.

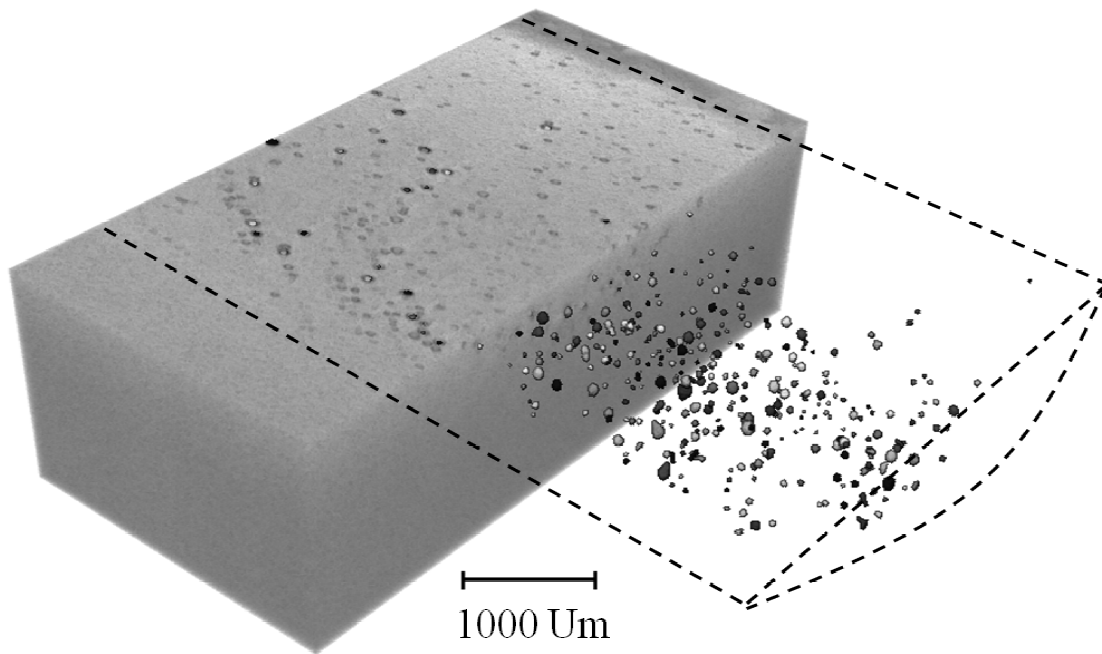


Fig. 5.30 X-ray tomography image of a weld fabricated on a clamped plate at a welding speed of 2 mm/s and a welding current of 95 A.

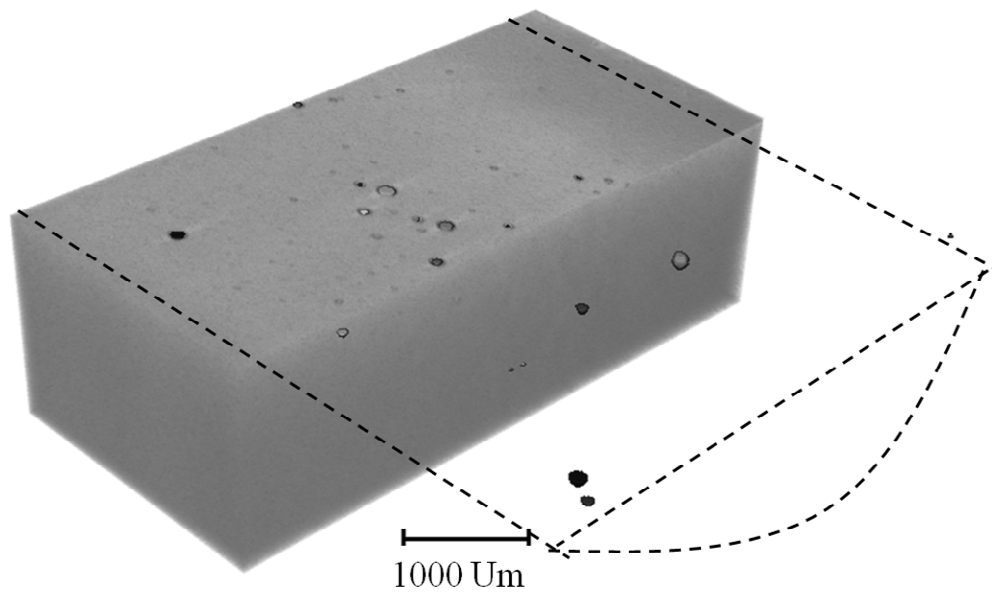


Fig. 5.31 X-ray tomography image of a weld fabricated on a clamped plate at a welding speed of 4 mm/s and a welding current of 120 A.

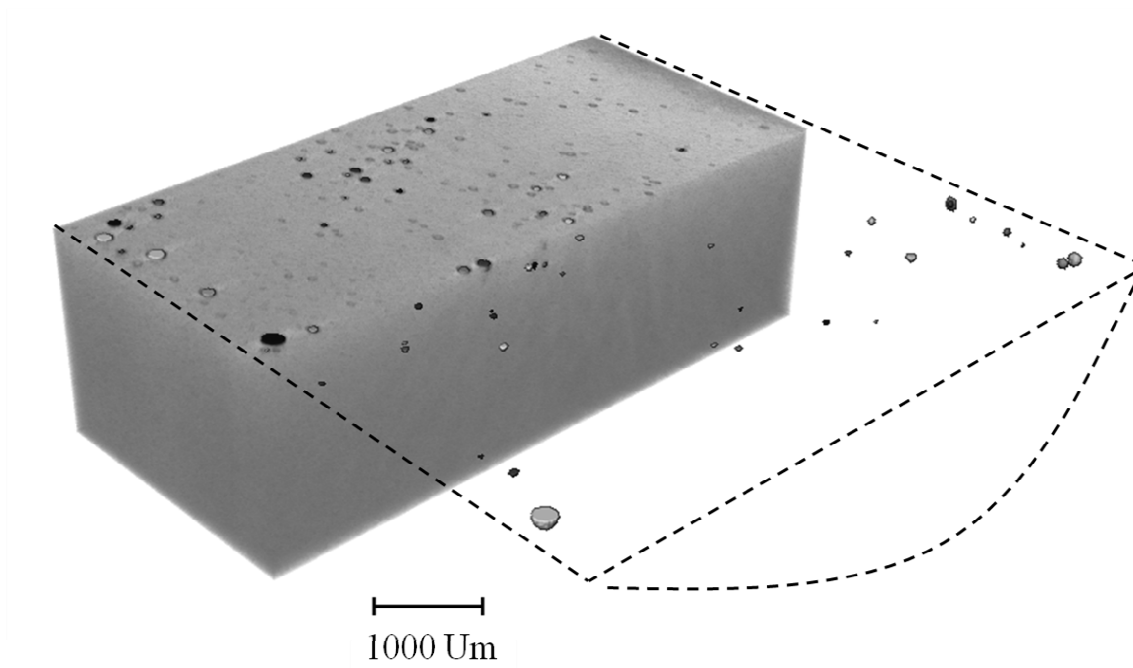


Fig. 5.32 X-ray tomography image of a weld fabricated on a clamped plate at a welding speed of 5 mm/s and a welding current of 140 A.

6 Conclusions

6.1 Conclusion

The key conclusions of this study are:

- A 3D meso-scale solidification model simulating fusion welding of aluminum – magnesium – silicon alloys has been developed that directly models the evolving semisolid microstructure composed of micro liquid channels and solidifying grains on a relatively large domain. By coupling modified Voronoi diagrams with experimental data, the simulation accurately estimates the shape and size of the weld pool. The results demonstrate that mushy zone features strongly depend on welding parameters, and quantifies the effects of welding procedure on both the macrostructure and also the evolving solidification microstructure. The model demonstrates that the ability of the mushy zone to feed molten metal into the solidifying areas is not uniform throughout the weld as the micro liquid channels between the columnar zone and equiaxed fusion zone provide the best feeding.
- The developed model couples the meso-scale solidification model of welding with a thermomechanical model of the base metal in order to investigate deformation within the semisolid weld as a function of welding parameters. The model considers solidification contractions as well as the temperature-dependent stress response of the base metal during welding to yield the force field acting on the fusion surface of the aluminum alloy AA6061 during tungsten inert gas welding. Based on the obtained results, for a plate 3 mm in thickness, the semisolid weld experiences the maximum deformations at a moderate welding speed of 4 mm/s and a high level of welding current. The results also suggest that any external tensile stress during welding will amplify the deformation of the semisolid weld.
- The normal separation rate of the walls of the micro liquid channels induced by both solidification shrinkage and external forces are predicted as a function of welding conditions. Also, this model is able to simulate the variation of the deformation rate through the weld mushy zone. This can be used to locate the areas inside the weld that are more prone to solidification cracking. From the simulations, four main

conclusions can be made: (1) Welding parameters (travel speed and current) strongly influence the internal deformation rates of the micro liquid channels induced by solidification shrinkage. The model suggests that increasing the welding travel speed increases the internal deformation rate of the weld mushy zone. Also, it is shown that lower welding currents at a constant welding travel speed increase the internal deformation rate of the mushy zone and therefore can induce solidification cracking. (2) Welding conditions also impact the external deformation rate of the weld mushy zone induced by external forces and thermo-mechanical stresses. The model shows that in an externally restrained welding condition, the external force is the dominant factor where larger forces cause higher external deformation rates. For self-restrained welding conditions in which the external force is eliminated, the model suggests that higher welding speeds increase the external deformation rate and can cause solidification cracking. (3) The internal normal deformation rate due to solidification shrinkage and also the external normal deformation rate caused by external forces are both highest for the micro liquid channels at the center of the mushy zone. This phenomenon explains the common occurrence of solidification cracks at the center of the weld. (4) The internal normal deformation rate of the micro liquid channels induced by solidification shrinkage increases near the weld pool where the solid fraction is low, whereas the external normal deformation rate caused by external forces is the lowest in this area.

- The model shows that the pressure field inside the weld mushy zone is non-uniform. Specifically, the pressure values inside the channels at the centre of the weld are lower than the pressure values within the channels adjacent to the fusion surface. The model also predicts that the average pressure decreases to a minimum value near the fully solidified end of the weld mushy zone at an average solid fraction of 0.8. The results demonstrate that welding parameters associated with longer columnar zones induce larger pressure drops. In addition, the model indicates that external lateral tensile strain rates greater than 0.1 s^{-1} significantly lower the pressure values inside the weld mushy zone.
- The formation of cracks and hydrogen porosity during welding is simulated through three different micro-scale models. The results show that various regions across the

weld mushy zone have different levels of susceptibility to the formation of solidification defects. The model also indicates that welding conditions impact the susceptibility of the weld. Specifically, the model predicts that higher welding speeds lower the risk of solidification defects. Also, the results show that external lateral tensile strain rates greater than 0.1 s^{-1} can drastically increase the number of defects inside the weld mushy zone.

6.2 Model limitations

Similar to any other model, the developed model is accompanied with several limitations caused by simplifying assumptions. The main limitations of this model are:

- This modelling approach does not consider the dendritic morphology of grains but instead assumes that the solidification envelope defines the solid-liquid boundary. This assumption restricts the capability of the model to assessing only the meso-scale feeding ability of the mushy zone through analysis of the width of the intergranular micro liquid channels, while ignoring the interdendritic micro liquid channels. Although this is a strong assumption, it matches the geometrical features of the micro liquid channels defined by the micro-scale models of solidification cracking, and therefore will benefit the studies on developing the multi-scale models of solidification cracking based on the existing micro-scale models.
- Despite the fact that the growth angle of the columnar grains in the weld microstructure varies with welding parameters, the model assumes that the columnar grains always grow normal to the fusion surface.
- The model does not account for curved columnar grains and assumes that these grains have straight edges.
- The columnar-to-equiaxed transition does not occur naturally within the model but instead is imposed by the placement of the grain nuclei.
- In order to calculate the transient force field acting on the weld mushy zone, the model assumes that the weld remains intact. This can induce errors if the external force is large enough to tear the mushy zone.

- Although the modified partitioning technique used to distribute the global external deformation rate among the micro liquid channels has improved the existing partitioning methods, it does not yet include the role of the solid grains. In addition, this model assumes that each micro liquid channels equally contribute to the global deformation rate. Although the ability of the micro liquid channels to accommodate strain correlates with the width of the channels, where the channel walls can separate more easily in wider channels, this effect is only significant at lower average solid fractions where the semisolid weld contains a wide range of channels with different widths and therefore different capabilities to contribute to semisolid deformation. As this model focuses on solidification cracks, which occur at high average solid fraction, the application of this partitioning technique is appropriate.
- Only the lateral component of the global external deformation rate is considered, *i.e.* the effects of the other components are ignored.
- The model geometry, specifically, the parallel micro liquid channel walls, does not exactly match welding microstructure since in reality the grain boundaries are not parallel to each other during solidification. This is a strong assumption, however, it has been successfully used in previous applications of granular models of solidification to investigate new phenomena related to solidification cracking during casting processes. If the channels walls are not assumed to be parallel, then it is not possible to determine the external deformation rate vector. Further, the solidification velocity vector $(\vec{v}_1^*, \vec{v}_2^*)$, resulting in the internal deformation rate vector, would have to be defined through two separate terms, *i.e.* βv_1^* and βv_2^* , rather than a single parameter ($\delta_{z,int}^i = \beta(v_1^* + v_2^*)$).
- Unlike real semisolids in which solid grains have smooth surfaces with rounded corners, the grain edges within the reconstructed mushy zone are sharp due to using the Voronoi tessellation algorithm. These sharp edges do not allow the model to form large liquid pockets at grain triple joints and therefore for a given micro channel width, the model overestimates the solid fraction. The overestimation of the solid fraction will induce a premature drop in the number of micro liquid channels, potentially leading to an artificial rise in the external deformation rate.

- The model assumes that the formation of defects does not affect fluid flow. Kuzentsov and Vafai [137] have shown that neglecting the influence of defect formation on fluid flow analysis in semisolids leads to deviations from the actual pressure field.
- This model assumes that the healing of hot cracks and/or porosity does not occur. This assumption compromises the accuracy of the model predictions when the average solid fraction is low since in this state the liquid can easily circulate through the channels.

6.3 Outlook of future use

The current model is able to simulate the key transient physical phenomena during welding that cannot be studied through experimental techniques. For example, one can use the model to explain the evolution of a transient force field on the fusion surface that deforms the weld mushy zone. In another example, the model can be used to determine the deformation rate, fluid velocity, and liquid pressure inside every single micro liquid channel of the weld mushy zone as a function of welding parameters. In addition, this model can qualitatively predict the susceptibility of the weld to hot cracking. Specifically, the model can be used to assess the role of welding velocity and welding current in the formation of solidification defects in TIG welding of aluminum 6061.

In the future, the application of this model could be extended to other materials, welding technologies and also other failure mechanisms. One could update the current modules in order to apply this model to TIG welding of other materials. This would allow engineers to estimate a safe range of welding parameters for welding of new materials. Further, the current model could be modified in order to be exploited in other fusion welding technologies such as laser welding. Also, the same techniques could be used to simulate liquation cracking inside the heat affected zone of the weld. This would enable the engineer to assess the susceptibility of different materials to liquation cracking during welding as a function of welding parameters, and therefore to optimize welding procedures.

Bibliography

- [1] Kaufman, J. G., "Properties of aluminum alloys: tensile, creep, and fatigue data at high and low temperatures", ASM international, Ohio, 1999.
- [2] Kaufman, J. G., Elwin, L. R., "Aluminum alloy castings", American Foundry Society, Columbus, Ohio, 2004.
- [3] ASM Metals Handbook, Vol. 2, "Properties and selection of nonferrous alloys and special purpose materials", ASM International, 1990.
- [4] Welding Handbook, Vol. 1, American Welding Society, Miami, 1976, pp. 2-32.
- [5] Schwartz, M. M., "Metals joining manual", McGraw-Hill, New York, 1979, pp. 1-40.
- [6] Esmaeili, A., Besharati Givi, M. K., Zareie Rajani, H. R., "A metallurgical and mechanical study on dissimilar Friction Stir welding of aluminum 1050 to brass (CuZn30)", *Materials Science and Engineering: A*, 528.22 (2011): 7093-7102.
- [7] Kou, S., "Welding metallurgy", John Wiley & Sons Inc., Hoboken, New Jersey, 2003.
- [8] Davies, G. J., Garland, J. G., "Solidification structures and properties of fusion welds.", *International Metallurgical Reviews* 20.1 (1975): 83-108.
- [9] Liming, L., Gang, S., Guoli, L., Jifeng, W., " Pore formation during hybrid laser-tungsten inert gas arc welding of magnesium alloy AZ31B-mechanism and remedy ", *Materials Science and Engineering A* 390 (2005): 76-80.
- [10] Ren pei, L., Zu jue, D., Yong ming, P., " Solidification crack susceptibility of aluminum weld metals ", *Transactions of Nonferrous Metals Society of China* 16 (2006): 110-116.
- [11] Sistaninia, M., Phillion, A. B., Drezet, J. M., Rappaz, M., "A 3-D coupled hydromechanical granular model for simulating the constitutive behavior of metallic alloys during solidification", *Acta Materialia* 60.19 (2012): 6793-6803.

[12] Sistaninia, M., Phillion, A. B., Drezet, J. M., Rappaz, M., "Three-dimensional granular model of semi-solid metallic alloys undergoing solidification: Fluid flow and localization of feeding", *Acta Materialia* 60.9 (2012): 3902-3911.

[13] Kou, S., Le., Y., "Grain structure and solidification cracking in oscillated arc welds of 5052 aluminum alloy", *Metallurgical Transactions A*, 16.7 (1985): 1345-1352.

[14] Vernède, S., Jarry, P., Rappaz, M., "A granular model of equiaxed mushy zones: Formation of a coherent solid and localization of feeding", *Acta materialia* 54.15 (2006): 4023-4034.

[15] Fujii, H., Nogi, K., Aoki, Y., Umatoshi, H., " Bubble formation in aluminum alloy during electron beam welding ", *Journal of materials Processing Technology* 155 (2004): 155-156, 1252-1255.

[16] DuPont, J. N., Robino, C. V., Marder, A. R., " Solidification and weldability of superalloys", *Welding Journal* 77 (1998): 417s.

[17] DuPont, J. N., Robino, C. V., Marder, A. R., Notis, M. R., Michael, J. R., "Solidification of Nb-bearing superalloys: Part I. Reaction sequences.", *Metallurgical and Materials Transactions A* 29.11 (1998): 2785-2796.

[18] DuPont, J. N., Robino, C. V., Marder, A. R., "Modeling solute redistribution and microstructural development in fusion welds of Nb-bearing superalloys", *Acta Materialia* 46.13 (1998): 4781-4790.

[19] Singer, A. R. E., Jennings, P. H., " Hot-shortness of some aluminium-iron- silicon alloys of high purity ", *Journal of The Institute of Metals* 73 (1947): 273-284.

[20] Nakata, K., Matsuda, F., "Evaluations of ductility characteristics and cracking susceptibility of Al alloys during welding (Materials, Metallurgy & Weldability)", *Transactions of JWRI* 24.1 (1995): 83-94.

[21] Dvornak, M. J., Frost, R. H., Olson, D. L., "The weldability and grain refinement of AL-2. 2 Li-2. 7 Cu.", *Welding Journal* 68 (1989): 327s-337s.

- [22] Kou, S., Kanevsky, T., Fyfe, S., "Welding thin plates of aluminum alloys-a quantitative heat-flow analysis", *Welding Journal*, 61 (1982): 175s-181s.
- [23] Flemings, M. C., "Solidification processing", *Metallurgical transactions*, 5.10 (1974): 2121-2134.
- [24] Rajasekhar, K., Harendranath, C. S., Raman, R., Kulkarni, S. D., "Microstructural evolution during solidification of austenitic stainless steel weld metals: a color metallographic and electron microprobe analysis study" *Materials Characterization*, 38.2 (1997): 53-65.
- [25] Norman, A. F., Drazhner, V., Prangnell, P. B., "Effect of welding parameters on the solidification microstructure of autogenous TIG welds in an Al-Cu-Mg-Mn alloy", *Materials Science and Engineering: A*, 259.1 (1999): 53-64.
- [26] Arata, Y., Matsuda, F., Matsui, A., "Effect of welding condition on solidification structure in weld metal of aluminum alloy sheets", *Transactions of JWRI* 3.1 (1974): 89-97.
- [27] Villafuerte, J. C., Kerr, H. W., "Electromagnetic stirring and grain refinement in stainless-steel GTA welds", *Welding journal* 69.1 (1990): 1s-13s.
- [28] Sunadaresan, S., Janaki Ram, G. D., "Use of magnetic arc oscillation for grain refinement of gas tungsten arc welds in titanium alloys", *Science and Technology of Welding and Joining* 4.3 (1999): 151-160.
- [29] Aidun, D. K., Dean, J. P., "Effect of enhanced convection on the microstructure of Al-Cu-Li welds", *Welding Journal* 78 (1999): 349-s.
- [30] Ganaha, T., Pearce, B. P., Kerr, H. W., "Grain structures in aluminum alloy GTA welds", *Metallurgical Transactions A* 11.8 (1980): 1351-1359.
- [31] Bettinger, W. J., Coriell, S. R., Greer, A.L., Karma, A., Kurz, W., Rappaz, M., Trivedi, R., "Solidification microstructures: recent developments, future directions", *Acta Materialia* 48 (2000): 43-70.

- [32] Saito Y, Goldbeck-Wood G., Muller-Krumbhaar H, "Numerical simulation of dendritic growth.", *Physical Review A* 38.4 (1988): 2148.
- [33] Sullivan, J. M., Lynch, D. R., O'Neill, K., "Finite element simulation of planar instabilities during solidification of an undercooled melt", *Journal of Computational Physics* 69.1 (1987): 81-111.
- [34] Duggan, G., Tong. M., Browne. D. J., "An integrated meso-scale numerical model of melting and solidification in laser welding", *IOP Conference Series: Materials Science and Engineering* 27 (2012): 1-6.
- [35] Boettinger, W. J., Warren, J. A., Beckermann, C., Karma, A., "Phase-field simulation of solidification", *Annual Review of Materials Research* 32 (2002): 163-194.
- [36] Warren, J. A., Kobayshi, R., Lobkovsky, A. E., Carter, W. C., "Extending phase field models of solidification to polycrystalline materials", *Acta Materialia* 51 (2003): 6035-6058.
- [37] Karma, A., Rappel, W. J., "Phase-field method for computationally efficient modeling of solidification with arbitrary interface kinetics", *Physical Review E* 53.4 (1996): R3017.
- [38] Henry, S., PhD thesis, No. 1943, Ecole Polytechnique Fédérale de Lausanne, Lausanne, 1999.
- [39] Farzadi, A., Do-Quang, M., Serajzadeh, S., Kokabi, A. H., Amberg, G., "Phase-field simulation of weld solidification microstructure in an Al-Cu alloy", *Modelling and Simulation in Materials Science and Engineering*, 16 (2008): 1-18.
- [40] Fallah, V., Amooezaei, M., Provatas, N., Corbin, S. F., Khajepour, A., "Phase-field simulation of solidification morphology in laser powder deposition of Ti-Nb alloys", *Acta Materialia* 60 (2012): 1633-1646.
- [41] Zheng, W. J., Dong, Z. B., Wei, Y. H., Song, K. J., Guo, J. L., Wang, Y., "Phase field investigation of dendrite growth in the welding pool of aluminum alloy 2A14 under transient conditions", *Computational Materials Science*, 82 (2014): 525-530.

- [42] Montiel, D., Liu, L., Xiao, L., Zhou, Y., Provatas, N., "Microstructure analysis of AZ31 magnesium alloy welds using phase-field models", *Acta Materialia* 60 (2012): 5925-5932.
- [43] Rappaz, M., Bellet, M., Deville, M. O., "Numerical modeling in materials science and engineering", Springer Science & Business Media, Berlin, 2010.
- [44] Zhan, X. H., Dong, Z. B., Wei, Y. H., Ma, R., "Simulation of grain morphologies and competitive growth in weld pool of Ni-Cr alloy", *Journal of Crystal Growth* 311.23 (2009): 4778-4783.
- [45] Bordreuil, C., Niel, A., "Modelling of hot cracking in welding with a cellular automaton combined with an intergranular fluid flow model", *Computational Materials Science* 82 (2014): 442-450.
- [46] Vernède, S., Rappaz, M., "A simple and efficient model for mesoscale solidification simulation of globular grain structures", *Acta Materialia* 55.5 (2007): 1703-1710.
- [47] Vernède, S., Rappaz, M., "Transition of the mushy zone from continuous liquid films to a coherent solid", *Philosophical Magazine* 86.24 (2006): 3779-3794.
- [48] Phillion, A. B., Vernède, S., Rappaz, M., Cockcroft, S. L., Lee, P. D., "Prediction of solidification behaviour via microstructure models based on granular structures", *International Journal of Cast Metals Research* 22.1-4 (2009): 240-243.
- [49] Mathier, V., Jacot, A., Rappaz, M., "Coalescence of equiaxed grains during solidification", *Modelling and Simulation in Materials Science and Engineering* 12.3 (2004): 479-490.
- [50] Phillion, A. B., Cockcroft, S. L., Lee, P. D., "A three-phase simulation of the effect of microstructural features on semi-solid tensile deformation", *Acta Materialia* 56.16 (2008): 4328-4338.
- [51] Zaragoci, J. F., Silva, I., Bellet, M., Gandin, C. A., "Numerical tensile test on a mushy zone sample", *IOP Conference Series: Materials Science and Engineering* 33 (2012).

- [52] Lippold, J. C., "Recent developments in weldability testing" In : Hot cracking phenomena in welds, Springer, 2005, pp. 271-290.
- [53] Heuser, H., "Value of different hot cracking tests for the manufacture of the filler metals" In : Hot cracking phenomena in welds, Springer, 2005, pp. 305-327.
- [54] Farrar, J. C. M., "Hot cracking tests-the route to international standardization" In : Hot cracking phenomena in welds, Springer, 2005, pp. 291-305.
- [55] Borland, J. C., Rogerson, J. H., "Examination of the patch test for assessing hot cracking tendencies of weld metal", British Welding Journal 9 (1962): 464-498.
- [56] Nelson, T. W., Lippold, J. C., Lin, W., Baeslack, W. A., "Evaluation of the circular patch test for assessing weld solidification cracking, Part I- Development of a test method", Welding Journal 76.3 (1997): 110s-119s.
- [57] Holdcroft, P. T., "A simple cracking test for use with argon-arc welding", British Welding Journal 2 (1955): 471-475.
- [58] Savage, W. F., Lundin, C. D., "The vareststraint test." Welding Journal 44.10 (1965): 433s.
- [59] Wilken, K., Kleistner H., "The MVT test-A new universal procedure for testing the hot cracking sensitivity during welding", Material Und Technik, 1 (1982): 3-10.
- [60] Cross, C. E., Coniglio, N., "Weld solidification cracking: critical conditions for crack initiation and growth" In: Hot cracking phenomena in welds II, Springer, 2008, pp. 39-58.
- [61] Herold, H., Streitenberger, A., Pchennikov, A., "Modeling of the PVR test to examine the origin of different hot cracking types" In: Mathematical modeling of weld phenomena 5, IOM, 2001, pp. 783-792.
- [62] Tamura, H., Kato, N., Ochiai, S., Katagiri, Y., "Cracking study of aluminum alloys by the variable tensile strain hot cracking test", Transactions of the Japan Welding Society 8.2 (1977): 143-149.

- [63] Böllinghaus, T., Herold, H., " Hot cracking phenomena in welds", Springer Science & Business Media, Berlin, 2005.
- [64] Böllinghaus, T., Herold, H., Cross, C. E., Lippold, J. C. "Hot cracking phenomena in welds II", Springer Science & Business Media, Berlin, 2008.
- [65] Lippold, J. C., Böllinghaus, T., Cross, C.E., "Hot cracking phenomena in welds III", Springer Science & Business Media, New York, 2011.
- [66] Singer, A. R. E., Jennings, P. H., "Hot shortness of aluminum silicon alloys of commercial purity" *Journal of The Institute of Metals* 73 (1947): 197-212.
- [67] Pumphrey, W. I., Lyons, J. V., "Cracking during the casting and welding of the more common binary aluminum alloys", *Journal of The Institute of Metals* 74 (1948): 439.
- [68] Dowd, J. D., "Weld cracking of aluminum alloys", *Welding Journal* 31 (1952): 448s.
- [69] Jennings, P. H., Singer, A. R. E., Pumphrey, W. L., "Hot-shortness of some high purity alloys in the system aluminum copper silicon and aluminum magnesium silicon", *Journal of the Institute of Metals* 74.7 (1948): 227-246..
- [70] Dudas, J. H., Collins, F. R., "Preventing weld cracks in high-strength aluminum alloys.", *Welding journal* 45.6 (1966): 241s.
- [71] Michaud, E. J., Kerr, H. W., Weckman, D. C., " Temporal pulse shaping and solidification cracking in laser welded Al-Cu alloys " In: *Trends in Welding Research*, ASM International, Ohio, 1995, p. 154.
- [72] Coniglio, N., Cross, C. E., Michael, Th., Lammers, M., "Defining a critical weld dilution to avoid solidification cracking in aluminum", *Welding Journal* 87.8 (2008): 237s-247s.
- [73] Mousavi, M. G., Cross, C. E., Grong, O., "Effect of Scandium and Titanium-Boron on Grain refinement and hot cracking of aluminum alloy 7108", *Science and Technology of Welding and Joining* 4.6 (1999): 381-388.
- [74] Warrington, D., McCartney, D. G., "Development of a new hot cracking test for aluminum alloys", *Cast Metals* 2.3 (1989): 134-143.

- [75] Eskin, D. G., Suyitno, W. H., Katgerman, L., "Mechanical properties in the semisolid state and hot tearing of aluminum alloys", *Progress in Materials Science* 49 (2004):629-711.
- [76] Arata, Y. Matsuda, F., Nakata, K., Shinozaki, K., "Solidification crack susceptibility of aluminum alloy weld metals (report II)-effect of straining rate on cracking threshold in weld metal during solidification" *Transactions of JWRI* 6.1 (1977): 91-104.
- [77] Matsuda, F., Nakagawa, H., Nakata, K., Okada, H., "The VDR cracking test for solidification crack susceptibility on weld metals and its application to aluminum alloys" *Transactions of JWRI* 8 (1979): 85-95.
- [78] Yang, Y. P., Dong, P., Zhang, J., and Tian, X., "A hot-cracking mitigation technique for welding high-strength aluminum alloy." *Welding Journal* 79.1 (2000): 9s.
- [79] Chihoski, R. A., "The character of stress field around a weld arc moving on aluminum sheet" *Welding Journal* 51.1 (1972): 9s-18s.
- [80] Chihoski, R.A., "Expansion and stress around aluminum weld puddles", *Welding Journal*, 58.9 (1979): 263s-276s.
- [81] Cicala, E., Duffet, G., Andrzejewski, H., Grevey, D., Ignat S., "Hot cracking in Al-Mg-Si alloy laser welding: Operating parameters and their effects", *Materials Science and engineering* 395A (2005):1-9.
- [82] Hunziker, O., Dye, D., Roberts, S. M., Reed, R.C., "A coupled approach for the prediction of solidification cracking during the welding of superalloys" In: *Hot cracking phenomena in welds*, Springer, 2005, pp. 299-319.
- [83] Shibahara, M., Serizawa, H., Murakawa, M., "Finite element method for hot cracking analysis using temperature dependent interface element" In: *Hot cracking phenomena in welds*, Springer, 2005, pp. 253-267.
- [84] Niel, A., Deschaux-Beaume, F., Bordreuil, C., Fras, G., Drezet, J. M., "Hot tearing test for TIG welding of aluminum alloys: Application of a stress parallel to the fusion line" In: *Hot cracking phenomena in welds III*, Springer, 2011, pp. 43-59.

- [85] Zacharia, T., "Dynamic stresses in weld metal hot cracking", *Welding Journal* 73.7 (1994): 164s-172s.
- [86] Langlais, J., Gruzleski, J. E., "A novel approach to assessing the hot tearing susceptibility of aluminum alloys", *Materials Science Forum* 331-337 (2000): 167-172.
- [87] Dickhaus, C. H., Ohm, L., Engler, S., "Mechanical properties of solidifying shells of aluminum alloys", *American Foundrymen Society Transactions* 101 (1994): 677-684.
- [88] Lahaie, D. J., Bouchard, M., "Physical modeling of the deformation mechanisms of semisolid bodies and a mechanical criterion for hot tearing", *Metallurgical and Materials Transactions* 32B.8 (2001): 697-705.
- [89] Pellini, W. S., "Strain theory of hot tearing", *Foundry* 80.11 (1952): 125-133.
- [90] Magnin, B., Maenner, L., Katgerman, L., Engler, S., "Ductility and rheology of an Al-4.5% Cu alloy from room temperature to coherency temperature", *Materials Science Forum* 217 (1996): 1209-1214.
- [91] Matsuda, F., Nakata, K., Harada, S., "Moving characteristics of weld edges during solidification in relation to solidification cracking in GTA weld of aluminum alloy thin sheet", *Transactions of JWRI* 9.2 (1980): 83-93.
- [92] Matsuda, F., Nakata, K., Tsukamoto, K., Kohzoh, A., "Effect of additional alloying element on weld solidification crack susceptibility of Al-Zn-Mg alloy", *Transactions of JWRI* 12.2 (1985): 93-102.
- [93] Ploshikhin, V., Prihodovsky, A., Makhutin, M., Llin, A., Zoch, H. W., "Integrated mechanical-metallurgical approach to modeling of solidification cracking in welds" In: *Hot cracking phenomena in welds*, Springer, 2005, pp. 223-244.
- [94] Prokhorov, N. N., "Resistance to hot tearing of cast metals during solidification" *Russian Castings Production* 4 (1962): 172-175.
- [95] Feurer, U. "Quality control of engineering alloys and the role of metals science", Delft University of Technology, Delft, The Netherlands (1977): 131-45.

- [96] Vero, J., "The hot shortness of aluminum alloys", *The Metal Industry* 48 (1936): 431-494.
- [97] Feurer, U., "Influence of alloy composition and solidification conditions on dendrite arm spacing, feeding, and hot tear properties of aluminum alloys" In: *Proceedings of International Symposium of Engineering Alloys, Delft, 1977*, pp. 131-145.
- [98] Clyne, T. W., Davies, G. J., "Comparison between experimental data and theoretical predictions relating to dependencies of solidification cracking on composition" In: *TMS Proceedings of International Conference of Solidification, Sheffield, 1979*, pp. 275-278.
- [99] Rappaz, M., Drezet, J. M., Gremaud, M., "A new hot-tearing criterion", *Metallurgical and materials transactions A* 30A (1999): 449-455.
- [100] Kou, S., "A criterion for cracking during solidification", *Acta Materialia* 88 (2015): 366-374.
- [101] Drezet J. M., Allehaux, D., "Application of Rappaz-Drezet-Gremaud hot tearing criterion to welding of aluminum alloys" In: *Hot cracking phenomena in welds II*, Springer, 2008, pp. 19-39.
- [102] Campbell, J., "Solidification modelling: current limitations and future potential", *Materials science and technology* 7.10 (1991): 885-894.
- [103] Jones, S. F., Evans, G. M., Galvin, K. P., "Bubble nucleation from gas cavities- a review", *Advances in Colloid and Interfaces Science* 80 (1999): 27-50.
- [104] Fisher, J. C., "The fracture of liquids", *Journal of Applied Physics* 19 (1948): 1062-1067.
- [105] Tiwari, S. N., Beech, J., "Origin of gas bubbles in aluminum", *Metal Science* 12.8 (1978): 356-362.
- [106] Rooy, E. L., "Mechanisms of porosity formation in aluminum", *Modern Casting* 82.9 (1992): 34-36.

- [107] Campbell, J., "Pore nucleation in solidifying metals", The Solidification of Metals Iron and Steel Institute (1968): 18-26.
- [108] Lee, P. D., Atwood, R. C., Dashwood, R. J., Nagaumi, H., " Modeling of porosity formation in direct chill cast aluminum-magnesium alloys", Materials Science and Engineering A328 (2002): 213-222.
- [109] Talbot, D. E. J., "The effects of hydrogen in aluminum and its alloys", Maney publishing, 2004.
- [110] Dixon, B., "Weld metal solidification cracking in steels" In: Proceedings of IIW Asian Pacific Regional Welding Congress, Hobart, Tasmania, 1988: 731-751.
- [111] Syvertsen, M., "Oxide skin strength on molten aluminum", Metallurgical and Materials Transactions B 37.3 (2006): 495-504.
- [112] Wenda, T., Yung, C. S., "Multi-scale modelling of solidification and microstructure development in laser keyhole welding process for austenitic stainless steel" Computational Materials Science 98 (2015): 446-458.
- [113] Koseki, T., Inoue, H., Fukuda, Y., Nogami, A., "Numerical simulation of equiaxed grain formation in weld solidification", Science and Technology of Advanced Materials 4 (2003): 183-195.
- [114] Sistaninia, M., Terzi, S., Phillion, A. B., Drezet, J. M., Rappaz, M., "3-D granular modelling and in situ X-ray tomography imaging: A comparative study of hot tearing formation and semisolid deformation in Al-Cu alloys", Acta Materialia 61 (2013): 3831-3841.
- [115] Cross, C. E., Coniglio, N., Schempp, P., Mousavi, M., "Critical conditions for weld solidification crack growth" In: Hot cracking phenomena in welds III, Springer, Berlin, 2011, pp. 25-41.
- [116] Zareie Rajani, H. R., Phillion, A. B., "A mesoscale solidification simulation of fusion welding in aluminum-magnesium-silicon alloys" Acta Materialia 77 (2014): 162-172.

- [117] Bonifaz, E. A., Richards, N. L., "Modeling cast IN-738 superalloy gas tungsten arc welds", *Acta Materialia* 57.6 (2009): 1785-1794.
- [118] <http://math.lbl.gov/voro++/doc/>
- [119] Brenner, S. C., Scott, L. R., "The mathematical theory of finite element methods", Springer-Verlag, New York, 1994.
- [120] Yan, X., Chen, S., Xie, F., Chang, Y. A., "Computational and experimental investigation of microsegregation in an Al-rich Al–Cu–Mg–Si quaternary alloy", *Acta Materialia* 50.9 (2002): 2199-2207.
- [121] Wang, H., Liu, F., Yang, G., Zhou, Y., "Modeling the overall solidification kinetics for undercooled single-phase solid-solution alloys. II. Model application", *Acta Materialia* 58.16 (2010): 5411-5419.
- [122] Clyne, T. W., Kurz, W., "Solute redistribution during solidification with rapid solid state diffusion", *Metallurgical Transactions A* 12.6 (1981): 965-971.
- [123] Coniglio, N., Cross, C. E., "Initiation and growth mechanisms for weld solidification cracking", *International Materials Reviews* 58 (2013): 375-397.
- [124] Prasad, Y. V. R. K., Sasidhara, S., Gegel, H. L., Malas, J. C., "Hot working guide: A compendium of processing maps", ASM International, Ohio, 1997.
- [125] Mahabunphachai, S., Koç, M., "Investigations on forming of Aluminum 5052 and 6061 sheet alloys at warm temperatures", *Materials & Design* 31 (2010): 2422-2434.
- [126] Lindgren, L. E., "Computational welding mechanics: thermomechanical and microstructural simulations", CRC Press, New York, 2007.
- [127] Manes, A., Peroni, L., Scapin, M., Giglio, M., "Analysis of strain rate behaviour of an Al 6061-T6 alloy", *Procedia Engineering* 10 (2011): 3477-3482.
- [128] Wang, J. J., Phillion, A. B., GuiMin Lu, "Development of a visco-plastic constitutive modeling for thixoforming of AA 6061 in semi-solid state", *Journal of Alloy and Compounds* 609 (2014): 290-295.

- [129] Farup, I., Drezet, J. M., Rappaz, M., "In situ observation of hot tearing formation in Succinonitrile-Acetone", *Acta Materialia* 49 (2001): 1261-1269.
- [130] Dijkstra, W. O., Vuik, C., Katgerman, L., "Network model of fluid flow in semi-solid aluminum alloys", *Computational Materials Science* 38.1 (2006): 67-74.
- [131] Dongarra, J., Lumsdaine, R., Pozo, R., Remington, K., "A sparse matrix library in C++ for high performance architectures" In: proceedings of the second object oriented numerics conference, 1994, 214-218.
- [132] Poirier, D. R., Yeum, K., Maples, Al. I., "A thermodynamic prediction for microporosity formation in aluminum-rich Al-Cu alloys", *Metallurgical Transactions A* 18.11 (1987): 1979-1987.
- [133] Lee, Y. W., Chang, E., Chieu, C. F., "Modeling of feeding behavior of solidifying Al-7Si-0.3 Mg alloy plate casting", *Metallurgical Transactions B* 21.4 (1990): 715-722.
- [134] Kubo, K., Pehlke, R. D., "Mathematical modeling of porosity formation in solidification" *Metallurgical Transactions B* 16.2 (1985): 359-366.
- [135] Sigworth, G. K., Wang, C., "Evolution of porosity in long freezing range alloys", *Metallurgical Transactions B* 24.2 (1993): 365-377.
- [136] Sabau, A. S., Viswanathan, S., "Microporosity prediction in aluminum alloy castings", *Metallurgical and Materials Transactions B* 33.2 (2002): 243-255.
- [137] Kuznetsov, A. V., Vafai, K., "Development and investigation of three-phase model of the mushy zone for analysis of porosity formation in solidifying castings", *International journal of heat and mass transfer* 38.14 (1995): 2557-2567.
- [138] Dean, R. B., "The formation of bubbles", *Journal of Applied Physics* 15 (1994): 446-451.
- [139] Nield, D. A., Bejan, A., "Mechanics of fluid flow through a porous medium", Springer, New York, 2013.

[140] Devletian, J. H., Wood, W. E., "Factors affecting porosity in aluminum welds- a review", Welding Research Council Bulletin, 290 (1993): 1-18.